



Fakultät für Maschinenwesen
Lehrstuhl für Aerodynamik und Strömungsmechanik

Experimental Investigation of Shock-Induced Droplet Breakup

Zhaoguang Wang

Vollständiger Abdruck der von der Fakultät für Maschinenwesen der Technischen Universität München zur Erlangung des akademischen Grades eines

Doktor-Ingenieurs (Dr.-Ing.)

genehmigten Dissertation.

Vorsitzender: Prof. Rafael Macián-Juan, Ph.D.

Prüfer der Dissertation:

1. Prof. Dr.-Ing. Nikolaus A. Adams
2. Prof. David Hung, Ph.D.

Die Dissertation wurde am 11.02.2021 bei der Technischen Universität München eingereicht und durch die Fakultät für Maschinenwesen am 19.05.2021 angenommen.

Declaration of Authorship

I hereby declare that except where specific reference is made to the work of others, the contents of this dissertation are original and have not been submitted in whole or in part for consideration for any other degree or qualification in this, or any other university. This dissertation is my own work and contains nothing which is the outcome of work done in collaboration with others, except as specified in the text and Acknowledgements.

Zhaoguang Wang
February 1, 2021

© Zhaoguang Wang, 2021
zg.wang@tum.de

All rights reserved. No part of this publication may be reproduced, modified, re-written, or distributed in any form or by any means, without the prior written permission of the author.

Released February 1, 2021
Typesetting \LaTeX

Abstract

This cumulative thesis focuses on experimental investigation of droplet aerobreakup. A shock tube is employed for the generation of well-defined flow conditions. The temporal steadiness and the spatial uniformity of the shock-induced freestream flow is verified by systematic pressure measurements. Optimization guidelines for the design of pressure sensor housings are proposed in the first publication to improve the measurement accuracy and the response rate. The shock tube provides a wide range of operating conditions and renders possible the experiments of droplet breakup in highly-rarified supersonic flow. Owing to this advantage, the impact of flow Mach number on stripping breakup is elucidated in the second publication to address the importance of flow compressibility in supersonic atomization. The shock tube also allows for the study of simultaneous breakup of closely spaced droplet clusters, as the ambient flow is instantly established by the fast-propagating incident shock wave. Thus, the breakup behavior of droplets in tandem formation at different separation distances is illustrated in the third publication to evaluate the droplet interaction in dense sprays.

In impulse facilities such as shock tubes and expansion tubes where the experimental time window is limited, measurement of transient stagnation pressure is critical. The first part of this thesis analyzes the characteristic behavior of pressure sensors shielded by housings of different geometries. Compared to the conical housings that are commonly adopted in conventional steady/quasi-steady pressure measurements, the blunt housings show consistent advantages under transient conditions and produce pressure signals with shorter rise time and less pronounced oscillations. Additionally, the blunt housings give rise to lower errors when practical problems such as misaligned assembly and exposure of the sensor surface are present. This work delivers the key message that it is mandatory to employ sensor housings with blunt tips and short internal void to achieve robust high-accuracy fast-response measurements of transient stagnation pressure.

With the rapid development of supersonic gas atomizers, droplet breakup in high-speed flows becomes of increasing importance. In contrast to most research that places emphasis on Weber and Ohnesorge numbers, the second part of this thesis investigates the effect of flow Mach number on the breakup behavior in the shear stripping regime. The main feature is that the Mach number is decoupled from other non-dimensional parameters and varied independently. As opposed to the conventional stripping pattern in subsonic flow with fine mist shed off the liquid sheet around the equator, the breakup process in transonic flow is characterized by rupture of multiple bags formed along the periphery and in supersonic flow by fragmentation of ligament structures stretching from the leeward surface. Moreover, increasing the flow Mach number disrupts the uniformity of fragment sizes and narrows the cross-stream span of fragment dispersion. This work highlights the necessity of developing new models to

accurately predict the performance of supersonic atomization.

In practical applications related to dense sprays, the interaction between droplets in close proximity tends to affect the breakup behavior. The third part of this thesis studies the droplet breakup in tandem formation and particularly details the interactive modes over a wide range of Weber numbers and separation distances. The key finding is that whereas the breakup pattern of the lead droplet is barely altered, the breakup intensity of the trailing droplet is consistently weakened as the separation distance decreases to critical levels. The size of bag structures is reduced in low-Weber number regimes and the cross-stream dispersion of fragments is narrowed in high-Weber number regimes. Furthermore, conventional breakup morphologies are not preserved at even smaller separation distances and new patterns including puncture and coalescence modes emerge. This work provides quantitative bases for the modeling of droplet interaction in dense sprays.

Acknowledgements

Before I embarked on my four-year pursuit of the PhD degree, I had been warned of the challenges and difficulties in the journey. But to get dressed up in the doctoral cap and gown, I guess everyone just has to live through his/her own bitterness and sweetness. Fortunately, in the last four years I have met so many wonderful colleagues in work and made so many warm-hearted friends in life, to whom I would like to express my sincerest gratitude.

First of all, I would like to thank Prof. Nikolaus A. Adams for his inspiring supervision and patient mentoring. I feel genuinely grateful for his help with my research work and his support when I was striving for my future academic career. Particularly, his attitude of being responsible for every student is what I would bear in mind as a code of conduct. My special thanks goes to Dr. Marcus Giglmaier and Thomas Hopfes. I truly appreciate all the effort Marcus has paid in supervising my work and sustaining my contract. His words of encouragement gave me the confidence to face my anxiety and unease. Thomas and I collaborated on almost every aspect of the work. The word "collaboration" simply cannot describe the time we spent together in conducting experiments and discussing topics. I am truly grateful for having such a wonderful colleague and for the memorable experiences we shared in these years. My thanks is extended to Dr. Steffen Schmidt for the constructive suggestions on my research work as well as for all the beer talks in the Italian restaurant. I also would like to wish Jingyu Wang all the best and hope he keeps in mind there is always light at the end of the tunnel.

I want to thank Mrs. Angela Grygier for her kind assistance with my working contract, Mr. Wolfgang Lützenburg, Mr. Martin Banzer and Mr. Luigi Findanno for their great help with our experimental setup, and Ms. Hua Liu for her patient delivery of our experimental consumables. I also feel honored to have worked with colleagues Nico Fleischmann, Jakob Kaiser, Josef Winter, Theresa Trummler and many others. They have offered me valuable help and widened my research visions.

I feel extremely fortunate to have made so many close friends in Munich. Xi Chen, Jiang Zhang, Sanmei Wang, Shuangjie Shu, Guoli Ma and Qingping Wu left their footprints with me over places from Heidelberg to Dresden and from Czech Republic to Turkey. Our friendship makes me realize what "I'll be there for you" truly is. I shared great time with Zibo Zhou, Yin Ruan and Shu Lu as flatmates and enjoyed all the chances they provided to try "a bite of China" abroad. I also spent a great number of Saturday afternoons with friends Zhen Xu, Yuhang Yun and many others playing table tennis, which helped me effectively relieve stress and restore energy. Particularly, I would like to thank two of my undergraduate friends Nan Li and Yang Yang, who traveled to Munich specially for our reunion.

Last but not least, I would like to express my deepest gratitude to my family. My

VIII

parents, grandparents, elder brother and sister have always loved and supported me unconditionally. My two lovely nephews have brought priceless happiness to my daily routine. I cannot say enough how grateful I feel to have been born in such a family and how much I love them. This thesis is dedicated to them, the most important people in my life.

Contents

Declaration of Authorship	III
Abstract	V
Acknowledgements	VII
1 Introduction	1
1.1 State of the Art	1
1.1.1 Generation of well-defined flow conditions in shock tubes	1
1.1.2 Pressure measurement techniques in shock tubes	3
1.1.3 Droplet breakup/secondary atomization	4
1.2 Motivation and Objective	9
1.3 Outline	11
2 Experimental Methods	13
2.1 Shock Tube	13
2.2 Pressure Measurement System	15
2.3 Schlieren/Shadowgraph Photography	17
2.4 Droplet Generation	18
2.5 Experimental Matrix	19
2.5.1 Sensor housing design for total pressure measurement	19
2.5.2 Droplet breakup in supersonic flow	20
2.5.3 Droplet breakup in tandem formation	21
3 Summary of Publications	23
3.1 Impact of Sensor Housing Geometries on Transient Stagnation Pressure Measurements in Impulse Facilities	23
3.1.1 Summary of the publication	23
3.1.2 Individual contributions of the candidate	24
3.2 Effect of Mach Number on Droplet Aerobreakup in Shear Stripping Regime	25
3.2.1 Summary of the publication	25
3.2.2 Individual contributions of the candidate	26
3.3 Experimental Investigation of Shock-Induced Tandem Droplet Breakup . .	27
3.3.1 Summary of the publication	27
3.3.2 Individual contributions of the candidate	28
4 List of Publications	29
4.1 Peer-Reviewed Journal Articles	29

X

5 Discussion	31
6 Outlook	33
Bibliography	35
A Original Peer-Reviewed Publications	43
A.1 Impact of Sensor Housing Geometries on Transient Stagnation Pressure Measurements in Impulse Facilities	45
A.2 Effect of Mach Number on Droplet Aerobreakup in Shear Stripping Regime	61
A.3 Experimental Investigation of Shock-Induced Tandem Droplet Breakup . .	83
B Copyright Permissions for Reproduced Material	99

Nomenclature

Greek letters:

ϵ	Density ratio between liquid and gas
η	Viscosity ratio between liquid and gas
γ	Ratio of specific heats
μ	Dynamic viscosity
ρ	Density

Non-dimensional groups:

M	Mach number
Oh	Ohnesorge number
Re	Reynolds number
We	Weber number

Roman letters:

a	Speed of sound
C_D	Drag coefficient
D	Normalized diameter of the housing borehole
d	Droplet diameter
G	Normalized depth of the housing cavity
H	Normalized diameter of the sensor tip
h	Sensor tip diameter
i	Relative magnitude of Mach number
j	Relative magnitude of Reynolds number
L	Normalized length of the housing borehole
P	Normalized pressure

XII

p	Pressure
PR	Pressure ratio p_4/p_1
S	Normalized separation distance between tandem droplets
s	Separation distance between tandem droplets
T	Normalized time
t	Time
u	Velocity
w	Vertical misalignment between tandem droplets
x	Streamwise location or displacement

Super- and subscripts:

—	Condition of the post-bow shock flow
0	Initial condition, e.g. $t = 0$
1	Condition of the stationary driven gas in the shock tube
3	Condition of the expanding driver gas in the shock tube
4	Condition of the stationary driver gas in the shock tube
∞	Condition of the shock-induced freestream flow in the shock tube
avg	Value averaged from repeated experiments
D	Value based on the housing borehole diameter
d	Condition of the liquid droplet
d_0	Value based on the initial droplet diameter
s	Condition of the incident shock wave

1 Introduction

The present doctoral project focuses on employing a shock tube facility to experimentally investigate fragmentation of dispersed media. The shock waves impose step changes to the pressure and velocity of the continuous phase that further exerts inertial forces on the dispersed phase, and cause distortion and rupture of the immiscible interface. The analyses require fine temporal and spatial resolutions, and involve complex physics such as interfacial instabilities and nonlinear dynamics.

The shock tube adopted in the study is capable of generating a wide range of well-defined flow conditions. A significant amount of effort was first dedicated to validating the performance, including shock attenuation along the propagation, temporal steadiness and spatial uniformity of the shock-induced freestream flow. To accurately describe the flow conditions with low uncertainties, systematic pressure measurements were carried out and optimization of the instrumental technique was proposed. The shock tube was then employed to study two types of fragmentation phenomena, namely breakup of liquid droplets and collapse of gas bubbles. Droplet breakup is an essential process in atomization and exhibits distinct morphologies at different ambient flow conditions. Breakup patterns of droplets in supersonic flow and in tandem formation were thoroughly investigated to shed light on underlying physics in supersonic atomization and dense sprays, respectively. Bubble collapse occurs mostly in cavitation-related scenarios and shows aspherical features with the presence of nearby boundaries. Collapse strengths of bubbles close to deformable boundaries and in non-Newtonian fluids were studied to assess the potential destruction of *in vivo* cavitation.

This cumulative thesis details the development of the experimental methodology and overviews my work in the field of shock-induced droplet breakup. Three topics are presented in this thesis: optimization of sensor housing geometries for total pressure measurement, impact of flow Mach number on stripping breakup of single droplets, and variation of tandem droplet breakup at different separation distances. The work related to bubble collapse is not presented in this thesis.

1.1 State of the Art

1.1.1 Generation of well-defined flow conditions in shock tubes

The shock tube is an impulse facility to generate shock waves that lead a region of uniform flow [1, 2]. It has been widely adopted in studies of experimental fluid mechanics, such as wave interactions [3], boundary layer growth [4] and flame propagation [5].

The shock tube consists of a high-pressure driver section and a low-pressure driven section. A diaphragm separates these two parts and a planar shock wave is generated

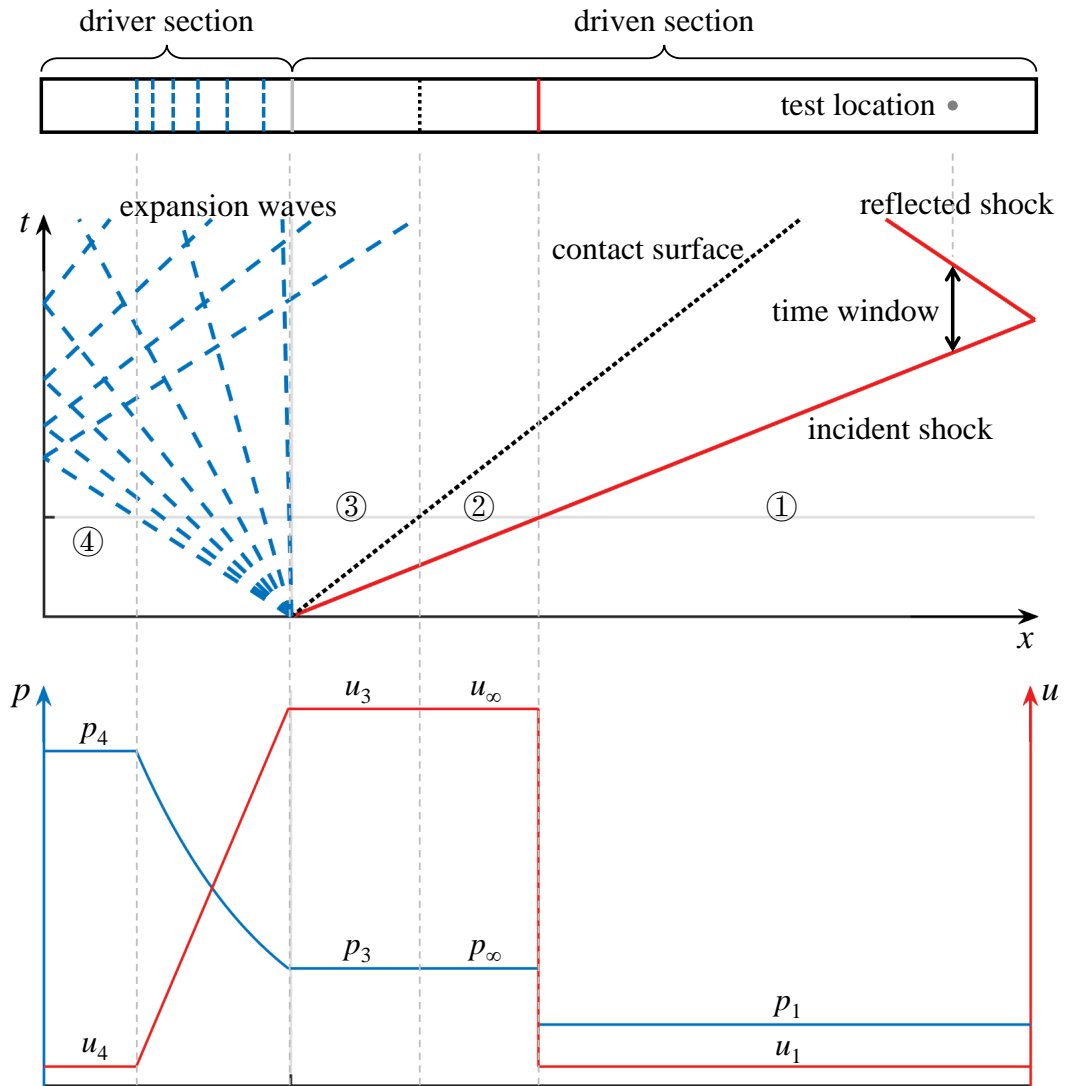


Figure 1.1: Ideal wave dynamics and associated pressure and velocity distributions inside the shock tube. The uniform flow conditions in region ② are conventionally exploited for fluid mechanics experiments.

when the diaphragm ruptures at predetermined conditions. Figure 1.1 illustrates the ideal evolution of wave dynamics inside the shock tube and also presents the corresponding pressure and velocity distributions. In the figure, $x = 0$ indicates the location of the diaphragm and $t = 0$ represents the time instant of diaphragm rupture. The incident shock wave (red solid line) propagates towards the downstream stationary low-pressure region (①) while expansion waves (blue dashed lines) travel along the opposite direction into the stationary high-pressure region (④). A contact surface (black dotted line) follows the movement of the incident shock and separates the expanding driver gas (③) and the compressed driven gas (②). The post-shock freestream flow in region ② exhibits uniform pressure and velocity, and is conventionally exploited for fluid mechanics experiments. The incident shock reflects at the endwall of the tube and the steady-flow time window is terminated when the reflected shock arrives at the test location. It is worth mentioning that the region ③ shares the same pressure and velocity as the region ② but has considerably distinct temperature (normally much lower

due to the expansion). The flow uniformity in the region ③ is disturbed to certain extent by the mixing across the contact surface.

Ideally, the freestream conditions are predefined by the initial states of driver and driven gases. The relation between the driver pressure p_4 , the driven pressure p_1 and the freestream pressure p_∞ is [6]

$$\frac{p_4}{p_1} = \frac{p_\infty}{p_1} \left(1 - \frac{(\gamma_4 - 1)(a_1/a_4)(p_\infty/p_1 - 1)}{\sqrt{2\gamma_1(2\gamma_1 + (\gamma_1 + 1)(p_\infty/p_1 - 1))}} \right)^{-2\gamma_4/(\gamma_4 - 1)}, \quad (1.1)$$

where γ and a are the ratio of specific heats and the speed of sound for each gas, respectively. Then the theoretical incident shock Mach number M_s is calculated as

$$M_s = \sqrt{\frac{\gamma_1 + 1}{2\gamma_1} \left(\frac{p_\infty}{p_1} - 1 \right) + 1} \quad (1.2)$$

and the freestream velocity u_∞ as

$$u_\infty = a_1 \frac{2M_s^2 - 2}{(\gamma + 1)M_s}. \quad (1.3)$$

Other freestream properties can be further derived from moving shock relations.

In reality, the incident shock strength highly depends on the diaphragm rupture. Imperfect rupture causes extra pressure loss and disrupts the sharpness of the shock front. There are several commonly-used methods to break the diaphragm. A mechanically driven plunger is employed in studies [7–9] to perforate the diaphragm. Other researchers [10–12] build shock tubes with scored diaphragms that burst with the buildup of the driver pressure. For low-pressure experiments where diaphragms are made of plastics, electric heating wires are adopted to melt the diagonals of the diaphragm [13–15].

1.1.2 Pressure measurement techniques in shock tubes

To assess the performance of the shock tube as well as to resolve the flow conditions with low uncertainties, fast-response high-accuracy measurement of the flow pressure is desired. The most widely employed technique for total pressure measurement is Pitot tubes due to the low cost and the simplicity of operation. They are conventionally adopted in steady/quasi-steady flows and the measured pressure is used to derive flow velocity or volumetric flow rate [16, 17]. Comprehensive reviews of Pitot tube techniques are provided by Folsom [18] and Chue [19], including various tube designs and calibration methods studied in wind tunnels.

In impulse facilities such as shock tubes and expansion tubes, however, the experimental time window is extremely short and the low response rate of conventional Pitot tubes fails to resolve the transient pressure variation properly. Therefore, piezoelectric or piezoresistive pressure sensors with short response time, high resonant frequency and high sensitivity are preferred [20–22]. The working principle is the same as conventional Pitot tubes, which is to create a stagnation region at the sensor tip by positioning them directly against the freestream flow. To avoid being damaged by fast-traveling fragments of the ruptured diaphragms, these expensive sensors are typically shielded by external housings [23–26]. Figure 1.2 shows the commonly-used conical housing

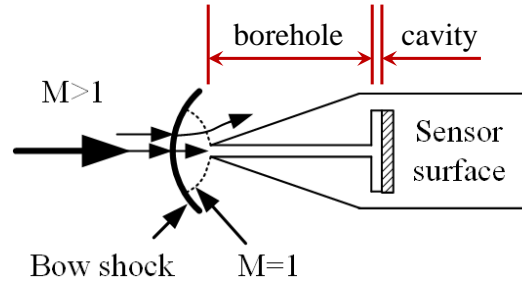


Figure 1.2: Conical housing geometry and the surrounding flow structures in supersonic flow.

geometry and highlights the presence of the characteristic narrow borehole and shallow cavity that connect the sensor surface to the ambient flow.

In subsonic flows, the shielded pressure sensor directly measures the freestream total pressure $p_{0\infty}$ which is related the static pressure p_∞ and the Mach number M_∞ in the following relation:

$$p_{0\infty} = p_\infty \cdot \left(1 + \frac{\gamma-1}{2} M_\infty^2\right)^{\frac{\gamma}{\gamma-1}}. \quad (1.4)$$

In supersonic flows, however, the measured pressure is interpreted differently. In front of the housing structure, a bow shock emerges as the supersonic flow decelerates to stagnation conditions [27]. By assuming normal shock relations across the center of the bow shock, the static pressure of the flow ahead of the housing \bar{p} is evaluated as

$$\bar{p} = p_\infty \cdot \left(1 + \frac{2\gamma}{\gamma+1} (M_\infty^2 - 1)\right) \quad (1.5)$$

and the flow Mach number \bar{M} as

$$\bar{M} = \sqrt{\left(1 + \frac{\gamma-1}{2} M_\infty^2\right) \left(\gamma M_\infty^2 - \frac{\gamma-1}{2}\right)^{-1}}. \quad (1.6)$$

The measured pressure by the shielded sensor is the total pressure behind the bow shock \bar{p}_0 , which can be theoretically calculated by replacing p_∞ and M_∞ in Equation 1.4 with \bar{p} and \bar{M} . Thus, \bar{p}_0 is related to the total pressure of the undisturbed freestream flow $p_{0\infty}$ in the following way

$$\bar{p}_0 = p_{0\infty} \cdot \left(\frac{\gamma+1}{2\gamma M_\infty^2 - (\gamma-1)}\right)^{\frac{1}{\gamma-1}} \left(\frac{\gamma+1}{2/M_\infty^2 + (\gamma-1)}\right)^{\frac{\gamma}{\gamma-1}}. \quad (1.7)$$

1.1.3 Droplet breakup/secondary atomization

In this thesis, the shock tube facility is mainly utilized to study the atomization phenomenon. Gas atomization is relevant in a diverse variety of applications, such as fuel

injection [28–32], spray coating [33–36] and powder metallurgy [37–40]. The atomization process is conventionally divided into two stages, primary atomization that refers to the initial disintegration of the liquid bulk into large droplets and secondary atomization that represents the further fragmentation of these droplets into micro fragments. Secondary atomization is of particular importance because it determines the final fragment size distribution which is the most crucial parameter in practical applications [41–44]. For instance, droplets of small sizes are desired in combustion systems to enhance evaporation and mixing rates.

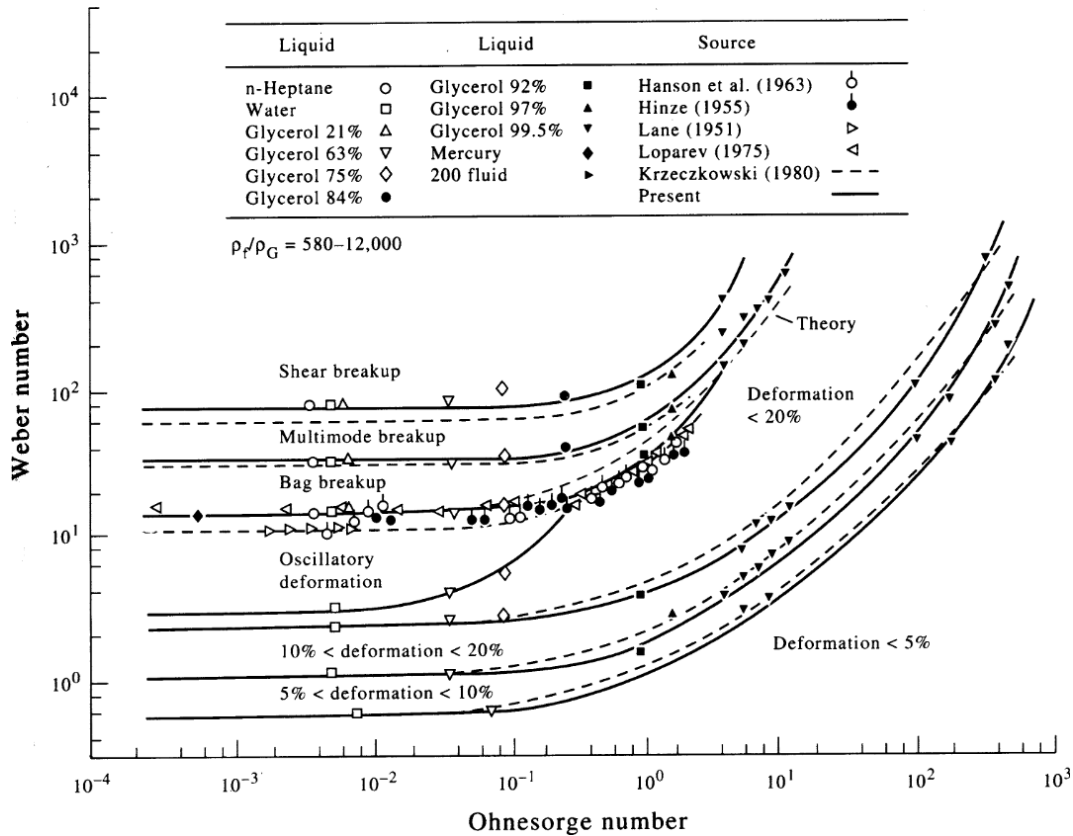


Figure 1.3: Variation of the breakup modes with Weber and Ohnesorge numbers. Reproduced from Ref. [45].

In secondary atomization, the aerodynamic force exerted by the ambient flow drives the deformation of the droplet, while the surface tension tends to restore a spherical shape. The droplet deformation is also resisted by internal viscous forces. Consequently, the two non-dimensional parameters widely adopted [46–50] to describe droplet breakup are the Weber number (We)

$$We = \rho_\infty u_\infty^2 d_0 / \sigma \quad (1.8)$$

and the Ohnesorge number (Oh)

$$Oh = \mu_d / \sqrt{\rho_d d_0 \sigma} \quad (1.9)$$

where ρ_∞ and u_∞ are the density and velocity of the gas freestream flow, and d_0 , σ , μ_d and ρ_d are the initial diameter, surface tension, dynamic viscosity and density of the

liquid droplet, respectively. The Weber number compares the disruptive aerodynamic force to the restorative surface tension, and the Ohnesorge number represents the ratio between the viscous force and the surface tension.

A number of droplet breakup modes have been reported in previous literature. Figure 1.3, which is reproduced from Ref. [45], provides an overview of the variation of the breakup modes at different Weber and Ohnesorge numbers. As indicated in the figure, the influence of the liquid viscosity diminishes for $Oh < 0.1$ leaving We as the solely dominant factor. For the sake of brevity, the following discussion only focuses on cases with $Oh < 0.1$. The simplified pattern of each breakup mode is sketched in Figure 1.4 that is reproduced from Ref. [50].

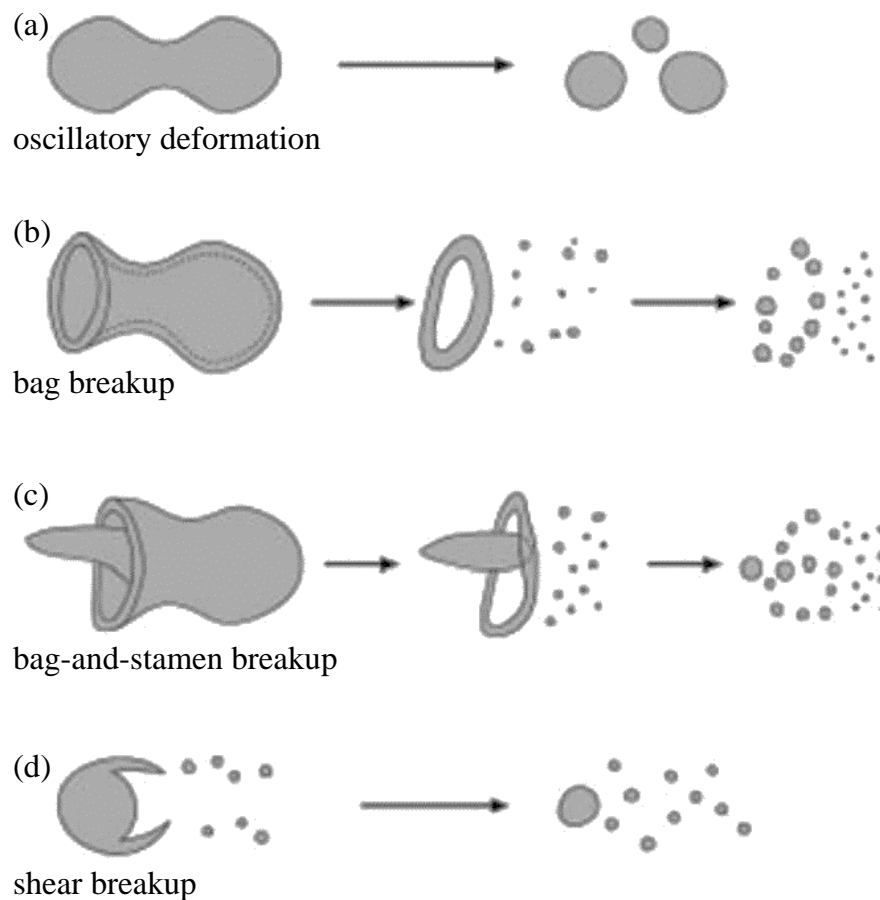


Figure 1.4: Sketch of droplet breakup modes, including oscillatory deformation (a), bag breakup (b), bag-and-stamen breakup (c) and shear breakup (d). Reproduced from Ref. [50].

For Weber numbers below 11, the droplet exhibits oscillatory deformation and occasionally breaks into a few fragments of comparable sizes to the parent droplet [51, 52]. This behavior is also termed vibrational breakup and is excluded from the secondary atomization modes by most researchers [48].

The bag breakup is conventionally considered as the first breakup mode and observed over the range $11 < We < 18$ [53, 54]. As sketched in Figure 1.4(b), the droplet deforms into a hollow bag. This thin bag ruptures into fine mist under capillary instabilities, leaving a thick toroidal rim. The rim continues to expand [55] and later disintegrates

into larger fragments. The physical mechanism behind the bag formation is explained by most researchers as Rayleigh-Taylor instabilities developed at the windward surface of the droplet [56–59]. However, some studies propose alternative explanations, including the pressure imbalance between the windward and leeward sides [60–62], the stress repartition around the surface [63] and the structure of flow vortices in the wake [64].

For the shear breakup at $We > 80$ [54, 65], a peripheral sheet develops around the droplet equator as presented in Figure 1.4(d). Micro fragments are then continuously shed off the sheet until the entire droplet is consumed or a small core remains [65]. The physical mechanism of the shear breakup is still under debate. Nicholls and Ranger [66] propose the so-called shear stripping mechanism. They argue that the ambient shear flow induces inside the liquid a boundary layer which becomes unstable at the droplet equator and sheds fragments along the periphery. This argument is supported by the experimental work from Ref. [67–69]. Liu and Reitz [70] postulate an alternative mechanism termed sheet thinning. They state that the peripheral sheet around the droplet equator is bent downstream by the external flow and further disintegrates into ligaments and micro droplets. Experimental results in Ref. [71–73] and numerical simulations in Ref. [60, 61, 74, 75] agree with this mechanism. Theofanous et al. [76] put forward a third theory named shear-induced entrainment and attribute the development of the peripheral sheet to the mass redistribution driven by the shear flow.

For Weber numbers in the intermediate range $18 < We < 80$, there exist several transitional modes which are collectively known as multimode breakup [45, 77]. Two classical multimode morphologies are bag-and-stamen breakup [48, 54, 65] and multibag breakup [58, 78]. In the former morphology, a bag structure similar to that in the bag breakup forms, but an additional streamwise stamen emerges at the center. The stamen disintegrates into large pieces after the fragmentation of the toroidal ring. In the latter morphology, a peripheral sheet develops around the equator in a similar manner to that in the shear breakup. Along the sheet, small bags inflate and rupture continuously until a core is left. The transitional multimode breakup is conventionally understood as a consequence of the competition between the physical mechanisms of bag breakup and shear breakup [50, 76].

In some of the previous research work [79, 80], another so-called catastrophic breakup mode is included in the classification for high relative velocities. But the transitional Weber number varies significantly in different studies, from 350 proposed by Pilch and Erdman [48] to 10000 reported by Hsiang and Faeth [65]. The distinct feature in the catastrophic regime is corrugation at the droplet front. The physical mechanism is explained as the growth of Rayleigh-Taylor instabilities at the windward surface by Joseph et al. [56] and Hwang et al. [81]. They show that the wavelengths predicted by Rayleigh-Taylor instabilities match well the waves measured from shadowgraph images. However, Theofanous and Li [76] present a remarkably smooth central region at the droplet front for high Weber numbers by adopting a different technique of laser-induced fluorescence visualization. They state that the wavy windward surface reported in the previous shadowgraph images is an misinterpreted projected view of complex flow fields and thus negate the existence of this ultimate breakup mode.

Although the Weber number is the dominant parameter in determining the breakup morphology, other non-dimensional quantities exert certain effects on specific breakup behaviors. Chou et al. [67] experimentally investigate the shear breakup with Ohne-

sorge numbers below 0.1, and observe that higher Oh results in larger fragments. Pilch and Erdman [48] analyze the dependence of breakup time on Oh and state that increasing Oh consistently postpones the breakup initiation. The influence of the liquid–gas density ratio

$$\epsilon = \rho_d / \rho_\infty \quad (1.10)$$

on the breakup process is experimentally studied by Lee and Reitz [72] and they conclude that the effect is negligible when ϵ is higher than 100. Kékesi et al. [82] conduct numerical works for density ratios below 100 and observe new breakup patterns. Han and Tryggvason [60, 61] report a backward-facing bag mode in their simulations with $\epsilon = 10$ and state that this mode is absent for density ratios close to unity. Another parameter that has been investigated is the flow Reynolds number

$$Re_\infty = \rho_\infty u_\infty d_0 / \mu_\infty. \quad (1.11)$$

Liu and Reitz [70] carry out experiments over a wide range of Re_∞ above 500 and conclude that the breakup behavior is independent of Re_∞ . Aalburg et al. [83] and Hsiang and Faeth [45] show that the importance of Re to droplet breakup only emerges in Stokes flows and in liquid–liquid breakup systems, respectively. The liquid–gas viscosity ratio

$$\eta = \mu_d / \mu_\infty \quad (1.12)$$

has also been discussed in previous literature [45, 82, 84]. The effect of η on the breakup pattern is concluded to be negligible.

In terms of the experimental methods for the study of droplet breakup, there are three types of widely-adopted facilities: shock tubes [45, 47, 52, 54–58, 65–69, 76, 85, 86], continuous wind tunnels [31, 59, 70–73, 78, 87] and drop towers [63, 88, 89]. Compared to wind tunnels where droplets have to pass a shear layer before reaching the uniform core flow of the continuous jets and drop towers where droplets are accelerated slowly by gravity, shock tubes show the advantage of accelerating the ambient flow around the droplets instantly over a step change to uniform states. Thus, the corresponding initial and boundary conditions are better defined and the results are more suitable for validation of theoretical and numerical studies. Main challenges of shock tube experiments are that the available time window is limited and that the synchronization between the droplet production and the shock generation is critical. Nevertheless, these challenges can be coped with by modifying the test section designs and by adopting suitable mechanisms for diaphragm rupture.

The experimental time t in droplet breakup is typically normalized against the characteristic transport time derived by Ranger and Nicholls [66] to yield the non-dimensional time T

$$T = t \cdot u / (d_0 \sqrt{\epsilon}). \quad (1.13)$$

A convenient relation is consequently obtained to calculate the droplet drag coefficient C_D

$$C_D = \frac{8}{3} \cdot \frac{x/d_0}{T^2}, \quad (1.14)$$

where x is the streamwise displacement of the mass center. However, droplet breakup behaviors under certain conditions cannot be properly characterized by this time scale. For instance, Faeth et al. [49] suggest non-dimensionalizing the experimental time t based on a characteristic viscous time

$$T = t \cdot \rho_{\infty} u_{\infty}^2 / \mu_d \quad (1.15)$$

to analyze the deformation rate at high Oh . Our experiments of droplet breakup in supersonic flow also indicate that the time scaling in Equation 1.13 fails to describe the deformation pattern at high Mach numbers.

There are two time instants of particular significance to characterize the breakup process, namely breakup initiation time and total breakup time. The initiation time is defined by Pilch and Erdman [48] as the instant of the minimum streamwise diameter, and marks the start of the bag inflation at low We and the bending of the peripheral sheet over the rear surface at high We . The total breakup time represents the time required to complete the entire fragmentation process. Several empirical correlations [48, 65, 90] have been proposed for both characteristic times, and are widely used for validation of numerical simulations or comparison with non-conventional breakup behaviors.

1.2 Motivation and Objective

This publication-based thesis aims to take advantage of the well-defined wide-ranging flow conditions generated in a shock tube facility to investigate droplet breakup. The first publication is intended for improving the instrumental technique in pressure measurement to accurately determine the shock-induced freestream conditions and to assess the flow steadiness and uniformity. By exploiting the unique features of the shock-induced flow (such as high Mach numbers and step change in flow conditions), the second and third publications attempt to characterize the droplet breakup behavior in supersonic flow and in tandem formation and to highlight the impacts on relevant practical applications.

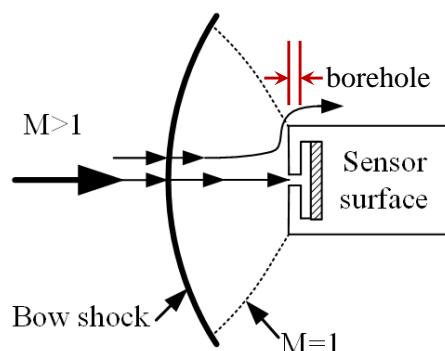


Figure 1.5: Blunt housing geometry and the surrounding flow structures in supersonic flow.

In conventional steady/quasi-steady pressure measurements, housings with conical tips as presented in Figure 1.2 are preferred [19, 91, 92]. The main advantage is that

conical housings exhibit weaker interaction with the ambient flow and exert less influence on the downstream setup. In transient pressure measurements, however, conical housings suffer noticeable drawbacks. The inherent long internal borehole would retard the temporal response of the measured pressure to external flow variations and the high curvature of the detached bow shock would challenge the presumption of normal shock relations. Therefore, we propose alternative housing geometries with blunt tips as sketched in Figure 1.5. The objective of the current work is to evaluate the specific influence of housing geometries on the transient stagnation pressure measurement and to provide general guidance on sensor housing designs. This work is detailed in the peer-reviewed publication [93]

- **Wang, Z.**, Giglmaier, M., Hopfes, T., Köglmeier, L. and Adams, N. A. "Impact of sensor housing geometries on transient stagnation pressure measurements in impulse facilities". In: *Experimental Thermal and Fluid Science* 109 (2019), p. 109851.

which has been attached in Appendix A.1.

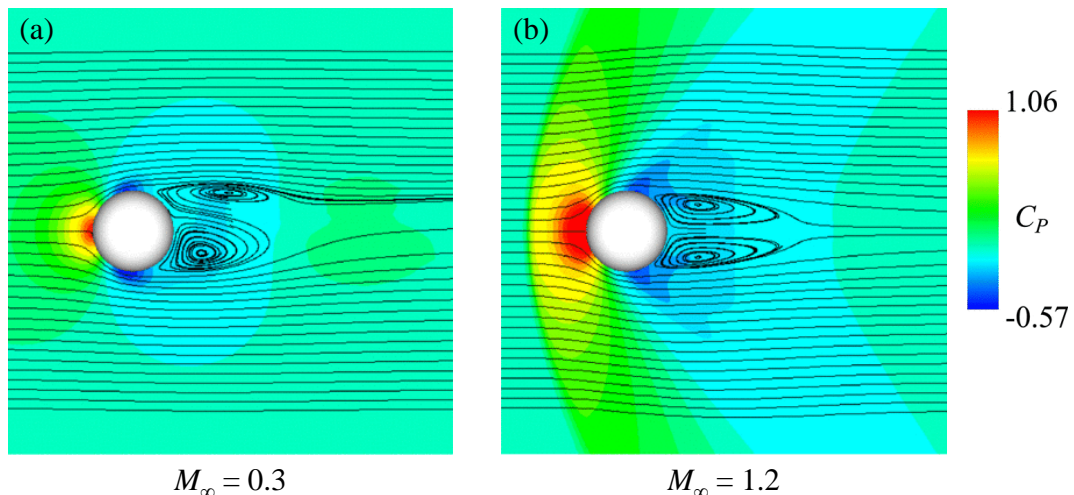


Figure 1.6: Pressure coefficient contours around a sphere at $M_\infty = 0.3$ (a) and $M_\infty = 1.2$ (b). Reproduced from Ref. [94].

In the research field of droplet breakup, most preceding works were conducted under subsonic conditions. However, the rapid development of supersonic combustion systems including pulse detonation engines [95], scramjet engines [96] and supersonic gas atomizers [97] promotes the importance of understanding droplet breakup in high-speed flows. As presented in Figure 1.6 which is reproduced from Ref. [94], the pressure distribution around a sphere is noticeably altered as the ambient flow changes from subsonic to supersonic conditions. The location of the minimum pressure is shifted downstream along the sphere surface, and the relative magnitude of pressure at the rear side is lowered. These changes are expected to affect the behavior of droplet breakup. In the scarce number of studies related to supersonic breakup [58, 85, 98–101], only the early-stage droplet deformation is investigated and the change of flow Mach number is accompanied with varying other non-dimensional parameters. The objective of the current work is to address the influence of the flow Mach number on droplet breakup patterns independently of Weber and Reynolds numbers and to shed

light on the underlying physics in supersonic atomization. This work is detailed in the peer-reviewed publication [14]

- **Wang, Z.**, Hopfes, T., Giglmaier, M. and Adams, N. A. "Effect of Mach number on droplet aerobreakup in shear stripping regime". In: *Experiments in Fluids* 61.9 (2020), pp. 1-17.

which has been attached in Appendix A.2.

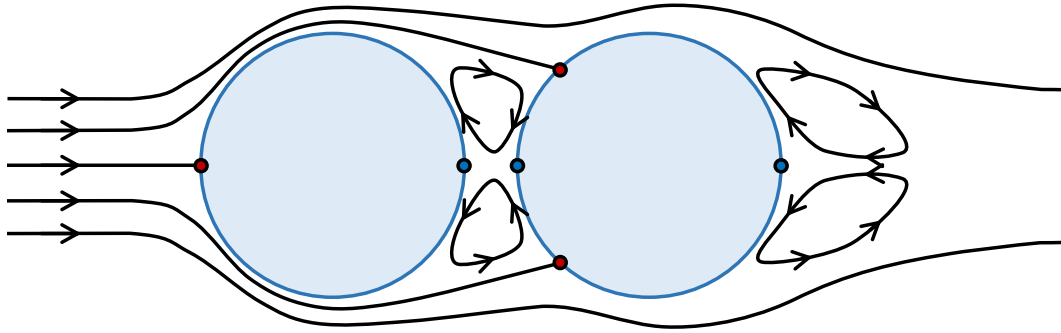


Figure 1.7: Simplified 2D sketch of streamlines around tandem droplets. Stagnation points of the highest pressure are labeled in red and those of lower pressure in blue.

In dense spray-related applications such as diesel injections [102] and agricultural sprays [103], droplets are distributed in close proximity. As indicated by the simplified streamlines around two adjacent droplets in Figure 1.7, the tandem formation reduces the pressure imposed on the front of the downstream droplet and moves the highest pressure to locations near the equator. This shielding effect exerted by the upstream droplet is expected to alter the breakup structure of the downstream droplet. Previous studies of droplet breakup in tandem formation [85, 87, 104–106] report distinct features from conventional isolated droplet breakup. However, the numerical works among them fail to model detailed breakup structures and the experimental works cover very limited breakup conditions and only draw qualitative conclusions. The objective of the current work is to investigate the breakup features of tandem droplets over a wide range of Weber numbers and separation distances and to provide quantitative bases for more accurate modeling of dense sprays. This work is detailed in the peer-reviewed publication [15]

- **Wang, Z.**, Hopfes, T., Giglmaier, M. and Adams, N. A. "Experimental investigation of shock-induced tandem droplet breakup". In: *Physics of Fluids* 33 (2021), p. 012113.

which has been attached in Appendix A.3.

1.3 Outline

The present thesis is structured as follows. Chapter 1 illustrates the fundamental principles of the shock tube facility as well as the associated pressure measurement techniques, and introduces the state of the art in droplet breakup morphologies. The motivation of the thesis and the objective of each specific topic are also included. Chapter 2

presents the experimental facilities and the measurement systems adopted in the current study and provides detailed quantities of the experimental matrices. Chapter 3 summarizes the main findings in the three publications on which this thesis is based. The discussions in Chapter 5 highlight the key features of the current work compared to previous literature and the outlooks in Chapter 6 list the relevant potential topics for future research.

2 Experimental Methods

This chapter summarizes the main experimental methods employed in the present work, including a shock tube facility for generation of uniform gas flow, a pressure measurement system for determination of flow conditions, a schlieren/shadowgraph photography system for visualization of wave dynamics and a droplet generation setup. Experimental matrices for the three topics covered in this publication-based thesis are also provided to complete this chapter.

2.1 Shock Tube

The layout of the shock tube adopted in this work is depicted in Figure 2.1. The driver and driven sections are 3 m and 21 m long, respectively. Both have an inner diameter of 290 mm. A 0.5 m-long test section locates in the downstream segment of the driven section. A cookie-cutter is installed in front of the test section to reduce the cross section to a square with the side length of 190 mm and to separate boundary layers from the uniform core flow.

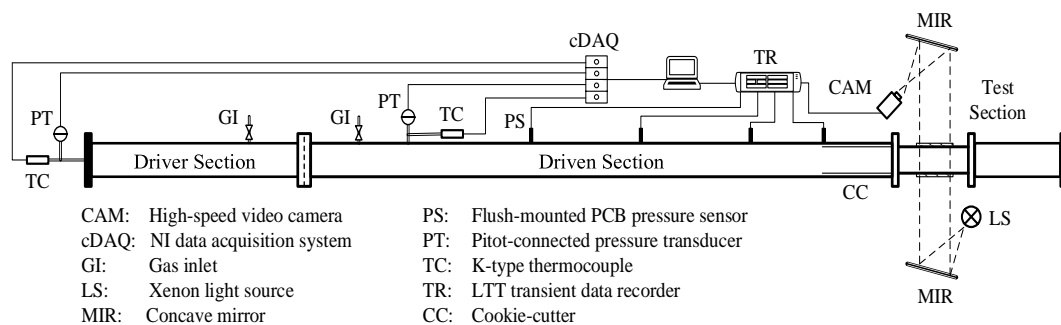


Figure 2.1: Sketch of the shock tube and the measurement system.

For high-pressure experiments ($2 \text{ bar} < p_4 - p_1 < 7 \text{ bar}$), the thin diaphragm is made from aluminum and ruptured by a sharp X-shape steel blade as the driver section is filled up to a critical pressure. For low-pressure experiments ($0.1 \text{ bar} < p_4 - p_1 < 2 \text{ bar}$), plastic Mylar diaphragms are utilized. A pair of 0.1 m-thick crossed NiCr heating wires are positioned in contact with the diaphragm and melt its two diagonals once a 3 A electric current is supplied. A main advantage of the latter rupture mechanism is that the incident shock is generated at an accurately controlled timing and at a precisely defined driver pressure. An accompanying challenge is that the Mylar diaphragms tend to break into a number of pieces scattered along the shock tube, which adds more difficulties to the tube cleaning.

The ideal wave dynamics inside the shock tube have been exemplified in Figure 1.1. However, due to the change of the cross section area at the inlet of the test section, additional wave motions emerge and reduce the duration of steady flow conditions. The simplified wave dynamics in the present setup are sketched in Figure 2.2(a). As the core part of the incident shock enters the test section, the peripheral part propagates into the narrow gap between the cookie-cutter and the tube wall and reflects at the root of the cookie-cutter. Later as the incident shock reaches the end of the test section, the increase of the cross section area induces additional expansion waves. Both the reflected shock and the expansion waves disturb the mainstream flow in the test section and limit the available experimental time. An exemplary pressure signal measured at the indicated test location is presented in Figure 2.3, of which the measurement setup will be illustrated in Section 2.2. After a step increase through the incident shock, the pressure remains steady for 2.1 ms.

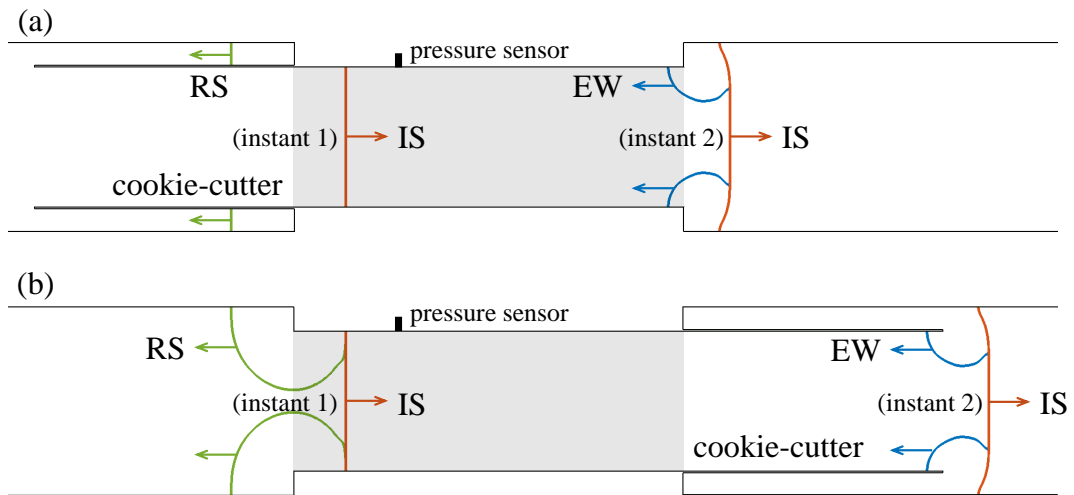


Figure 2.2: Simplified sketch of wave motions around the test section at two time instants, with the cookie-cutter positioned upstream (a) and downstream (b). The test section is marked with gray shades, The incident shock propagates from left to right. (IS: incident shock, RS: reflected shock, EW: expansion wave).

The time window of steady flow conditions is sufficient for most of the studies carried out in this work. Solely for droplet breakup at very low Weber numbers, the complete breakup process exceeds 2.1 ms. For these experiments, the cookie-cutter is shifted from upstream to downstream of the test section to prolong the time window. The corresponding wave dynamics are sketched in Figure 2.2(b) and the pressure signal is provided in Figure 2.3. In this new setup, the peripheral part of the incident shock reflects at the front of the test section and directly interacts with the mainstream flow, which leads to a short transition period (approximately 0.2 ms) in the pressure signal. The pressure settles down shortly at a higher level than that in the previous setup. With the region of constant cross section extended further downstream by the cookie-cutter, the generation of expansion waves is postponed and the mainstream flow remains steady for 4.5 ms until the up-traveling expansion waves reach the test location. Thus, the available experimental time is greatly prolonged at the expense of causing an additional transition period and relatively high flow fluctuations.

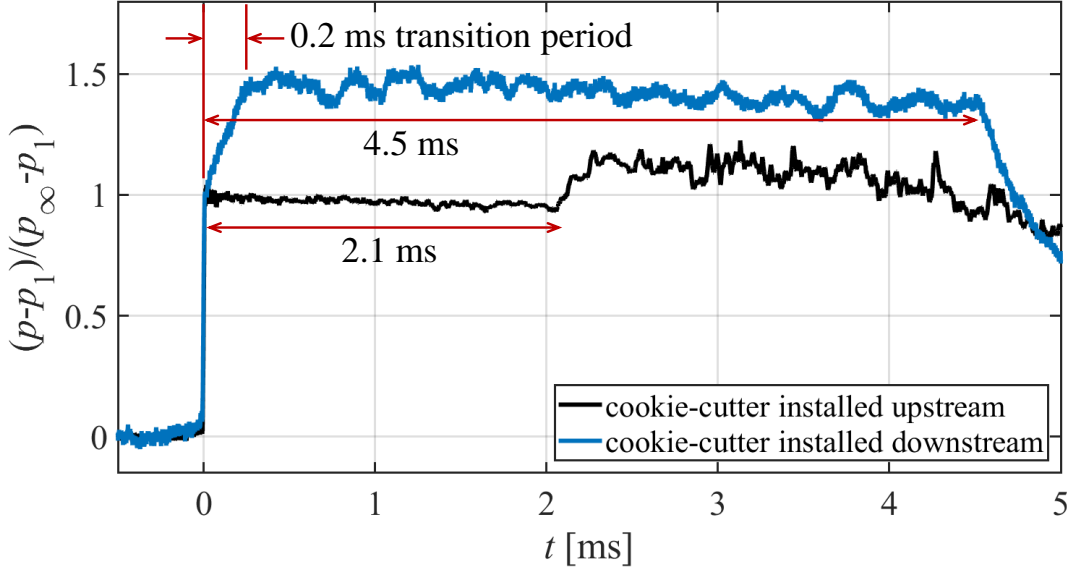


Figure 2.3: Exemplary pressure signals measured inside the test section. The pressure is normalized by theoretical values. The steady-flow time window is extended from 2.1 ms to 4.5 ms by positioning the cookie-cutter from upstream to downstream.

2.2 Pressure Measurement System

Pressure changes inside the driver and driven sections during the preparation phase (including filling and evacuation) are tracked by two pressure gauges, as sketched in Figure 2.1. An NI™ cDAQ device acquires the signals from which the driver pressure p_4 and the driven pressure p_1 at the time instant of shock generation are extracted. Due to pressure loss in flow mixing and viscous dissipation of the shock propagation, the experimental incident shock strength is weaker than that derived from the ideal relation Equation 1.1. Thus, although the measured p_1 will still be used in the following calculation of shock-induced freestream conditions, p_4 only serves as a qualitative indicator.

To accurately determine the incident shock strength, the shock propagation along the driven section and the pressure inside the test section are monitored by flush-mounted PCB Piezotronics ICP® fast-response sensors. These sensors show a resonant frequency above 500 kHz and rise time below 1 μ s. An LTT data acquisition device records the pressure data at a sampling rate of 1 MHz. Exemplary pressure signals have been presented in Figure 2.3. Given that the separation distance between the two sensors installed directly upstream of the test section is 0.75 m, the incident shock speed u_s is yielded by measuring the time lag between instants of the shock passing them. The corresponding shock Mach number M_s is obtained through dividing u_s by the speed of sound calculated from the driven gas temperature (which is normally the room temperature). Then, the shock-induced freestream pressure p_∞

$$p_\infty = p_1 \cdot \frac{2\gamma M_s^2 - (\gamma - 1)}{\gamma + 1}, \quad (2.1)$$

density ρ_∞

$$\rho_\infty = \rho_1 \cdot \frac{(\gamma + 1)M_s^2}{(\gamma - 1)M_s^2 + 2}, \quad (2.2)$$

velocity u_∞

$$u_\infty = u_s \cdot \frac{2M_s^2 - 2}{(\gamma + 1)M_s^2}, \quad (2.3)$$

and Mach number M_∞

$$M_\infty = \frac{2M_s^2 - 2}{\sqrt{(2\gamma M_s^2 - (\gamma - 1))((\gamma - 1)M_s^2 + 2)}} \quad (2.4)$$

are derived from the moving shock relations.

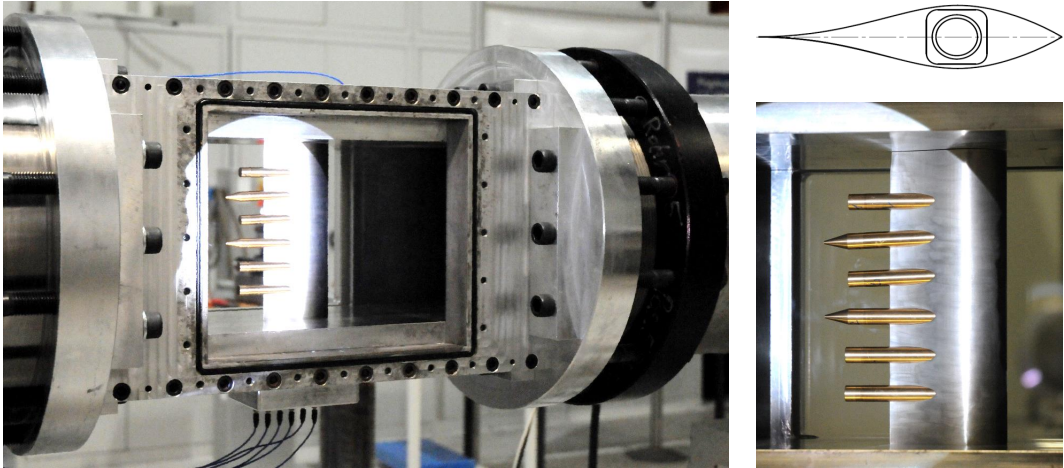


Figure 2.4: Experimental Pitot rack for the stagnation pressure measurement in the test section. The incident shock arrives from left.

As previously demonstrated in Figure 2.3, the freestream pressure p measured in the current setup agrees well with the theoretical value p_∞ derived from Equation 2.1 and shows good temporal constancy. To further quantify the spatial uniformity of the freestream flow, a rack of Pitot probes are assembled inside the test section as depicted in Figure 2.4. The rack is built based on a modified Guderley profile [107] to weaken the interaction with the incident shock wave and to avoid the formation of additional shocks. Six Pitot probes equipped with pressure sensors are spaced evenly along the rack and the interaction between the probes is experimentally verified to be negligible. The second and third upper slots in the rack are manufactured with a 2° downward inclination to investigate the effect of mounting misalignment. The freestream stagnation pressure measured by the other four straight Pitot tubes are exemplified in Figure 2.5. The signals are in good consistency with the theoretical value $p_{0\infty}$ calculated from the isentropic relation Equation 1.4 and verify the flow uniformity in the test section.

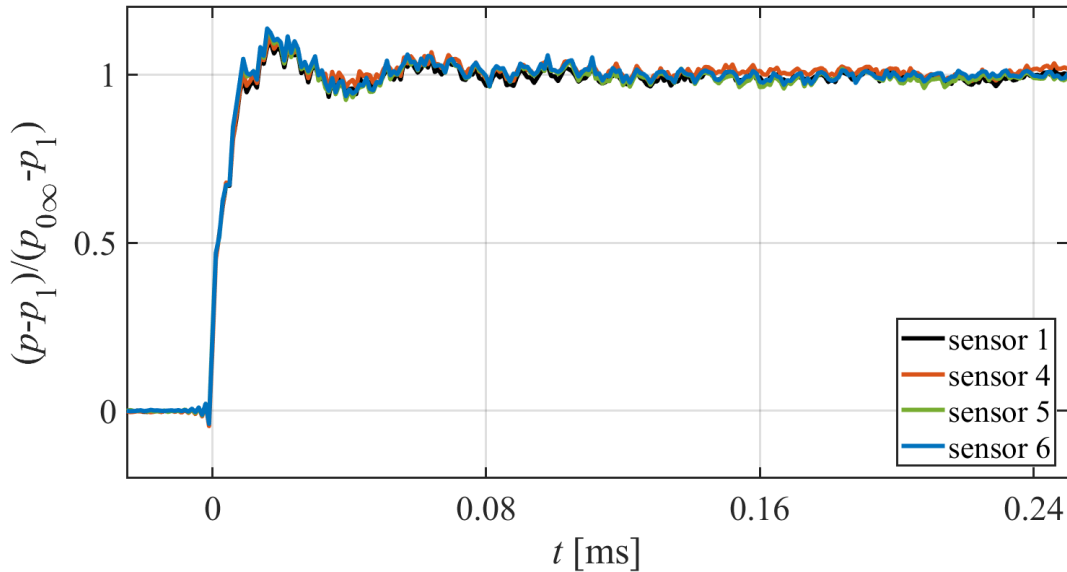


Figure 2.5: Exemplary stagnation pressure signals measured by sensors embedded in the Pitot rack. The sensors are numbered from top to bottom.

2.3 Schlieren/Shadowgraph Photography

The present work employs a Z-type schlieren system, which is sketched in Figure 2.6, for visualization of wave motions in the flow field. In this photography system, the light emitted from a 150 W Xenon lamp is converged by a series of lenses (labeled as lens I) and forms a point light source at the aperture. The light is projected on an aluminum-coated parabolic mirror (diameter of 26 cm and focal length of 2.5 m) and transforms into a parallel light beam. This light beam passes through the test section where high-transparency glass windows (19 cm in height and 40 cm in length) are installed at both sides to provide optical access, and is then focused by another identical parabolic mirror on a sharp knife edge. Eventually a second set of lenses (labeled as lens II) cast the light on the sensor chip of a Shimadzu HyperVision HPV-X ultra-high-speed camera. A total number of 128 consecutive images are recorded with a spatial resolution of 250×400 pixels and a framing rate up to 1 Mfps.

In the schlieren photography system, the lens I determines the illuminated area of the test section and the lens II regulates the zooming of the camera imaging. The setup sensitivity to flow disturbance is controlled by adjusting the amount of light blocked by the knife edge. However, increasing the sensitivity is accompanied with reduction in the image brightness and blurring of the gas-liquid or gas-solid interface. Therefore, for droplet experiments where the deformation needs to be accurately quantified, the knife edge is removed and the system is simplified to shadowgraph photography.

The post-processing methods for the recorded schlieren/shadowgraph images have been standardized in the current work, including background subtraction, contrast adjustment and super resolution using MATLAB's Very Deep Super-Resolution convolutional neural network [108]. A set of MATLAB packages are also developed to trace positions of pixels that constitute the droplet in images and thus to calculate various deformation quantities such as the cross-stream diameter and the streamwise displacement.

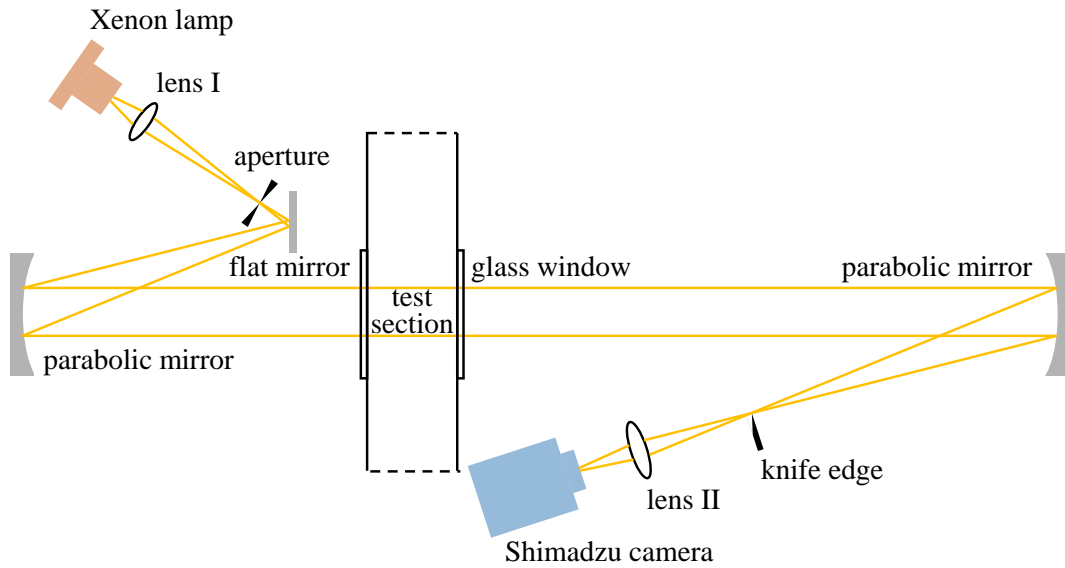


Figure 2.6: Layout of the Z-type schlieren/shadowgraph system.

2.4 Droplet Generation

In the present work, droplets are produced by expelling liquids through syringe needles that are inserted into the test section. For single droplet experiments, droplets detach from the needle tip when the diameter reaches a critical point and the weight overcomes the surface tension force. For tandem droplet experiments where the detachment of the two droplets needs to be synchronized, droplets of desired diameters are first produced hanging at needle tips and the syringes are then withdrawn rapidly shedding the droplets simultaneously.

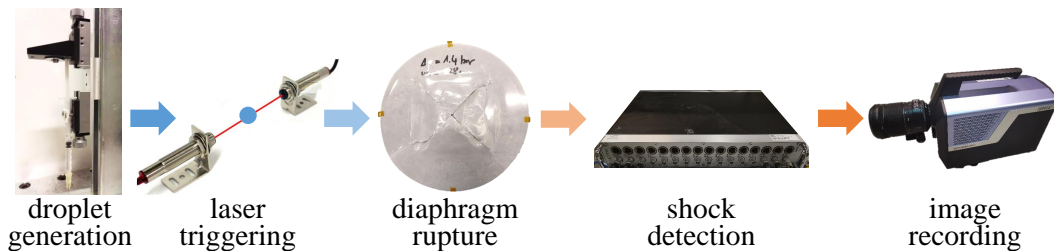


Figure 2.7: Workflow of droplet breakup experiments.

Droplet generation is the last step in the preparation phase of experiments and initiates the automated workflow shown in Figure 2.7. The generated droplet falls through an aligned pair of laser emitter and receiver and triggers the associated electronic switch to supply powers to NiCr heating wires. These heating wires melt the Mylar diaphragm that separates driver and driven sections and then a planar shock wave forms. A pressure sensor flush-mounted in the test section detects the arrival of the incident shock and a trigger signal is sent to the camera to start image recording after a preset delay. The timing of each step in the automated workflow is carefully regulated to make sure that both the instant of the incident shock impacting the free falling droplet and the subsequent breakup process are captured by the camera.

2.5 Experimental Matrix

2.5.1 Sensor housing design for total pressure measurement

In the study of impacts of sensor housing geometries on transient stagnation pressure measurements, housings with blunt and conical tips are compared. Figure 2.8 presents drawings of the cross-section geometry and provides detailed dimensions that are normalized against the sensor tip diameter $h = 5.54$ mm. The conical housing is designed with a 15° taper angle which naturally leads to a significantly longer borehole ($L = 3.11$) than the blunt housing ($L = 0.23$). The borehole diameter D is varied among 0.36 (default), 0.45 and 0.54 and the cavity depth G among 0.045 (default), 0.12 and 0.19. To investigate the effect of mounting misalignment, the second and third upper slots in the Pitot rack presented in Figure 2.4 are manufactured with a 2° downward inclination.

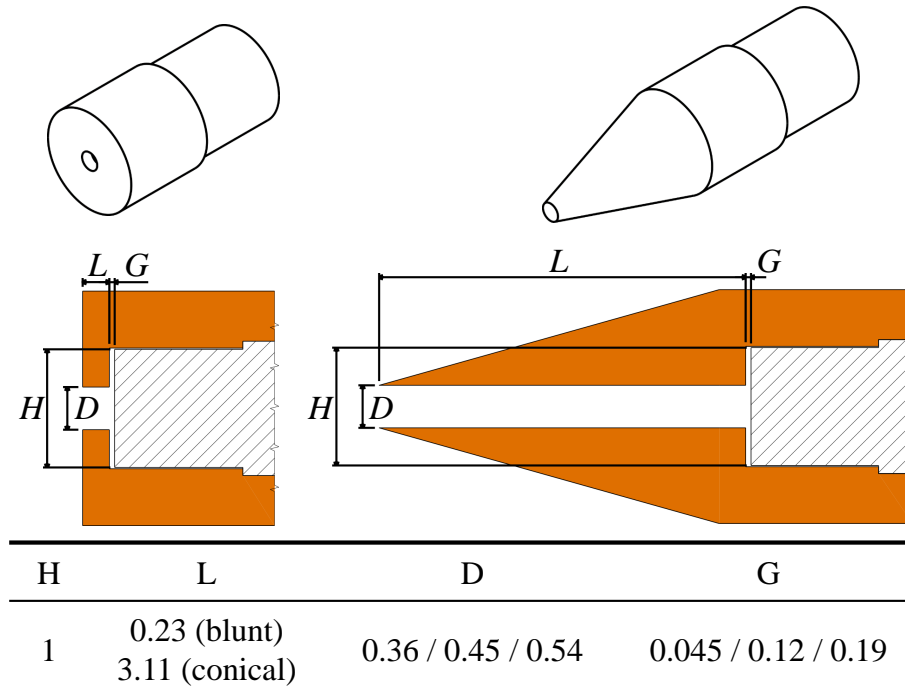


Figure 2.8: Dimensions of blunt and conical housings (orange colored) normalized by the sensor tip diameter $h = 5.54$ mm. The shaded regions represent the pressure sensors.

The performance of each housing design is evaluated under three distinct flow conditions as listed in Table 2.1. The driver pressure p_4 is maintained at 7 bar for all cases and the driven pressure p_1 is adapted to achieve pressure ratios PR of 10, 100 and 1000. The corresponding freestream Mach number M_∞ in the test section increases from 0.6 (subsonic) to 1.36 (supersonic). The freestream Reynolds number $Re_{\infty,D}$ is calculated based on the default housing borehole diameter $D = 0.36$ (2 mm) and decreases from 25000 to 700.

Table 2.1: Operating flow conditions averaged from 4 repeated experiments for the stagnation pressure measurement.

$PR = p_4/p_1$	M_s	M_∞	u_∞ (m/s)	$Re_{\infty,D}$
10 ($\pm 3\%$)	1.50	0.60	241	25000
100 ($\pm 2\%$)	2.24	1.08	518	4800
1000 ($\pm 5\%$)	3.01	1.36	775	700

2.5.2 Droplet breakup in supersonic flow

In the study of droplet breakup in supersonic flow, the effect of flow Mach number M_∞ on the breakup pattern is investigated independently of flow Reynolds number Re_{∞,d_0} and Weber number We . To achieve this objective, two liquids (ethylene glycol and water) and two gases (air and CO_2) are used and different combinations between them allow to decouple the correlation between M_∞ , Re_{∞,d_0} and We . For all cases, the Weber number is constrained within the interval 1100 ± 60 , which maintains a stripping breakup mode for droplets and renders a wide variation of M_∞ and Re_{∞,d_0} possible. The corresponding inversely-proportional relations between M_∞ and Re for different liquid–gas combinations are plotted in Figure 2.9. The present work covers eight operating conditions that are labeled in the plot. The associated gray error bars represent variations of M_∞ and Re_{∞,d_0} from repeated experiments. The eight operating conditions are numbered as $i.j$, with the values of i and j standing for the relative magnitudes of M_∞ and Re_{∞,d_0} , respectively. Table 2.2 summarizes main non-dimensional quantities averaged from repeated experiments for each operating condition.

Table 2.2: Operating conditions averaged from 5 repeated experiments for the droplet breakup in supersonic flow.

Case	Liquid	Gas	We	Oh	Re_{∞,d_0}	M_∞
1.4	E.G.	Air	1060	0.042	2.4e4	0.30
2.3	E.G.	Air	1056	0.044	8.6e3	0.63
3.2	E.G.	Air	1120	0.043	5.9e3	0.83
5.1	E.G.	Air	1050	0.044	2.6e3	1.19
3.3	Water	Air	1160	0.002	9.5e3	0.83
4.3	E.G.	CO_2	1100	0.044	8.8e3	0.94
5.2	E.G.	CO_2	1120	0.043	5.9e3	1.19
5.3	Water	CO_2	1080	0.002	8.6e3	1.19

The average droplet diameter d_0 is 3.1 mm for water ($\rho_d = 998 \text{ kg/m}^3$, $\sigma = 7.28\text{e-}2 \text{ N/m}$, $\mu_d = 8.9\text{e-}4 \text{ kg/m-s}$) and 2.6 mm for ethylene glycol ($\rho_d = 1113 \text{ kg/m}^3$, $\sigma = 4.73\text{e-}2 \text{ N/m}$, $\mu_d = 1.61\text{e-}2 \text{ kg/m-s}$). The corresponding Ohnesorge numbers are around 0.002 and 0.043, of which both are significantly lower than 0.1.

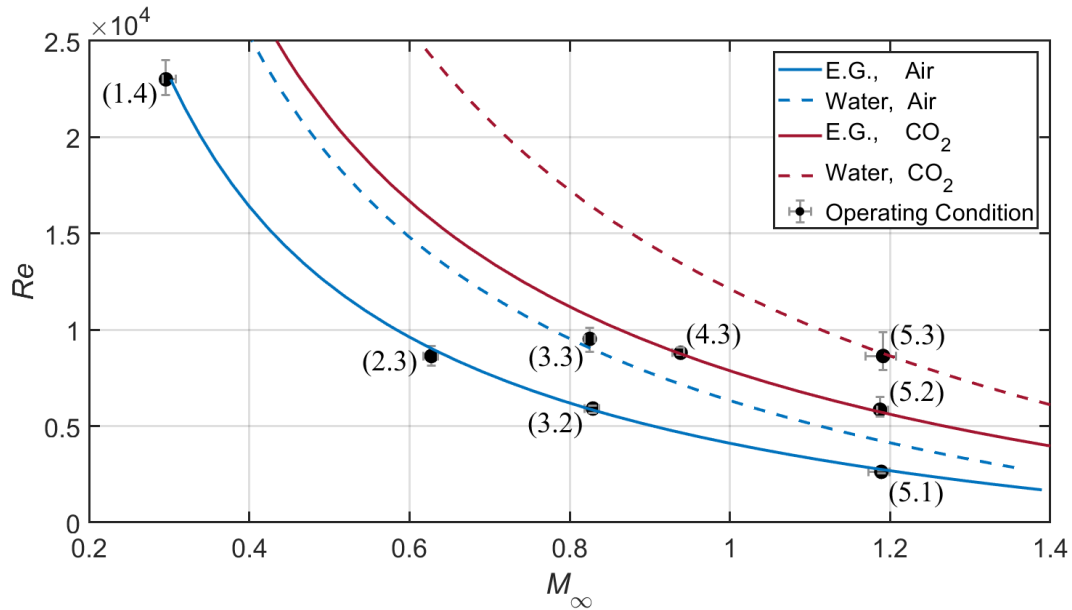


Figure 2.9: Inversely proportional correlation between M_∞ and Re_{∞,d_0} at $We = 1100$. Each line corresponds to a certain liquid–gas combination. The eight operating conditions are labeled as $i.j$, with i and j representing the relative magnitudes of M_∞ and Re_{∞,d_0} respectively. The associated error bars stand for the ranges of conditions from repeated experiments and are magnified twice in the plot for a clearer display.

Therefore, the effect of liquid viscosity on the breakup morphology is negligible. Over the test matrix, the freestream Mach number ranges from subsonic ($M_\infty = 0.3$) to supersonic ($M_\infty = 1.19$) levels and the Reynolds number varies between $Re_{\infty,d_0} = 2.6e3$ and $Re_{\infty,d_0} = 2.4e4$.

Main comparisons are made between Case 1.4, 2.3, 3.2 and 5.1 that employ the same liquid and gas, to present overall influences of M_∞ and Re_{∞,d_0} on the stripping breakup behavior. Further analyses of Case 2.3, 4.3 and 5.3 that have comparable Re_{∞,d_0} but different M_∞ shed light on the exclusive role played by M_∞ in the breakup process. Similarly, the effect of Re_{∞,d_0} is highlighted by comparing identical- M_∞ cases 5.1, 5.2, and 5.3.

2.5.3 Droplet breakup in tandem formation

In the study of tandem droplet breakup, droplets are made of water and generated with diameters around $d_0 = 2$ mm. Experiments are conducted at four distinct flow conditions, with the initial driven pressure inside the test section maintained at atmosphere pressure. Table 2.3 presents the main non-dimensional parameters averaged from repeated experiments.

The Weber numbers are controlled at $13(\pm 1.3)$, $24(\pm 2.2)$, $70(\pm 3.0)$ and $180(\pm 10)$. The corresponding breakup morphology is bag, bag-and-stamen, multibag and shear stripping breakup, respectively. The Ohnesorge number for all cases is approximately $2.4e-3$, indicating that the viscous effect is negligible. The d_0 -based flow Reynolds number Re_{∞,d_0} increases from $2.5e3$ to $1.0e4$ and stays within the laminar region.

For each breakup morphology, seven initial on-center separation distances s are investigated, ranging from 1.2 to 10.5 times of the initial droplet diameter. The vertical

Table 2.3: Operating flow conditions averaged from 10-20 repeated experiments for the droplet breakup in tandem formation.

We	Oh_{avg}	$Re_{\infty, d_0 \text{avg}}$	breakup morphology
13(± 1.3)	2.4e-3	2.5e3	bag breakup
24(± 2.2)	2.4e-3	3.4e3	bag-and-stamen breakup
70(± 3.0)	2.3e-3	6.1e3	multibag breakup
180(± 10)	2.4e-3	1.0e4	shear stripping breakup

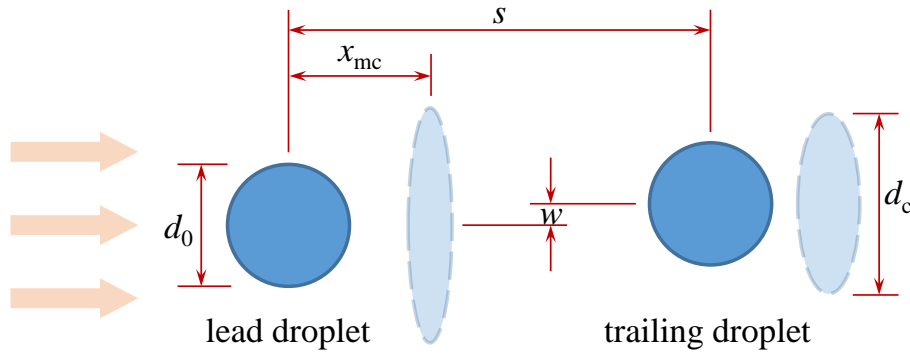


Figure 2.10: Sketch of droplets in tandem formation. Dark blue spheres and light blue ellipsoids represent initial states and deformed states of the droplets, respectively. The freestream direction is from left to right. (s : initial separation distance, w : initial vertical misalignment, d_0 : initial droplet diameter, d_c : cross-stream diameter, x_{mc} : streamwise displacement of the mass center).

misalignment w between the tandem droplets is limited under $0.2d_0$. As sketched in Figure 2.10, according to the freestream direction, the upstream and downstream droplets are referred to as lead and trailing droplets. Definitions of commonly analyzed quantities including the cross-stream diameter d_c and the streamwise displacement of the mass center x_{mc} are also indicated in the figure. With current framing rates and spatial resolutions of the recorded images, the uncertainty for temporal and spatial calculations is $\pm 1.3\%$ and $\pm 1.5\%$, respectively.

3 Summary of Publications

In this chapter, the three first-author peer-reviewed publications on which this dissertation is based are summarized.

3.1 Impact of Sensor Housing Geometries on Transient Stagnation Pressure Measurements in Impulse Facilities

Z. Wang, M. Giglmaier, T. Hopfes, L. Köglmeier, N. A. Adams

3.1.1 Summary of the publication

To provide general guidance on sensor housing designs in transient stagnation pressure measurements, this paper makes a thorough comparison between conical and blunt housings. The key finding is that housings with blunt tips and short internal void are preferred over those with conventional conical tips to achieve robust high-accuracy fast-response measurements.

Figure 3.1(a) sketches the simplified wave dynamics inside the void of the conical housing under impact of the incident shock. The corresponding pressure signal measured by the embedded sensor is plotted in Figure 3.1(b). Part of the incident shock propagates into the housing void and reflects back and forth between the sensor surface (solid boundary) and the housing tip (free surface). These cyclic wave motions give rise to the large-amplitude oscillation in the measured pressure signal. The oscillation gradually subsides as the wave strength decays through energy exchange with the external flow and viscous dissipation.

The wave dynamics inside the blunt housing occur in a similar pattern but at a much faster rate due to the significantly shorter void. The corresponding pressure signal is shown in Figure 3.1(c) and is highly preferable to that measured by the conical housing. The rise time is almost halved, because the blunt tip induces stronger shock reflection at the housing front and the resultant higher pressure initiates a steeper pressure rise. The overshoot is significantly dampened and the settling time is reduced approximately by 10 times, for the shorter housing void allows more efficient communications between the internal flow and the external free stream and thus restrains the housing void from being over-filled or over-drained.

As indicated previously in Figure 1.2, the housing void is composed of a borehole and a cavity. Both increasing the borehole diameter and decreasing the cavity depth accelerate the filling process of the void. This effectively reduces the rise time of the measured pressure signal but tends to overfill the void to higher overshoot. Therefore,

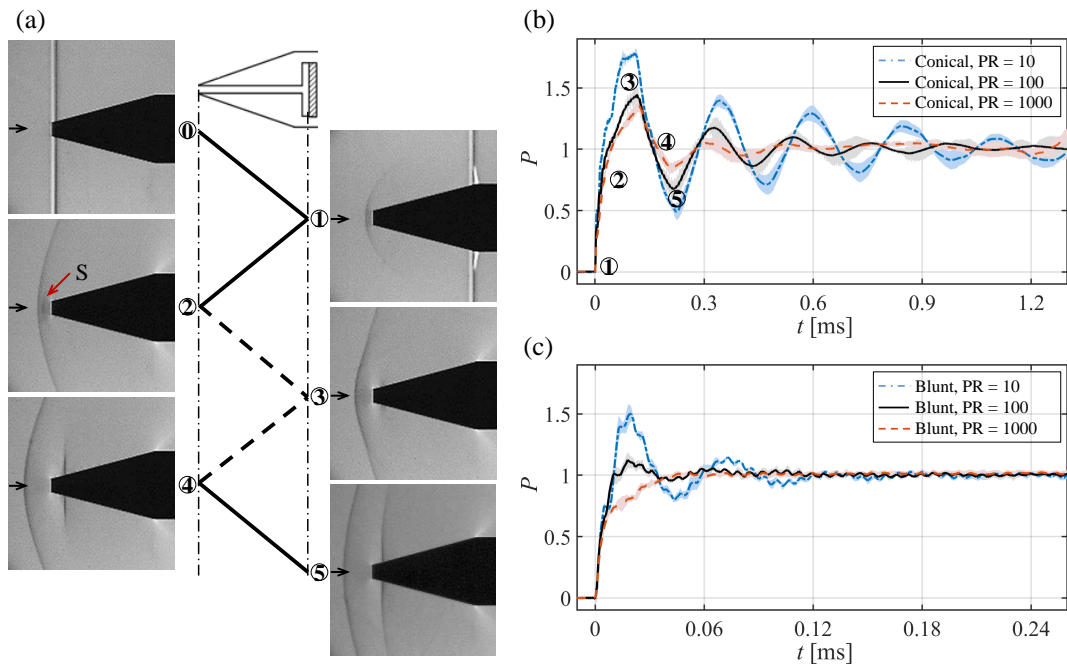


Figure 3.1: Sketch of the wave dynamics inside the conical housing and schlieren images of the wave motions outside (a). Solid lines represent shock waves and dashed lines expansion waves. Normalized pressure signals for conical (b) and blunt (c) housings at different flow conditions are presented with the shadowed ribbons indicating the measurement variation.

the volume ratio between the borehole and the cavity serves as a general indicator for the housing design to balance the signal behavior.

The influences of additional practical factors are also evaluated. The blunt housing maintains a higher measurement accuracy than the conical housing when the assembly is misaligned or the sensor surface is not properly shielded.

3.1.2 Individual contributions of the candidate

This article [93] was published in the peer-reviewed journal *Experimental Thermal and Fluid Science*. My contributions to this publication included carrying out experiments and performing numerical simulations. I verified the experimental methods, and analyzed the data by adapting post-processing tools. The original manuscript was written by me.

3.2 Effect of Mach Number on Droplet Aerobreakup in Shear Stripping Regime

Z. Wang, T. Hopfes, M. Giglmaier, N. A. Adams

3.2.1 Summary of the publication

To address the importance of flow compressibility in supersonic atomization, the present experimental work compares the stripping breakup of liquid droplets in subsonic and supersonic flows. The key feature is that the flow Mach number M_∞ is varied independently of Weber and Reynolds numbers. The main finding indicates that increasing M_∞ alters the stripping breakup pattern and changes the fragment size distribution.

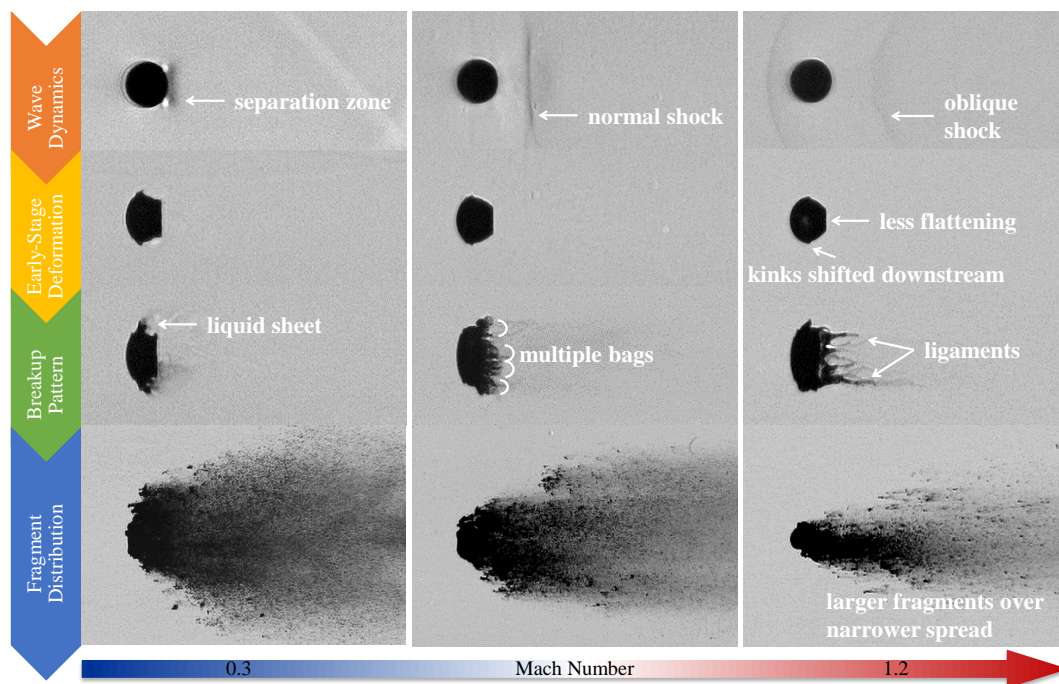


Figure 3.2: Summary of differences in the stripping breakup of droplets in subsonic and supersonic flows. The Weber number is maintained at 1100. The length scale of images in the last row is half of that in the first three rows.

Figure 3.2 presents the stripping breakup at subsonic and supersonic conditions with the Weber number maintained at 1100. The breakup process is divided into four stages that describe wave dynamics, early-stage deformation, breakup pattern and fragment distribution, respectively.

In terms of the initial wave dynamics, a distinct normal shock or an oblique shock cone emerges behind the droplet at higher flow Mach numbers. This confirms that the pressure imposed on the spherical surface differs significantly as M_∞ changes [109, 110]. These differences are held accountable for the more pronounced distinctions in succeeding deformation and breakup processes [111].

During the early-stage deformation, kinks form around the droplet equator, which are the origins of succeeding liquid sheets. As M_∞ increases, the position of the kink is shifted considerably downstream and follows the trajectory of the separation point

at the surface of a solid sphere as measured by Charters and Thomas [109]. Meanwhile, flattening of the leeward surface becomes significantly weaker, which could be associated to the observation by Karyagin et al. [112] that the pressure imposed on a sphere rear decreases consistently as the flow accelerates to supersonic conditions. Another noteworthy tendency is that the liquid sheet grows more rapidly at lower M_∞ . Our experiments show that the growth of the liquid sheet is enhanced by the gathering of propagating waves at the droplet surface, which has also been reported by Theofanous et al. [86] and Jalaal and Mehravaran [113]. These surface waves tend to be suppressed in supersonic flows by the compressibility effect [114–116].

As to the breakup pattern, the droplet in subsonic flow exhibits typical stripping features. Micro-drops are stripped off the peripheral sheet and entrained in the flow. For the droplet in transonic flow, however, the breakup onset is characterized by the formation of multiple bags along the peripheral sheet. As the sheet initially extends downstream, the rim is straightened directly facing the freestream flow and the development of Rayleigh-Taylor instabilities gives rise to bag formation similarly to the jet breakup simulated by Shinjo and Umemura [117]. In supersonic flow, the droplet breakup initiates with the generation of thin and long streamwise ligaments in the wake. These ligaments result from the development of streamwise vortical waves at the peripheral sheet [118] which is stretched along the flow direction and becomes increasingly sensitive to surface instabilities.

In the late stage, the droplet at subsonic conditions fragment into uniformly fine mist dispersed widely in the cross-stream direction. At supersonic conditions, however, disintegration of ligament structures results in relatively large fragments. Meanwhile, folding of the peripheral sheet reduces the cross-stream momentum gained by the fragments and thus significantly narrows their spatial dispersion.

3.2.2 Individual contributions of the candidate

This article [14] was published in the peer-reviewed journal *Experiments in Fluids*. My contributions to this publication included designing the experimental methodology and carrying out the experiments. I verified the experimental methods and analyzed the data by adapting post-processing tools. The original manuscript was written by me.

3.3 Experimental Investigation of Shock-Induced Tandem Droplet Breakup

Z. Wang, T. Hopfes, M. Giglmaier, N. A. Adams

3.3.1 Summary of the publication

To assess the significance of droplet interaction in dense sprays, the current study investigates the droplet breakup in tandem formation. The important contribution of this work is the quantification of experimental results over a wide range of Weber numbers and separation distances. A main conclusion is that the breakup of the trailing droplet is greatly dampened or even completely suppressed by the lead droplet in close proximity.

An overview of the interactive modes between the tandem droplets at different separation distances S and Weber numbers We is summarized in Figure 3.3. Since the lead droplet breakup is marginally influenced by the tandem formation, Figure 3.3 only categorizes the change of the breakup pattern for the trailing droplet. The entire $S-We$ map is divided into three regions.

The independent breakup region at the top-right corner represents cases where the trailing droplet undergoes the same breakup process as the lead droplet. The solid borderline in Figure 3.3(a) is of particular importance, because it marks the critical separation distance below which the interaction between the tandem droplets has to be taken into account. This critical distance is We -dependent and halved from $S = 10.8$ at $We = 13$ to $S = 5.4$ at $We = 180$.

The transition region covers conditions at which the trailing droplet fragments in the same morphology as the lead droplet but the breakup intensity is weakened, as presented in Figure 3.3(b). The wake of the lead droplet exerts shielding effects on the trailing droplet and greatly reduces the pressure imposed on its frontal surface. In low- We breakup morphologies, the shielding effect results in less pronounced flattening for the trailing droplet and further yields a smaller bag size. In high- We breakup morphologies, the shielding effect dampens the outward burst of tiny bags around the periphery and thus narrows the cross-stream dispersion of the fragments. The reduction of bag sizes and the contraction of fragment dispersion are intensified as the separation distance decreases.

The suppressed breakup region at the bottom-left corner of the $S-We$ map contains cases where the shielding effect is so strong that the trailing droplet fails to follow the conventional breakup morphology. For instance, the trailing droplet punctures the bag structure of the lead droplet at $We = 13$ and coalesces into the stamen-like structure of the lead droplet at $We = 70$, as shown in Figure 3.3(c). For both puncture and coalescence modes, the trailing droplet is not atomized into fine mist but disintegrates into fragments with sizes comparable to the initial diameter.

Further quantitative analyses indicate that the tandem formation postpones the breakup initiation of the trailing droplet, reduces the maximum cross-stream diameter and lowers the mean drag coefficient. All these effects become less pronounced as the Weber number increases, because the deformation of the lead droplet transitions from a disk to an ellipsoid and the shielding effect on the trailing droplet is weakened correspondingly.

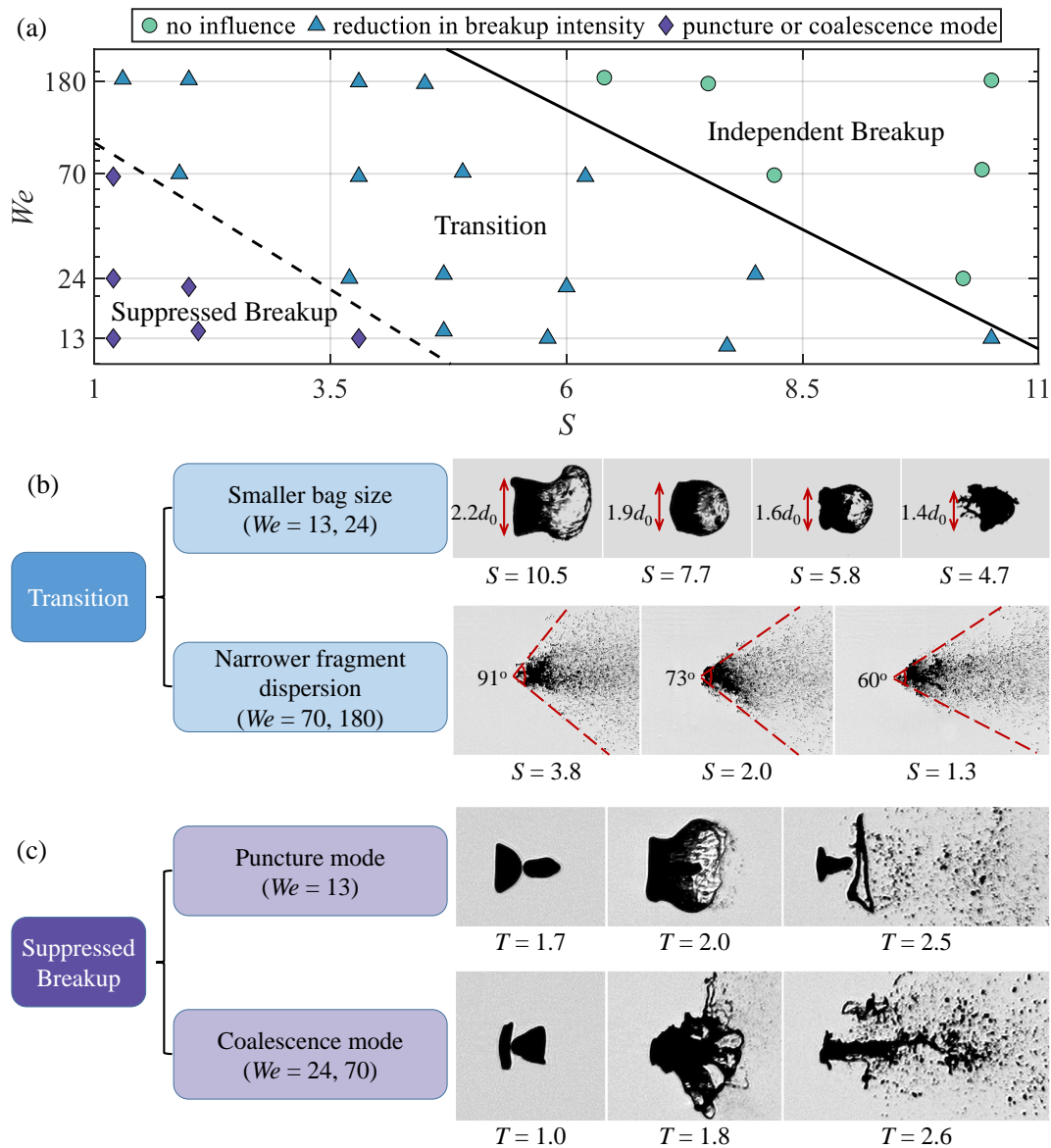


Figure 3.3: Change of the breakup pattern of the trailing droplet at different separation distances and Weber numbers, in comparison to the lead droplet (a). Exemplary cases in the transition region, characterized by smaller bag sizes at low Weber numbers and narrower fragment dispersion at high Weber numbers (b). Exemplary cases in the suppressed breakup region, exhibiting either puncture or coalescence mode (c).

3.3.2 Individual contributions of the candidate

This article [15] was published in the peer-reviewed journal *Physics of Fluids*. My contributions to this publication included conceiving the original idea, designing the experimental methodology and carrying out the experiments. I verified the experimental methods and analyzed the data by adapting post-processing tools. The original manuscript was written by me.

4 List of Publications

4.1 Peer-Reviewed Journal Articles

- **Wang, Z.**, Hopfes, T., Giglmaier, M. and Adams, N. A. "Experimental investigation of shock-induced tandem droplet breakup". In: *Physics of Fluids* 33 (2021), p. 012113.
- **Wang, Z.**, Hopfes, T., Giglmaier, M. and Adams, N. A. "Effect of Mach number on droplet aerobreakup in shear stripping regime". In: *Experiments in Fluids* 61.9 (2020), pp. 1-17.
- **Wang, Z.**, Giglmaier, M., Hopfes, T., Köglmeier, L. and Adams, N. A. "Impact of sensor housing geometries on transient stagnation pressure measurements in impulse facilities". In: *Experimental Thermal and Fluid Science* 109 (2019), p. 109851.

5 Discussion

This publication-based thesis was devoted to exploiting the well-defined flow conditions in a shock tube facility for studies of droplet breakup. Systematic pressure measurements have been carried out and verified the temporal steadiness and the spatial uniformity of the shock-induced freestream flow. Optimization of sensor housing designs that improved the measurement accuracy and the response rate was proposed in the first publication. By taking advantage of the high-speed freestream flow that was instantly accelerated by the shock wave, droplet breakup experiments have been conducted at high Mach numbers and in tandem formation. These two studies, which highlighted the importance of flow compressibility in supersonic atomization and detailed the droplet interaction in dense sprays, were summarized in the second and third publications, respectively.

Compared to conventional conical housings that are preferred for steady/quasi-steady pressure measurements [19, 91, 92], the present work demonstrated that blunt housings with short internal void showed noticeable advantages for transient pressure measurements in impulse facilities. The pressure signals measured by the embedded sensors exhibited shorter rise time, lower overshoot, weaker oscillations and shorter settling time, and were less influenced by misaligned assembly and inadequate shielding of the housing structure. Additionally, the borehole-cavity volume ratio in the void served as a general indicator for the housing interior design. The optimized sensor housing geometries were employed in the validation of the shock tube performance and also adopted in the droplet breakup studies to accurately measure the shock-induced freestream conditions.

The shock tube facility provided operating conditions over a wide range of Mach numbers. Owing to this advantage, the present work thoroughly compared droplet breakup in subsonic and supersonic flows. Previous literature related to high-speed breakup only managed to describe the early-stage deformation prior to the breakup. For instance, Ortiz et al. [99] reported a sharp rise in the droplet drag coefficient as the flow Mach number increased from 0.7 to 1.5. The numerical results from Xiao et al. [101] suggested a postponement of the breakup initiation for supersonic cases. Igra and Takayama [85] and Meng and Colonius [100] showed quantitatively that increasing the flow Mach number slowed the growth of the cross-stream diameter. Furthermore, in the above-mentioned research, the Mach number was varied with changing the Weber number. The present work, however, highlighted the individual role played by the flow Mach number in the entire breakup process. It is concluded that increasing the Mach number altered the stripping breakup pattern and favored the production of large fragments. The conventional stripping of the peripheral sheet in subsonic flow changed to rupture of multiple bags along the equator in transonic flow and further to fragmentation of ligaments over the leeward surface in supersonic flow. Meanwhile, the uniformity of

the fragment size distribution was disrupted and the cross-stream spread of the fragment dispersion was narrowed.

Another advantage of the shock tube facility was that the ambient flow field is instantly established by the fast-propagating incident shock wave. This rendered the present study of droplet breakup in tandem formation possible. The previous experimental research works about tandem droplet breakup covered very limited flow conditions and only drew qualitative conclusions. Zhao et al. [87] observed a puncture mode in bag breakup morphology, and Igra and Takayama [85] reported a lower deformation rate for the downstream water column in shear stripping morphology. Other numerical works [104–106] presented distinct patterns such as mushroom and shuttlecock shapes in the early-stage deformation but failed to model detailed breakup structures. In contrast to these preceding works, the present study analyzed tandem breakup patterns over a wide range of Weber numbers and separation distances and showed that the breakup of the trailing droplet was dampened or even completely suppressed by the presence of the neighboring lead droplet. With the separation distance falling below critical levels, the tandem formation reduced the size of bag structures of the trailing droplet at low Weber numbers and confined the dispersion of fragments at high Weber numbers. At even smaller separation distances, the trailing droplet failed to follow the conventional breakup morphology but exhibited either puncture or coalescence modes.

6 Outlook

The research topics covered in the thesis are of significance in a variety of practical applications, but have not been systematically investigated in previous literature. Main difficulties lie in the development of reliable experimental setup to repeat the desired physical scenario. Nevertheless, the experimental designs illustrated in this thesis can be further exploited or optimized to extend the present work. Potential topics for future research are listed as follows:

- The measurement of static pressure in impulse facilities is equally crucial to the measurement of stagnation pressure. We have noticed from previous shock tube experiments that the measurement accuracy is highly sensitive to the precision of the flush mounting of sensors. Furthermore, this sensitivity seems to depend on flow conditions and exhibits opposite trends in subsonic and supersonic flows. Therefore, the effect of the sensor misalignment on the measurement of static pressure needs to be addressed and associated techniques to tackle this problem is desired.
- The current work presents the influence of flow Mach number on the droplet breakup only in the shear stripping morphology. However, in practical applications droplets tend to complete the breakup process in the regime of bag breakup. The bag breakup is dominated by Rayleigh-Taylor instabilities instead of Kelvin-Helmholtz instabilities that drive the shear stripping breakup. Consequently, how the supersonic flow would transform the conventional bag breakup remains to be explored. Another topic of interest related to the supersonic atomization is based on the fact that the detached bow shock in front of the droplet lowers the effective Weber number. By delicately designing experimental conditions, the freestream flow and the post-bow shock flow could yield distinct Weber numbers that correspond to different breakup morphologies. Detailed study of droplet behavior under such situations would expand our understanding of breakup phenomena.
- The tandem formation investigated in the present work is the simplest arrangement of multiple droplets. In reality droplets tend to be distributed closely in more complex patterns and in larger numbers. First, the interaction of two droplets spaced in the cross-stream direction needs to be resolved. Although the shielding effect is absent for this arrangement, the flow field around individual droplets becomes asymmetric which is expected to make a difference to the breakup structures. Second, the breakup of a large cluster of closely-packed droplets is worth being studied. By comparing the average breakup intensity of the droplet cluster to the single droplet breakup, general guidance on the modeling of dense sprays would be obtained.

Bibliography

- [1] Bleakney, W., Weimer, D., and Fletcher, C. "The shock tube: a facility for investigations in fluid dynamics". In: *Review of Scientific Instruments* 20.11 (1949), pp. 807–815.
- [2] Glass, I. and Patterson, G. "A theoretical and experimental study of shock-tube flows". In: *Journal of the Aeronautical Sciences* 22.2 (1955), pp. 73–100.
- [3] Chang, T. and Hsiao, L. "The Riemann problem and interaction of waves in gas dynamics". In: *NASA STI/Recon Technical Report A 90* (1989), p. 44044.
- [4] Mark, H. *The interaction of a reflected shock wave with the boundary layer in a shock tube*. National Advisory Committee for Aeronautics, 1958.
- [5] Miller, J. A., Mitchell, R. E., Smooke, M. D., and Kee, R. J. "Toward a comprehensive chemical kinetic mechanism for the oxidation of acetylene: comparison of model predictions with results from flame and shock tube experiments". In: *Symposium (International) on Combustion*. Vol. 19. 1. Elsevier. 1982, pp. 181–196.
- [6] Anderson, J. D. *Modern compressible flow*. Tata McGraw-Hill Education, 2003.
- [7] Curran, H. J., Dunphy, M. P., Simmie, J. M., Westbrook, C. K., and Pitz, W. J. "Shock tube ignition of ethanol, isobutene and MTBE: Experiments and modeling". In: *Symposium (international) on Combustion*. Vol. 24. 1. Elsevier. 1992, pp. 769–776.
- [8] Alexiou, A. and Williams, A. "Soot formation in shock-tube pyrolysis of toluene, toluene-methanol, toluene-ethanol, and toluene-oxygen mixtures". In: *Combustion and flame* 104.1-2 (1996), pp. 51–65.
- [9] Arakeri, J., Das, D., Krothapalli, A., and Lourenco, L. "Vortex ring formation at the open end of a shock tube: A particle image velocimetry study". In: *Physics of fluids* 16.4 (2004), pp. 1008–1019.
- [10] Hornung, H., Sturtevant, B., Belanger, J., Sanderson, S., Brouillette, M., and Jenkins, M. "Performance data of the new free-piston shock tunnel T5 at GALCIT". In: *Shock Waves*. Springer, 1992, pp. 603–610.
- [11] Tranter, R., Brezinsky, K., and Fulle, D. "Design of a high-pressure single pulse shock tube for chemical kinetic investigations". In: *Review of Scientific Instruments* 72.7 (2001), pp. 3046–3054.
- [12] Tranter, R., Sivaramakrishnan, R., Srinivasan, N., and Brezinsky, K. "Calibration of reaction temperatures in a very high pressure shock tube using chemical thermometers". In: *International Journal of Chemical Kinetics* 33.11 (2001), pp. 722–731.

- [13] Meshkov, E. "Instability of the interface of two gases accelerated by a shock wave". In: *Fluid Dynamics* 4.5 (1969), pp. 101–104.
- [14] Wang, Z., Hopfes, T., Giglmaier, M., and Adams, N. A. "Effect of Mach number on droplet aerobreakup in shear stripping regime". In: *Experiments in Fluids* 61.9 (2020), pp. 1–17.
- [15] Wang, Z., Hopfes, T., Giglmaier, M., and Adams, N. A. "Experimental investigation of shock-induced tandem droplet breakup". In: *Physics of Fluids* 33 (2021), p. 012113.
- [16] Cable, A. and Cox, R. "The Ludwig pressure-tube supersonic wind tunnel". In: *The Aeronautical Quarterly* 14.2 (1963), pp. 143–157.
- [17] Klopfenstein Jr, R. "Air velocity and flow measurement using a Pitot tube". In: *ISA transactions* 37.4 (1998), pp. 257–263.
- [18] Folsom, R. G. *Review of the Pitot tube*. Tech. rep. 1955.
- [19] Chue, S. "Pressure probes for fluid measurement". In: *Progress in aerospace sciences* 16.2 (1975), pp. 147–223.
- [20] Gossweiler, C. "On probes and measuring techniques for fast-response flow measurement using piezo-resistive pressure transducers." In: (1995).
- [21] Lec, R. M. "Piezoelectric biosensors: recent advances and applications". In: *Proceedings of the 2001 IEEE International Frequency Control Symposium and PDA Exhibition (Cat. No. 01CH37218)*. IEEE. 2001, pp. 419–429.
- [22] Gautschi, G. "Piezoelectric sensors". In: *Piezoelectric Sensorics*. Springer, 2002, pp. 73–91.
- [23] Neely, A., Stalker, R., and Paull, A. "High enthalpy, hypervelocity flows of air and argon in an expansion tube". In: *The Aeronautical Journal* 95.946 (1991), pp. 175–186.
- [24] Paull, A. and Stalker, R. "Test flow disturbances in an expansion tube". In: *Journal of Fluid Mechanics* 245 (1992), pp. 493–521.
- [25] Sasoh, A., Ohnishi, Y., Ramjaun, D., Takayama, K., Otsu, H., and Abe, T. "Effective test time evaluation in high-enthalpy expansion tube". In: *AIAA journal* 39.11 (2001), pp. 2141–2147.
- [26] Sutcliffe, M. and Morgan, R. "The measurement of Pitot pressure in high enthalpy expansion tubes". In: *Measurement Science and Technology* 12.3 (2001), p. 327.
- [27] Davies, L. "Bow-shock establishment and stagnation-point pressure measurements for a blunt-nosed body at supersonic speeds". In: (1965).
- [28] Reitz, R. D. and Diwakar, R. "Effect of drop breakup on fuel sprays". In: *SAE transactions* (1986), pp. 218–227.
- [29] Reitz, R. D. and Diwakar, R. "Structure of high-pressure fuel sprays". In: *SAE transactions* (1987), pp. 492–509.
- [30] Kamimoto, T. and Kobayashi, H. "Combustion processes in diesel engines". In: *Progress in Energy and Combustion Science* 17.2 (1991), pp. 163–189.
- [31] Liu, A. B., Mather, D., and Reitz, R. D. "Modeling the effects of drop drag and breakup on fuel sprays". In: *SAE Transactions* (1993), pp. 83–95.

- [32] Arcoumanis, C., Gavaises, M., and French, B. "Effect of fuel injection processes on the structure of diesel sprays". In: *SAE transactions* (1997), pp. 1025–1064.
- [33] Heimann, R. B. "Plasma-spray coating". In: *Principles and Applications* (1996), p. 2.
- [34] Mostaghimi, J., Pasandideh-Fard, M., and Chandra, S. "Dynamics of splat formation in plasma spray coating process". In: *Plasma Chemistry and Plasma Processing* 22.1 (2002), pp. 59–84.
- [35] Pasandideh-Fard, M., Pershin, V., Chandra, S., and Mostaghimi, J. "Splat shapes in a thermal spray coating process: simulations and experiments". In: *Journal of Thermal Spray Technology* 11.2 (2002), pp. 206–217.
- [36] Moridi, A., Hassani-Gangaraj, S. M., Guagliano, M., and Dao, M. "Cold spray coating: review of material systems and future perspectives". In: *Surface Engineering* 30.6 (2014), pp. 369–395.
- [37] Grant, P. "Spray forming". In: *Progress in Materials science* 39.4-5 (1995), pp. 497–545.
- [38] Leatham, A. "Spray forming: alloys, products and markets". In: *Metal Powder Report* 54.5 (1999), pp. 28–37.
- [39] Lagutkin, S., Achelis, L., Sheikhaliev, S., Uhlenwinkel, V., and Srivastava, V. "Atomization process for metal powder". In: *Materials Science and Engineering: A* 383.1 (2004), pp. 1–6.
- [40] Henein, H., Uhlenwinkel, V., and Fritsching, U. *Metal sprays and spray deposition*. Springer, 2017.
- [41] Mates, S. P. and Settles, G. S. "A study of liquid metal atomization using close-coupled nozzles, Part 1: Gas dynamic behavior". In: *Atomization and Sprays* 15.1 (2005).
- [42] Zeoli, N. and Gu, S. "Numerical modelling of droplet break-up for gas atomisation". In: *Computational Materials Science* 38.2 (2006), pp. 282–292.
- [43] Watanawanyoo, P., Hirahara, H., Mochida, H., Furukawa, T., Nakamura, M., and Chaitap, S. "Experimental investigations on spray characteristics in twin-fluid atomizer". In: *Procedia Engineering* 24 (2011), pp. 866–872.
- [44] Firmansyah, D. A., Kaiser, R., Zahaf, R., Coker, Z., Choi, T.-Y., and Lee, D. "Numerical simulations of supersonic gas atomization of liquid metal droplets". In: *Japanese Journal of Applied Physics* 53.5S3 (2014), 05HA09.
- [45] Hsiang, L.-P. and Faeth, G. "Drop deformation and breakup due to shock wave and steady disturbances". In: *International Journal of Multiphase Flow* 21.4 (1995), pp. 545–560.
- [46] Lane, W. "Shatter of drops in streams of air". In: *Industrial & Engineering Chemistry* 43.6 (1951), pp. 1312–1317.
- [47] Hinze, J. "Fundamentals of the hydrodynamic mechanism of splitting in dispersion processes". In: *AIChE journal* 1.3 (1955), pp. 289–295.
- [48] Pilch, M. and Erdman, C. "Use of breakup time data and velocity history data to predict the maximum size of stable fragments for acceleration-induced breakup of a liquid drop". In: *International journal of multiphase flow* 13.6 (1987), pp. 741–757.

- [49] Faeth, G., Hsiang, L.-P., and Wu, P.-K. "Structure and breakup properties of sprays". In: *International Journal of Multiphase Flow* 21 (1995), pp. 99–127.
- [50] GuILDENBECHER, D., LÓPEZ-RIVERA, C., and SOJKA, P. "Secondary atomization". In: *Experiments in Fluids* 46.3 (2009), p. 371.
- [51] GORDON, G. "Mechanism and speed of breakup of drops". In: *Journal of Applied Physics* 30.11 (1959), pp. 1759–1761.
- [52] WIERZBA, A. "Deformation and breakup of liquid drops in a gas stream at nearly critical Weber numbers". In: *Experiments in fluids* 9.1 (1990), pp. 59–64.
- [53] KRZECZKOWSKI, S. A. "Measurement of liquid droplet disintegration mechanisms". In: *International Journal of Multiphase Flow* 6.3 (1980), pp. 227–239.
- [54] DAI, Z. and FAETH, G. "Temporal properties of secondary drop breakup in the multimode breakup regime". In: *International Journal of Multiphase Flow* 27.2 (2001), pp. 217–236.
- [55] CHOU, W.-H. and FAETH, G. "Temporal properties of secondary drop breakup in the bag breakup regime". In: *International journal of multiphase flow* 24.6 (1998), pp. 889–912.
- [56] JOSEPH, D. D., BELANGER, J., and BEAVERS, G. "Breakup of a liquid drop suddenly exposed to a high-speed airstream". In: *International Journal of Multiphase Flow* 25.6-7 (1999), pp. 1263–1303.
- [57] JOSEPH, D., BEAVERS, G., and FUNADA, T. "Rayleigh-Taylor instability of viscoelastic drops at high Weber numbers". In: *Journal of Fluid Mechanics* 453 (2002), pp. 109–132.
- [58] THEOFANOUS, T., LI, G., and DINH, T.-N. "Aerobreakup in rarefied supersonic gas flows". In: *J. Fluids Eng.* 126.4 (2004), pp. 516–527.
- [59] ZHAO, H., LIU, H.-F., LI, W.-F., and XU, J.-L. "Morphological classification of low viscosity drop bag breakup in a continuous air jet stream". In: *Physics of Fluids* 22.11 (2010), p. 114103.
- [60] HAN, J. and TRYGGVASON, G. "Secondary breakup of axisymmetric liquid drops. I. Acceleration by a constant body force". In: *Physics of fluids* 11.12 (1999), pp. 3650–3667.
- [61] HAN, J. and TRYGGVASON, G. "Secondary breakup of axisymmetric liquid drops. II. Impulsive acceleration". In: *Physics of fluids* 13.6 (2001), pp. 1554–1565.
- [62] OPFER, L., ROISMAN, I., VENZMER, J., KLOSTERMANN, M., and TROPEA, C. "Droplet-air collision dynamics: Evolution of the film thickness". In: *Physical Review E* 89.1 (2014), p. 013023.
- [63] VILLERMAUX, E. and BOSSA, B. "Single-drop fragmentation determines size distribution of raindrops". In: *Nature Physics* 5.9 (2009), pp. 697–702.
- [64] INAMURA, T., YANAOKA, H., and KAWADA, T. "Visualization of airflow around a single droplet deformed in an airstream". In: *Atomization and Sprays* 19.7 (2009).
- [65] HSIANG, L.-P. and FAETH, G. M. "Near-limit drop deformation and secondary breakup". In: *International journal of multiphase flow* 18.5 (1992), pp. 635–652.
- [66] NICHOLLS, J. and RANGER, A. "Aerodynamic shattering of liquid drops." In: *Aiaa Journal* 7.2 (1969), pp. 285–290.

- [67] Chou, W.-H., Hsiang, L.-P., and Faeth, G. "Temporal properties of drop breakup in the shear breakup regime". In: *International Journal of Multiphase Flow* 23.4 (1997), pp. 651–669.
- [68] Igra, D. and Takayama, K. "Investigation of aerodynamic breakup of a cylindrical water droplet". In: *Atomization and Sprays* 11.2 (2001).
- [69] Igra, D., Ogawa, T., and Takayama, K. "A parametric study of water column deformation resulting from shock wave loading". In: *Atomization and Sprays* 12.5&6 (2002).
- [70] Liu, Z. and Reitz, R. "An analysis of the distortion and breakup mechanisms of high speed liquid drops". In: *International journal of multiphase flow* 23.4 (1997), pp. 631–650.
- [71] Lee, C. and Reitz, R. D. "Modeling the effects of gas density on the drop trajectory and breakup size of high-speed liquid drops". In: *Atomization and Sprays* 9.5 (1999).
- [72] Lee, C. and Reitz, R. D. "An experimental study of the effect of gas density on the distortion and breakup mechanism of drops in high speed gas stream". In: *International Journal of Multiphase Flow* 26.2 (2000), pp. 229–244.
- [73] Lee, C. S. and Reitz, R. D. "Effect of liquid properties on the breakup mechanism of high-speed liquid drops". In: *Atomization and Sprays* 11.1 (2001).
- [74] Khosla, S., Smith, C. E., and Throckmorton, R. P. "Detailed understanding of drop atomization by gas crossflow using the volume of fluid method". In: *19th Annual Conference on Liquid Atomization and Spray Systems (ILASS-Americas), Toronto, Canada. 2006.*
- [75] Wadhwa, A. R., Magi, V., and Abraham, J. "Transient deformation and drag of decelerating drops in axisymmetric flows". In: *Physics of Fluids* 19.11 (2007), p. 113301.
- [76] Theofanous, T. and Li, G. "On the physics of aerobreakup". In: *Physics of fluids* 20.5 (2008), p. 052103.
- [77] Schmehl, R. "Modeling droplet breakup in complex two-phase flows". In: *9th International Conference on Liquid Atomization and Spray Systems ICLASS, 13-17 July 2003, Sorrento, Italy. 2003.*
- [78] Jain, M., Prakash, R. S., Tomar, G., and Ravikrishna, R. "Secondary breakup of a drop at moderate Weber numbers". In: *Proceedings of the Royal Society A: Mathematical, Physical and Engineering Sciences* 471.2177 (2015), p. 20140930.
- [79] Reinecke, W. and McKay, W. *EXPERIMENTS ON WATER DROP BREAKUP BEHIND MACH 3 TO 12 SHOCKS*. Tech. rep. Avco Corp., Wilmington, Mass. Avco Government Products Group, 1969.
- [80] Reinecke, W. and Waldman, G. *A study of drop breakup behind strong shocks with applications to flight*. Tech. rep. AVCO SYSTEMS DIV WILMINGTON MA, 1970.
- [81] Hwang, S., Liu, Z., and Reitz, R. D. "Breakup mechanisms and drag coefficients of high-speed vaporizing liquid drops". In: *Atomization and Sprays* 6.3 (1996).
- [82] Kékesi, T., Amberg, G., and Wittberg, L. P. "Drop deformation and breakup". In: *International Journal of Multiphase Flow* 66 (2014), pp. 1–10.

- [83] Aalburg, C., Van Leer, B., and Faeth, G. "Deformation and drag properties of round drops subjected to shock-wave disturbances". In: *AIAA journal* 41.12 (2003), pp. 2371–2378.
- [84] Aalburg, C., Leer, B. van, Faeth, G. M., and Sallam, K. A. "Properties of non-turbulent round liquid jets in uniform gaseous cross flows". In: *Atomization and Sprays* 15.3 (2005).
- [85] Igra, D. and Takayama, K. "Experimental investigation of two cylindrical water columns subjected to planar shock wave loading". In: *J. Fluids Eng.* 125.2 (2003), pp. 325–331.
- [86] Theofanous, T., Mitkin, V., Ng, C., Chang, C., Deng, X., and Sushchikh, S. "The physics of aerobreakup. II. Viscous liquids". In: *Physics of Fluids* 24.2 (2012), p. 022104.
- [87] Zhao, H., Wu, Z., Li, W., Xu, J., and Liu, H. "Interaction of two drops in the bag breakup regime by a continuous air jet". In: *Fuel* 236 (2019), pp. 843–850.
- [88] Merrington, A. and Richardson, E. "The break-up of liquid jets". In: *Proceedings of the Physical Society* 59.1 (1947), p. 1.
- [89] Magarvey, R. and Taylor, B. "Free fall breakup of large drops". In: *Journal of Applied Physics* 27.10 (1956), pp. 1129–1135.
- [90] Gel'Fand, B., Gubin, S., Kogarko, S., and Komar, S. "Singularities of the breakup of viscous liquid droplets in shock waves". In: *Journal of engineering physics* 25.3 (1973), pp. 1140–1142.
- [91] Naughton, J., Cattafesta III, L., and Settles, G. "Miniature, fast-response five-hole conical probe for supersonic flowfield measurements". In: *AIAA journal* 31.3 (1993), pp. 453–458.
- [92] Porro, A. R. "Pressure probe designs for dynamic pressure measurements in a supersonic flow field". In: *ICIASF 2001 Record, 19th International Congress on Instrumentation in Aerospace Simulation Facilities (Cat. No. 01CH37215)*. IEEE. 2001, pp. 417–426.
- [93] Wang, Z., Giglmaier, M., Hopfes, T., Köglmeier, L., and Adams, N. A. "Impact of sensor housing geometries on transient stagnation pressure measurements in impulse facilities". In: *Experimental Thermal and Fluid Science* 109 (2019), p. 109851.
- [94] Nagata, T., Nonomura, T., Takahashi, S., Mizuno, Y., and Fukuda, K. "Investigation on subsonic to supersonic flow around a sphere at low Reynolds number of between 50 and 300 by direct numerical simulation". In: *Physics of fluids* 28.5 (2016), p. 056101.
- [95] Kailasanath, K. "Recent developments in the research on pulse detonation engines". In: *AIAA journal* 41.2 (2003), pp. 145–159.
- [96] Curran, E. T. "Scramjet engines: the first forty years". In: *Journal of Propulsion and Power* 17.6 (2001), pp. 1138–1148.
- [97] Anderson, I., Figliola, R., and Morton, H. "Flow mechanisms in high pressure gas atomization". In: *Materials Science and Engineering: A* 148.1 (1991), pp. 101–114.

- [98] Dinh, N., Li, G., and Theofanous, T. "An investigation of droplet breakup in a high Mach, low Weber number regime". In: *41st Aerospace Sciences Meeting and Exhibit*. 2003, p. 317.
- [99] Ortiz, C., Joseph, D., and Beavers, G. "Acceleration of a liquid drop suddenly exposed to a high-speed airstream". In: *International journal of multiphase flow* 30.2 (2004), pp. 217–224.
- [100] Meng, J. and Colonius, T. "Numerical simulations of the early stages of high-speed droplet breakup". In: *Shock Waves* 25.4 (2015), pp. 399–414.
- [101] Xiao, F., Wang, Z., Sun, M., Liu, N., and Yang, X. "Simulation of drop deformation and breakup in supersonic flow". In: *Proceedings of the Combustion Institute* 36.2 (2017), pp. 2417–2424.
- [102] Ashgriz, N. *Handbook of atomization and sprays: theory and applications*. Springer Science & Business Media, 2011.
- [103] Dorr, G. J., Hewitt, A. J., Adkins, S. W., Hanan, J., Zhang, H., and Noller, B. "A comparison of initial spray characteristics produced by agricultural nozzles". In: *Crop Protection* 53 (2013), pp. 109–117.
- [104] Quan, S., Lou, J., and Stone, H. A. "Interactions between two deformable droplets in tandem subjected to impulsive acceleration by surrounding flows". In: *Journal of fluid mechanics* 684 (2011), p. 384.
- [105] Kékesi, T., Altimira, M., Amberg, G., and Wittberg, L. P. "Interaction between two deforming liquid drops in tandem and various off-axis arrangements subject to uniform flow". In: *International Journal of Multiphase Flow* 112 (2019), pp. 193–218.
- [106] Stefanitsis, D., Malgarinos, I., Strotos, G., Nikolopoulos, N., Kakaras, E., and Gavaises, M. "Numerical investigation of the aerodynamic breakup of droplets in tandem". In: *International Journal of Multiphase Flow* 113 (2019), pp. 289–303.
- [107] Guderley, K. "Starke kugelige und zylindrische verdichtungsstosse in der nahe des kugelmittelpunktes bzw. der zylinderachse". In: *Luftfahrtforschung* 19 (1942), p. 302.
- [108] Kim, J., Kwon Lee, J., and Mu Lee, K. "Accurate image super-resolution using very deep convolutional networks". In: *Proceedings of the IEEE conference on computer vision and pattern recognition*. 2016, pp. 1646–1654.
- [109] Charters, A. C. and Thomas, R. N. "The aerodynamic performance of small spheres from subsonic to high supersonic velocities". In: *Journal of the Aeronautical sciences* 12.4 (1945), pp. 468–476.
- [110] Bailey, A. and Hiatt, J. "Sphere drag coefficients for a broad range of Mach and Reynolds numbers". In: *Aiaa Journal* 10.11 (1972), pp. 1436–1440.
- [111] Hanson, A., Domich, E., and Adams, H. "Shock tube investigation of the breakup of drops by air blasts". In: *The Physics of Fluids* 6.8 (1963), pp. 1070–1080.
- [112] Karyagin, V., Lopatkin, A., Shvets, A., and Shilin, N. "Experimental investigation of the separation of flow around a sphere". In: *Fluid dynamics* 26.1 (1991), pp. 126–129.

-
- [113] Jalaal, M. and Mehravaran, K. "Transient growth of droplet instabilities in a stream". In: *Physics of Fluids* 26.1 (2014), p. 012101.
 - [114] Nayfeh, A. H. and Saric, W. S. "Non-linear kelvin–helmholtz instability". In: *Journal of Fluid Mechanics* 46.2 (1971), pp. 209–231.
 - [115] Papamoschou, D. and Roshko, A. "The compressible turbulent shear layer: an experimental study". In: *Journal of fluid Mechanics* 197 (1988), pp. 453–477.
 - [116] Liepmann, H. W. and Roshko, A. *Elements of gasdynamics*. Courier Corporation, 2001.
 - [117] Shinjo, J. and Umemura, A. "Simulation of liquid jet primary breakup: Dynamics of ligament and droplet formation". In: *International Journal of Multiphase Flow* 36.7 (2010), pp. 513–532.
 - [118] Samuelsen, G. and Stapper, B. "An experimental study of the breakup of a two-dimensional liquid sheet in the presence of co-flow air shear". In: *aiaa* (1990).

A Original Peer-Reviewed Publications

The three peer-reviewed journal articles presented in this thesis are attached here.

A.1 Impact of Sensor Housing Geometries on Transient Stagnation Pressure Measurements in Impulse Facilities

Zhaoguang Wang, Marcus Giglmaier, Thomas Hopfes, Lea Köglmeier, Nikolaus A. Adams

In: *Experimental Thermal and Fluid Science* 109 (2019), p.109851.
<https://doi.org/10.1016/j.expthermflusci.2019.109851>.

Contribution: My contributions to this publication included carrying out experiments and performing numerical simulations. I verified the experimental and numerical methods, and analyzed the data by adapting post-processing tools. The original manuscript was written by me.

JOURNAL PUBLISHING AND LICENSING AGREEMENT

Elsevier Inc.

Article: Impact of sensor housing geometries on transient stagnation pressure measurements in impulse facilities
Corresponding author: Mr. Zhaoguang Wang
E-mail address: zg.wang@tum.de
Journal: Experimental Thermal and Fluid Science
Article number: 109851
Our reference: ETF_109851
PII: S0894177719301591
DOI: 10.1016/j.expthermflusci.2019.109851

YOUR STATUS

» I am one author signing on behalf of all co-authors of the manuscript

LICENSE OF PUBLISHING RIGHTS

I hereby grant to Elsevier Inc. an exclusive publishing and distribution license in the manuscript identified above and any tables, illustrations or other material submitted for publication as part of the manuscript (the "Article") in print, electronic and all other media (whether now known or later developed), in any form, in all languages, throughout the world, for the full term of copyright, and the right to license others to do the same, effective when the Article is accepted for publication. This license includes the right to enforce the rights granted hereunder against third parties.

SUPPLEMENTAL MATERIALS

"Supplemental Materials" shall mean materials published as a supplemental part of the Article, including but not limited to graphical, illustrative, video and audio material.

With respect to any Supplemental Materials that I submit, Elsevier Inc. shall have a perpetual worldwide non-exclusive right and license to publish, extract, reformat, adapt, build upon, index, redistribute, link to and otherwise use all or any part of the Supplemental Materials, in all forms and media (whether now known or later developed) and permit others to do so. The publisher shall apply the same end user license to the Supplemental Materials as to the Article where it publishes the Supplemental Materials with the Article in the journal on its online platforms on an Open Access basis.

RESEARCH DATA

"Research Data" shall mean the result of observations or experimentation that validate research findings and that are published separate to the Article, which can include but are not limited to raw data, processed data, software, algorithms, protocols, and methods.

With respect to any Research Data that I wish to make accessible on a site or through a service of Elsevier Inc., Elsevier Inc. shall have a perpetual worldwide, non-exclusive right and license to publish, extract, reformat, adapt, build upon, index, redistribute, link to and otherwise use all or any part of the Research Data in all forms and media (whether now known or later developed), and to permit others to do so. Where I have selected a specific end user license under which the Research Data is to be made available on a site or through a service, the publisher shall apply that end user license to the Research Data on that site or service.

SCHOLARLY COMMUNICATION RIGHTS

I understand that I retain the copyright in the Article and that no rights in patents, trademarks or other intellectual property rights are transferred to Elsevier Inc.. As the author of the Article, I understand that I shall have: (i) the same rights to reuse the Article as those allowed to third party users of the Article under the CC BY-NC-ND License, as well as (ii) the right to use the Article in a subsequent compilation of my works or to extend the Article to book length form, to include the Article in a thesis or dissertation, or otherwise to use or re-use portions or excerpts in other works, for both commercial and non-commercial purposes. Except for such uses, I understand that the license of publishing rights I have granted to Elsevier Inc. gives Elsevier Inc. the exclusive right to make or sub-license commercial use.

USER RIGHTS

The publisher will apply the *Creative Commons Attribution-Noncommercial-NoDerivative Works 4.0 International License* (CC BY-NC-ND) to the Article where it publishes the Article in the journal on its online platforms on an Open Access basis. For further information, see <http://www.elsevier.com/about/open-access/open-access-options>.

The CC BY-NC-ND license allows users to copy and distribute the Article, provided this is not done for commercial purposes and further does not permit distribution of the Article if it is changed or edited in any way, and provided the user gives appropriate credit (with a link to the formal publication through the relevant DOI), provides a link to the license, and that the licensor is not represented as endorsing the use made of the work. The full details of the license are available at <http://creativecommons.org/licenses/by-nc-nd/4.0>.

REVERSION OF RIGHTS

Articles may sometimes be accepted for publication but later rejected in the publication process, even in some cases after public posting in "Articles in Press" form, in which case all rights will revert to the author. See <https://www.elsevier.com/about/our-business/policies/article-withdrawal>.

REVISIONS AND ADDENDA

I understand that no revisions, additional terms or addenda to this License Agreement can be accepted without Elsevier Inc.'s express written consent. I understand that this License Agreement supersedes any previous agreements I have entered into with Elsevier Inc. in relation to the Article from the date hereof.

COPYRIGHT NOTICE

The publisher shall publish and distribute the Article with the appropriate copyright notice.

AUTHOR REPRESENTATIONS / ETHICS AND DISCLOSURE / SANCTIONS

I affirm the Author Representations noted below, and confirm that I have reviewed and complied with the relevant Instructions to Authors, Ethics in Publishing policy, Declarations of Interest disclosure and information for authors from countries affected by sanctions (Iran, Cuba, Sudan, Burma, Syria, or Crimea). Please note that some journals may require that all co-authors sign and submit Declarations of Interest disclosure forms. I am also aware of the publisher's policies with respect to retractions and withdrawal (<https://www.elsevier.com/about/our-business/policies/article-withdrawal>).

For further information see the publishing ethics page at <https://www.elsevier.com/about/our-business/policies/publishing-ethics> and the journal home page. For further information on sanctions, see <https://www.elsevier.com/about/our-business/policies/trade-sanctions>

Author representations

- » The Article I have submitted to the journal for review is original, has been written by the stated authors and has not been previously published.
- » The Article was not submitted for review to another journal while under review by this journal and will not be submitted to any other journal.
- » The Article and the Supplemental Materials do not infringe any copyright, violate any other intellectual property, privacy or other right, or contain any libellous or other unlawful matter.
- » I have obtained written permission from copyright owners for any excerpts from copyrighted works that are included and have created the Article or the Supplemental Materials.
- » Except as expressly set out in this License Agreement, the Article is not subject to any prior rights or licenses and, if my or any of my co-authors' institutions has a policy that might restrict my ability to grant the rights required by this License Agreement (taking into account the communication rights permitted hereunder), a written waiver of that policy has been obtained.
- » If I and/or any of my co-authors reside in Iran, Cuba, Sudan, Burma, Syria, or Crimea, the Article has been prepared in a personal capacity and not as an official representative or otherwise on behalf of the relevant government or institution.
- » If I am using any personal details or images of patients, research subjects or other individuals, I have obtained all consents required and complied with the publisher's policies relating to the use of such images or personal information. See <https://www.elsevier.com/about/our-business/policies/patient-consent> for further information.
- » Any software contained in the Supplemental Materials is free from viruses, contaminants or worms.
- » If the Article or any of the Supplemental Materials were prepared jointly with other authors, I have informed the co-author(s) of this License Agreement and that I am signing on their behalf as their agent, and I am authorized to do so.

GOVERNING LAW AND JURISDICTION

This License Agreement will be governed by and construed in accordance with the laws of the country or state of Elsevier Inc. ("the Governing State"), without regard to conflict of law principles, and the parties irrevocably consent to the exclusive jurisdiction of the courts of the Governing State.

For information on the publisher's copyright and access policies, please see <http://www.elsevier.com/copyright>.

I have read and agree to the terms of the License Agreement.

6th July 2019

T-copyright license-v5/2017



Impact of sensor housing geometries on transient stagnation pressure measurements in impulse facilities

Zhaoguang Wang*, Marcus Giglmaier, Thomas Hopfes, Lea Köglmeier, Nikolaus A. Adams

Institute of Aerodynamics and Fluid Mechanics, Technical University of Munich, 85748 Garching, Germany

ABSTRACT

The measurement of transient stagnation pressure in impulse facilities, such as shock tubes and expansion tubes, is critical due to the limited experimental time window. In the present study, we investigate the characteristic behavior of pressure sensors shielded by blunt and conical housings, and evaluate the specific influence of the housing dimensions on the stagnation pressure measurement in distinct flow conditions. Pressure signals of piezoelectric sensors were acquired and schlieren images visualizing the wave dynamics were recorded. We conducted additional numerical simulations to support our hypotheses concerning the flow inside the housings. Results indicate that the pressure signal for conical housings exhibits longer rise time and more pronounced oscillations compared to that for blunt housings. Enlarging the borehole diameter and reducing the cavity depth both shorten signal rise time but enhance overshoots. Additional experiments on the sensitivity to assembly misalignment, the effect of gelatin-filled housings and the performance of exposed sensors complete the study.

1. Introduction

Pitot tubes have been widely adopted for total pressure measurements due to the low cost and the simplicity of operation. The measured pitot pressure is normally used to derive the flow velocity or the volumetric flow rate in steady/quasi-steady flows [1,2].

For subsonic flows, the Pitot tube directly measures the flow total pressure $p_{0\infty}$ with the presumption of isentropic deceleration, where

$$p_{0\infty} = p_{\infty} \left(1 + \frac{\kappa - 1}{2} M_{\infty}^2 \right)^{\frac{\kappa}{\kappa - 1}} \quad (1)$$

with p_{∞} , M_{∞} and κ being the freestream static pressure, the Mach number and the heat capacity ratio, respectively. However, more complexities are added when the flow reaches supersonic conditions. The deceleration of supersonic flows to stagnation conditions typically involves the formation of shocks [3] and hence, total pressure losses. To take them into account, the center of the detached bow shock ahead of the Pitot tube is assumed to fulfill the normal shock relations. Then, the static pressure ratio across the shock \bar{p}/p_{∞} and the post-shock Mach number \bar{M} are solely dependent on the pre-shock Mach number M_{∞} and the gas heat capacity ratio κ [4]:

$$\bar{p} = p_{\infty} \left(1 + \frac{2\kappa}{\kappa + 1} (M_{\infty}^2 - 1) \right) \quad (2)$$

$$\bar{M}^2 = \left(1 + \frac{\kappa - 1}{2} M_{\infty}^2 \right) \left(\kappa M_{\infty}^2 - \frac{\kappa - 1}{2} \right)^{-1} \quad (3)$$

By assuming that there is again an isentropic flow behind the shock,

both the pre- and the post-shock quantities satisfy Eq. (1) individually. Hence, the Pitot tube measures the post-shock stagnation pressure \bar{p}_0 , and the stagnation pressure $p_{0\infty}$ of the pre-shock undisturbed flow is deduced as:

$$p_{0\infty} = \bar{p}_0 \cdot \left(\frac{2\kappa M_{\infty}^2 - (\kappa - 1)}{\kappa + 1} \right)^{\frac{1}{\kappa - 1}} \left(\frac{(\kappa - 1) + 2/M_{\infty}^2}{\kappa + 1} \right)^{\frac{\kappa}{\kappa - 1}} \quad (4)$$

Folsom [5] and Chue [6] provided comprehensive reviews of the Pitot tube technique, and summarized various tube designs and calibration methods. However, the response rate of conventional Pitot tubes is too low for the transient pressure measurement in impulse facilities.

In shock tubes or expansion tubes where the experimental time tends to be extremely short, piezoelectric or piezoresistive pressure sensors are preferred due to their short response time and high resonant frequency paired with the high sensitivity to even small pressure fluctuations [7–9]. These sensors are positioned towards the freestream, creating a stagnation area at the tip and measuring the flow stagnation pressure on the same principle as conventional Pitot tubes. Housings that surround the sensors are used to protect them from being damaged by the fast-travelling fragments of metal diaphragms [10–14]. Such shielding designs normally leave a narrow borehole and a shallow cavity connecting the sensor surface to the ambient flow, as the two typical geometries shown in Fig. 1.

Housings with conical tips have been commonly employed in conventional pressure measurements [6,15,16]. One advantage is the less influence on the far-field flow than blunt tips. In supersonic flows where

* Corresponding author.

E-mail address: zg.wang@tum.de (Z. Wang).

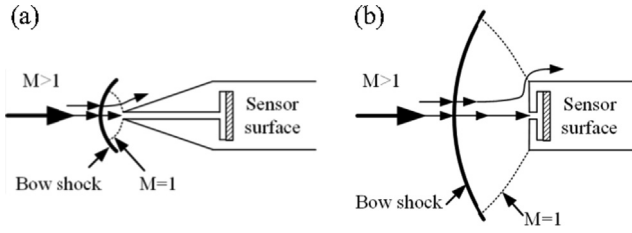


Fig. 1. Flow structures around a conical housing (a) and a blunt housing (b) in supersonic flows.

detached bow shocks are present in front of the housings, the stand-off distance is shorter for the conical tip. This would suggest less interaction of the shock with the freestream and hence, weaker effects on the downstream setup. Another advantage is that the smaller subsonic area behind the bow shock makes the conical tip less likely to be influenced by the surrounding disturbance. This would improve the measurement accuracy and consistency.

However, limited by the exterior geometry, the conical housing naturally results in a longer internal borehole than the blunt housing. Consequently, in transient pressure measurements, the wave propagation inside the conical housing would take longer time. The temporal response of the resulting pressure signal might be retarded correspondingly. In addition, at the abutting surface of the conical tip, the flow directly accelerates from the stagnation point in the center to Mach number $M = 1$ at the periphery. The area-averaged pressure over the cross section would differ from the stagnation pressure. The comparatively high curvature of the bow shock for the conical housing, which challenges the previous assumption of normal shock relations, might cause further inaccuracy to the calculation of the freestream stagnation pressure.

The present study attempts to make a thorough comparison between the conical and the blunt housings in terms of the performance in transient stagnation pressure measurements. The results would serve as general guidance on sensor housing designs.

2. Methods

2.1. Experiments

The current experimental research was carried out in a shock tube. As depicted in Fig. 2, the shock tube is composed of a driver section (3 m), a driven section (19.5 m) and a test section (0.5 m) attached to the end. The inner cross section has a diameter of 290 mm and changes to a square with the side length of 190 mm through a cookie-cutter in front of the test section. A diaphragm, which initially separates the driver and driven sections, ruptures as a critical pressure difference is reached. Subsequently, a shock wave develops and propagates towards the downstream test section and entails a flow of uniform pressure and

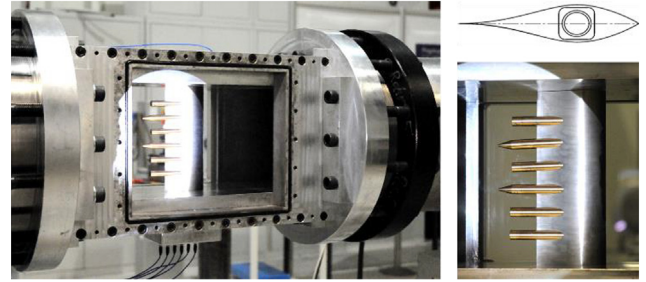


Fig. 3. Experimental Pitot rack for the stagnation pressure measurement in the test section. The incident shock arrives from left.

velocity.

In terms of the measurement system, pressure gauges and K-type thermocouples measured the initial experimental conditions at the driver and driven sections, and a NI™ cDAQ device collected the signals. Four PCB Piezotronics ICP® fast-response pressure sensors were flush-mounted along the driven section to monitor the propagation of the shock wave. An LTT device recorded the pressure data at a sampling rate of 1 MHz to determine the shock speed accurately. For visualization of the flow field inside the test section, a Z-type schlieren system was employed. A 150 W Xenon lamp served as the light source and a Shimadzu HyperVision HPV-X ultra-high-speed camera recorded 128 consecutive images of 250×400 pixels at a framing rate of 200 kfps. The resultant schlieren photographs have a resolution of 0.175 mm/pixel.

The stagnation pressure behind the incident shock wave was measured by a rack of Pitot probes in the test section, which were positioned opposite to the incoming flow as depicted in Fig. 3. The rack was built based on a modified Guderley profile to weaken the interaction with the incident shock wave and to avoid the formation of new shocks. A maximum number of six probes could be mounted on the rack and the interaction between them was experimentally verified to be negligible. From top to bottom, the second and the third slots for the probes were manufactured with a 2° downward inclination to investigate the sensitivity of the pressure measurement to the assembly misalignment.

Each Pitot probe on the rack was equipped with a PCB Piezotronics ICP® fast-response pressure transducer (Model 113B21) with a resonant frequency above 500 kHz and a rise time below 1 μs. The sensors were mounted in either conical or blunt housings, of which detailed geometries and dimensions are displayed in Fig. 4.

The conical housing has a 15° sloped surface relative to the centerline, resulting in a significantly longer borehole ($L = 3.11$) than the blunt housing ($L = 0.23$). The borehole diameter D varies among 0.36 (default), 0.45 and 0.54 and the cavity depth G ranges over 0.045 (default), 0.12 and 0.19. These two parameters were investigated separately.

The experiments were conducted under three distinct flow

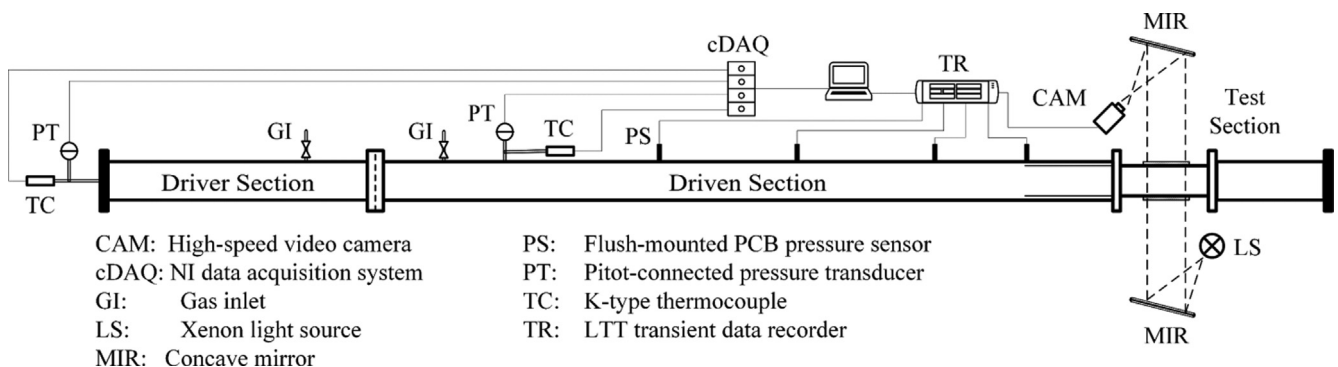


Fig. 2. Layout of the shock tube and the associated measurement system.

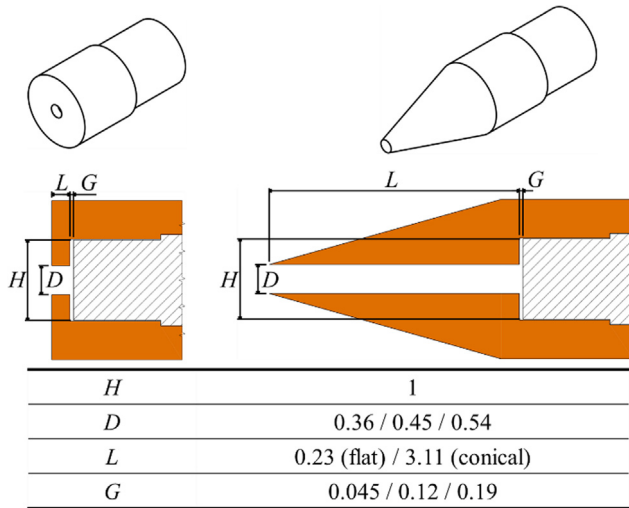


Fig. 4. Dimensions of blunt and conical housings (orange colored) normalized by the sensor tip diameter $h = 5.54$ mm. The shadowed regions represent the pressure sensors. (For interpretation of the references to colour in this figure legend, the reader is referred to the web version of this article.)

Table 1
Experimental flow conditions for the stagnation pressure measurement.

$PR = p_4/p_1$		10 ($\pm 3\%$)	100 ($\pm 2\%$)	1000 ($\pm 5\%$)
Theoretical	M_s	1.61	2.37	3.15
	M_∞	0.70	1.15	1.40
Experimental	M_s	1.50	2.24	3.01
	M_∞	0.60	1.08	1.36
	u_∞	241 m/s	518 m/s	775 m/s
	$Re_{\infty,D}$	25,000	4800	700

conditions as listed in Table 1. The driver and driven sections are filled with air to pressures p_4 and p_1 , respectively. The pressure ratio (PR) between them is varied by keeping p_4 around 7 bar while reducing p_1 , and controlled at 10, 100, and 1000, corresponding to subsonic, transonic and supersonic flow conditions in the test section. In the table, M_s , M_∞ , u_∞ and $Re_{\infty,D}$ are the Mach number of the incident shock, the Mach number of the post-shock freestream flow, the freestream velocity and the Reynolds number based on u_∞ and the default housing borehole diameter $D = 0.36$ (2 mm).

The experimental shock speed u_s was measured by monitoring the time lag between two pressure sensors mounted shortly upstream of the test section. Thus, M_s was obtained through dividing u_s by the speed of sound calculated from the driven gas temperature. Then, M_∞ and u_∞ were derived from the moving shock relations. The increased flow Mach number goes along with a decreased Reynolds number since the reduction of the flow density outweighs the increase in the flow speed.

2.2. CFD

In order to support understandings from the experiments, numerical simulations were carried out. The commercial CFD solver ANSYS FLUENT 19.1 was employed to solve a transient, compressible, two-dimensional and axisymmetric flow field. Appropriate initial and boundary conditions were assigned according to the experiments listed in Table 1. The interior and exterior surfaces of the housing were treated as no-slip walls with a fixed temperature. Air was modeled as ideal gas. For the case of $PR = 1000$, the laminar viscous model was used, while the $k-\omega$ SST turbulence model was chosen for the other two higher- Re cases.

A sufficient structured mesh with a total number of 100,000 cells was applied. In order to resolve the wall bounded flow accurately, the

dimensionless wall distance y^+ was kept around one.

3. Results and discussion

To assess the measurement accuracy, the pressure signal p is normalized by the expected pressure p_{ref} , which equals to the freestream total pressure $p_{0\infty}$ for subsonic flows and the post-bow shock total pressure \bar{p}_0 for supersonic flows. In the present experiments, the static pressure of the freestream p_∞ behind the incident shock is first derived from measured p_1 and M_s based on the moving shock relations. The value of p_{ref} is further obtained by calculating $p_{0\infty}$ from Eq. (1) or \bar{p}_0 from Eq. (4). The normalized pressure P is defined as:

$$P = (p - p_1)/(p_{ref} - p_1) \quad (5)$$

with $P = 0$ representing the initial pressure and $P = 1$ the expected stagnation pressure. Since the normalization is based on the case-specific shock strength, the influence of the slight PR variation under each flow condition is negligible.

Pressure signals measured by sensors with different housing configurations are presented in this section. Main signal features are discussed with the help of schlieren images and simulation results. Section 3.1 shows the general flow wave motions surrounding the housings. Distinct signal characteristics for each housing geometry are presented in Section 3.2. The behavior of housings at different flow March numbers is presented in Section 3.3. Effects of varying the borehole diameter and the cavity depth are discussed in Sections 3.4 and 3.5, respectively. With the preceding two sections focused on the assembly misalignment and the gelatin-filled housings, Section 3.8 wraps up the discussion by evaluating the performance of exposed sensors.

3.1. Wave dynamics around the housings

Wave dynamics in the freestream around housings is discussed with schlieren images. The associated wave motions are mainly determined by the exterior geometry of the housings, and the interior void plays a supplementary role. The wave evolution determines when the flow outside the housings becomes steady, which further influences the settling time of the measured pressure signals to a certain extent.

Fig. 5 displays the schlieren images for the blunt housing under different pressure ratios. Only the top half of the geometries are provided owing to the symmetry. For each flow condition, the left column is the first image after the impact of the incident shock on the housing and is referred as time t_0 . Shock reflection occurs at the housing front, and the reflected shock travels in the upstream direction and expands radially. According to theory, the speed of the reflected shock decreases with increasing the flow Mach number as seen in the second column. At time $t_0 + 360 \mu s$ for the subsonic flow, intense separation is observed covering the entire outer surface of the housing. Meanwhile, the reflected shock disintegrates by traveling upstream. In contrast, the reflected shock is stabilized at a certain position for the transonic and supersonic cases as detached bow shocks. During the process, there are other waves developing around the housing exteriors. But they tend to be isolated from the upstream housing tips by supersonic regions in between and hence, exert little effects on the pressure measurement.

Fig. 6 shows the schlieren images for the conical housing. The flow fields exhibit certain resemblance to those in Fig. 5. In the first column, the incident shock is reflected at the housing tip and the sloped surface. The resulting reflected shock is substantially weaker than that for the blunt housing. For the supersonic flow, there is barely any reflection observable, as the flow density is considerably low making the schlieren phenomena less effectual. Shock positions in the second column show that, the reflected shock propagates upstream at a much lower velocity than cases with the blunt housing. For the two cases with $M_\infty > 1$, the reflected shock gradually settles down as a detached bow shock, similarly to the observations in Fig. 5. But as shown in the third column, the stand-off distance is relatively small and the shock profile is strongly

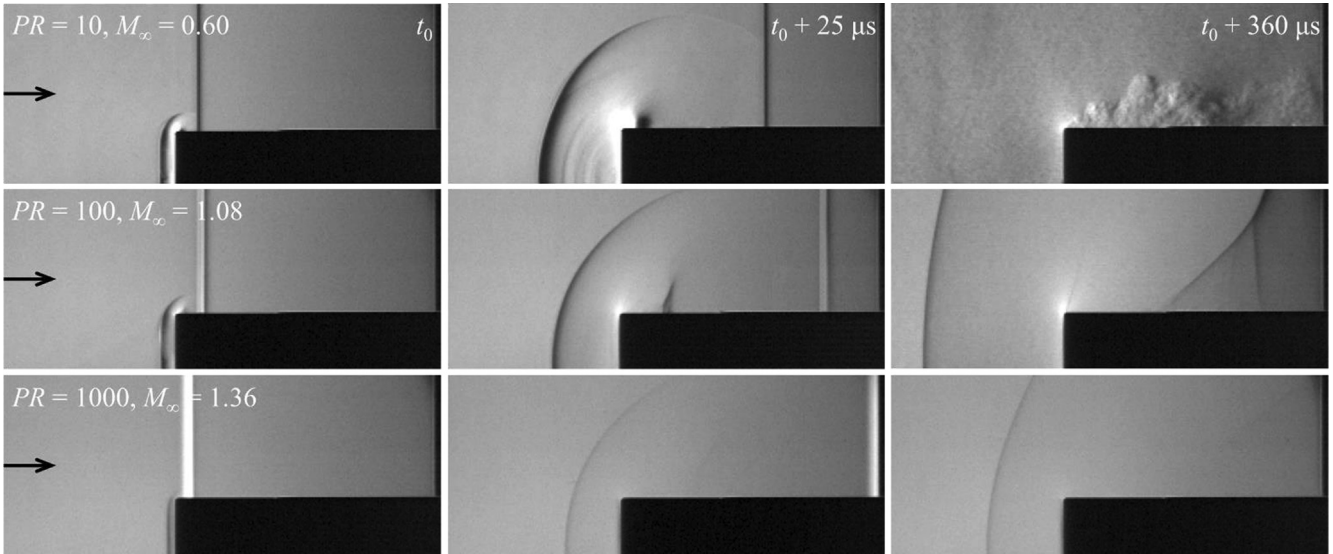


Fig. 5. Schlieren images of the flow field around the upper half of the sensor with the blunt housing. The incident shock and the induced freestream flow propagate from left to right. Each row corresponds to a certain flow Mach number, while each column to a specified time moment.

curved.

From the viewpoint of shock structures, the less-curved bow shock for the blunt housing satisfies the presumption of normal shock relations better. Hence, the blunt housing is expected to give more accurate pressure measurements. As to the duration of the transient wave motions, it is difficult to determine the exact moments for the waves to become stabilized. But a general trend is that the wave settling time declines as the flow velocity increases.

3.2. Characteristic pressure signals

Pressure signals measured by sensors with blunt and conical housings under identical flow conditions are compared in this section. The signal characteristics are closely related to the flow evolution inside the housings. The analyses of wave motions in Schlieren images accompanied with the simulation results provide insight into the internal flow features. In following figures, the experimental time t is regarded as zero at the initiation of the signal rise.

Fig. 7 shows the pressure signals measured with blunt and conical housings at $PR = 100$ for a comparison of respective signal features.

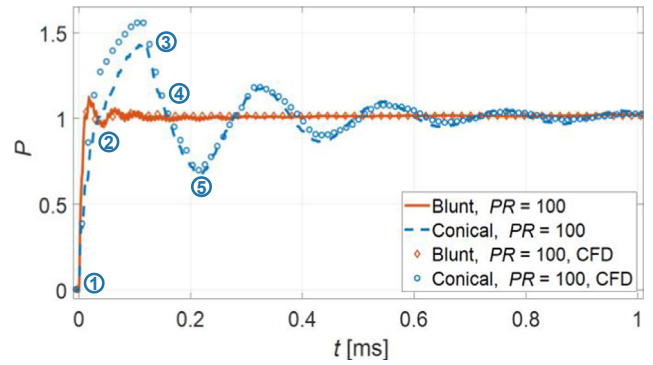


Fig. 7. Normalized pressure signals for blunt and conical housings ($D = 0.36$, $G = 0.045$) at $PR = 100$.

The signal for the sensor shielded by the blunt housing surges upwards at the beginning and exhibits a weak overshoot. The pressure soon becomes stabilized at the expected value after a short period of weak oscillations. In contrast, the signal for the conical housing rises slowly

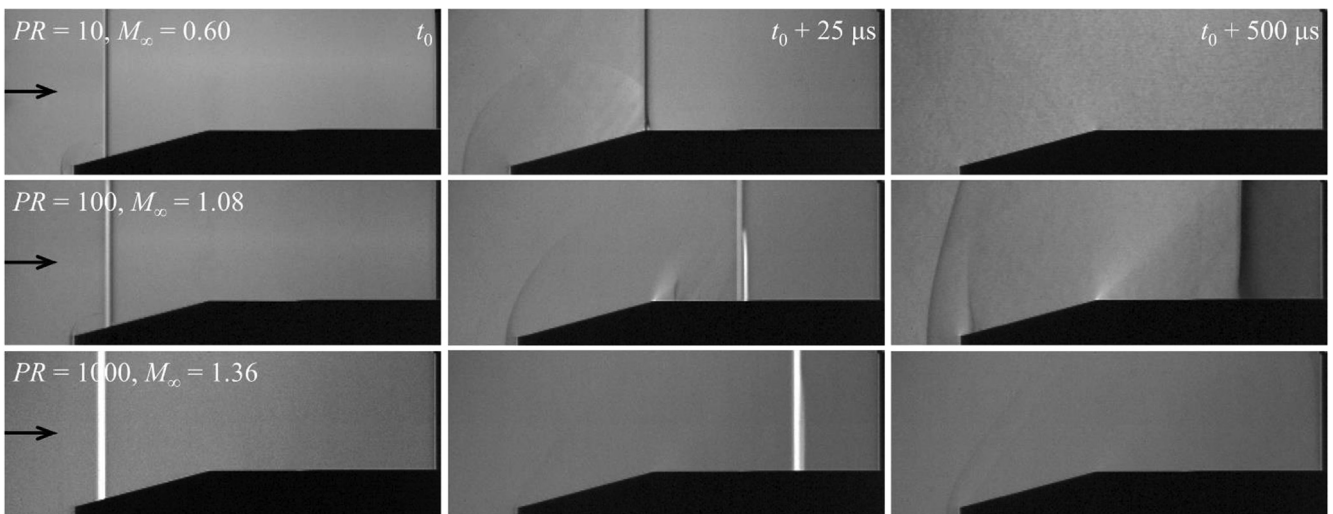


Fig. 6. Schlieren images of the flow field around the upper half of the sensor with the conical housing. The incident shock and the induced freestream flow propagate from left to right. Each row corresponds to a certain flow Mach number, while each column to a specified time moment.

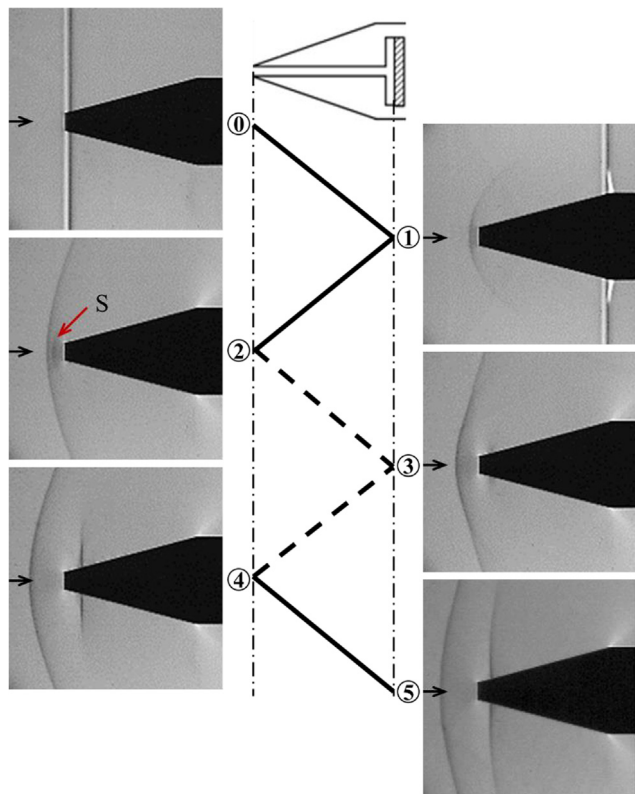


Fig. 8. Sketch of the wave dynamics inside the conical housing and schlieren images of the wave motions outside. Solid lines represent shock waves, and dashed lines expansion waves.

to the reference value and reaches a strong overshoot. Through a long lasting of large-amplitude oscillations, the signal gradually settles down around the expected value.

The strong oscillations for the conical housing arise from the wave motions inside the housing void. A sketch of the speculated wave dynamics in the borehole is displayed in Fig. 8. Schlieren images at specified time moments are also provided to present external flow fields. The plotted solid lines represent shock waves and the dashed lines expansion waves. The numeric labels correspond to the time moments in Fig. 7.

When the incident shock impacts on the housing tip, part of the shock propagates into the borehole/cavity and entails a flow behind. At the time moment ①, this shock gets reflected at the sensor surface and causes the pressure signal to start rising. The reflected shock travels upstream, and meets the external freestream at the borehole inlet. A weak shock, which is labelled as “S” in the schlieren image ②, is emitted from the housing tip towards the detached bow shock. Meanwhile, since the gas inside the borehole is over-compressed by the incident shock and the succeeding reflected shock, an expansion wave travels from the borehole inlet inwards and reduces the flow pressure. The pressure signal begins to drop when the expansion wave arrives at the sensor tip at ③. The subsequent reflected expansion wave over-expands the flow, decreasing the flow pressure below the reference value. At ④, this reflected expansion wave reaches the housing tip and interacts with the external flow, releasing a new shock into the borehole. As this shock arrives at the sensor tip at ⑤, the pressure signal is re-boosted and one cycle of the oscillations is completed. One point of interest is that during this process, the detached bow shock moves back and forth slightly, at a synchronized pace with the pressure oscillations. The wave dynamics inside the blunt housing occurs in a similar pattern, but at a much faster rate due to the significantly shorter borehole length.

Although supported by the schlieren images, the wave motions sketched in Fig. 8 are oversimplified. Effects of viscous dissipation, heat

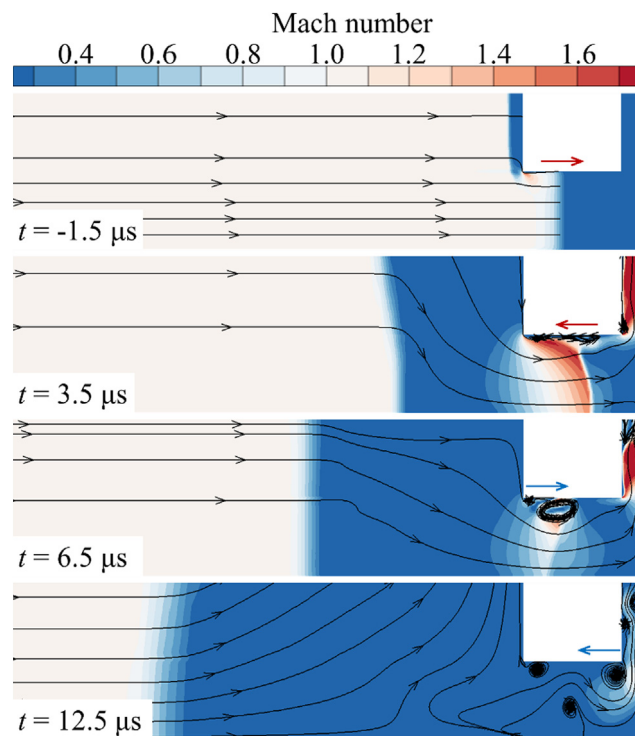


Fig. 9. Mach number contours with arrowed streamlines in the borehole for the blunt housing at $PR = 100$. The red and the blue arrows indicate the moving directions of the shock and the expansion waves, respectively. (For interpretation of the references to colour in this figure legend, the reader is referred to the web version of this article.)

transfer and flow mixing are still to be revealed. Hence, the simulation results are also presented here to verify the main ideas delivered in Fig. 8 and supplement further details. The pressure signals obtained from the numerical simulations are also included in Fig. 7 for validation. The experimental and the numerical results match reasonably well, with certain discrepancies in the signal overshoot which could be caused by the simplified isothermal boundary conditions imposed on the housing surfaces.

Fig. 9 presents the Mach number contours with arrowed streamlines inside the blunt housing at $PR = 100$. Only the upper half of the cross section is displayed due to the symmetry. The contours at $t = -1.5 \mu s$ clearly show that part of the incident shock propagates into the borehole. At $t = 3.5 \mu s$ after the shock gets reflected, the post-shock high-pressure region serves as a reservoir to fill the cavity in front of the sensor tip. The flow chokes around the cavity corner under the high pressure ratio. At $t = 6.5 \mu s$ the newly developed expansion wave departs from the borehole inlet and arrives at the sensor tip at $t = 12.5 \mu s$. Then the choking behavior disappears and the filling of the cavity is interrupted. Indicated by the streamlines at the housing front, there is no more flow into the borehole at this time moment, and the pressure measured by the sensor starts to drop.

The Mach number contours inside the conical housing at $PR = 100$ are shown in Fig. 10, of which the left column corresponds to the region near the housing tip and the right column in front of the sensor surface. Similar behavior, such as the reflection of the incident shock at the sensor surface and the propagation of the new expansion wave into the borehole, is present. But as expected, the corresponding time period is largely elongated. A choking throat also appears at the corner during the cavity filling process ($t = 5 \mu s$). At $t = 78 \mu s$ before the arrival of the expansion wave (which can be identified at $t = 110 \mu s$ by the change of the flow direction), the choking phenomenon already vanishes, indicating that the cavity has been filled up to a relatively high pressure level.

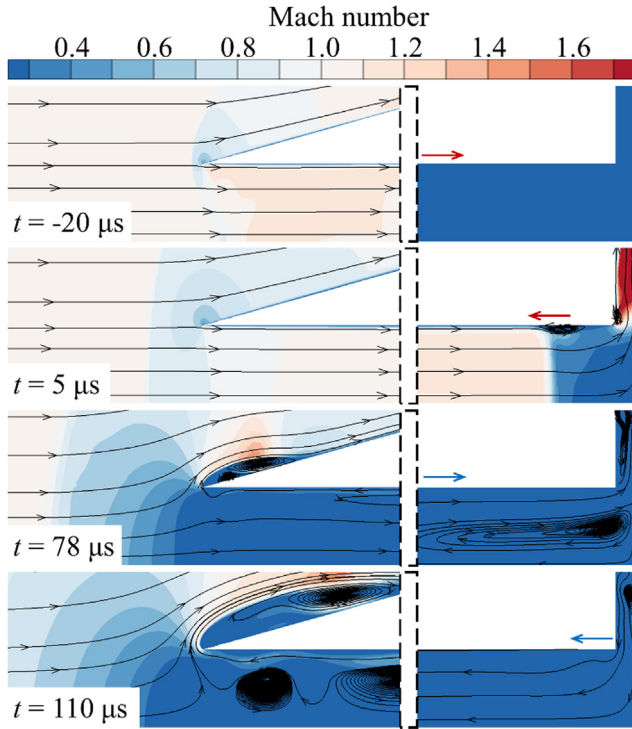


Fig. 10. Mach number contours with arrowed streamlines near the borehole inlet (left) and near the sensor tip (right) for the conical housing at $PR = 100$. The red and the blue arrows indicate the moving directions of the shock and the expansion waves, respectively. (For interpretation of the references to colour in this figure legend, the reader is referred to the web version of this article.)

The simulation results generally agree well with the hypothetical wave dynamics inside the housings presented in Fig. 8. Some details such as the choking behavior in the cavity are supplemented in Figs. 9 and 10. With this understanding, specific properties of the pressure signals shown in Fig. 7 are analyzed individually as follows.

The rise time, which is traditionally defined as the time period for the signal to rise from 10% to 90% of the steady value, is mainly determined by the initial mass flow rate of the cavity filling. A higher mass flow rate consumes less time to fill the cavity up to the reference pressure, meaning a shorter rise time. As indicated in Fig. 9 ($t = 3.5 \mu\text{s}$) and Fig. 10 ($t = 5 \mu\text{s}$), the flow is choked around the cavity corner at the beginning of the filling process for both blunt and conical housings. Then the filling mass flow rate solely depends on the total pressure of the flow ahead of the choking throat, considering the choking area is the same. Fig. 11 compares the total pressure distribution inside the borehole between the two housing designs at respective filling moments. The total pressure p_0 is normalized by the expected reference pressure p_{ref} . For the blunt housing, the total pressure is raised noticeably above p_{ref} , since the reflected shock in front of the housing is moving against the incoming flow. However, for the conical housing, the frontal reflected shock is rather weak and exerts little effects on the flow total pressure ($p_0/p_{\text{ref}} \sim 1$). As a result, the filling mass flow rate for the conical housing is relatively low and the rise time is comparatively long.

The maximum overshoot represents the peak value of the signal. The overshoot behavior is caused by the reflection of the incident shock inside the housing void, which over-compresses the flow and tends to fill the cavity to the pressure higher than p_{ref} . For the blunt housing, the filling process is interrupted by the arrival of the expansion wave at the sensor surface as illustrated in Fig. 9 ($t = 12.5 \mu\text{s}$). Hence, the maximum overshoot is suppressed at a low level. However, the conical housing experiences a fairly complete filling process and the resulting overshoot is much stronger.

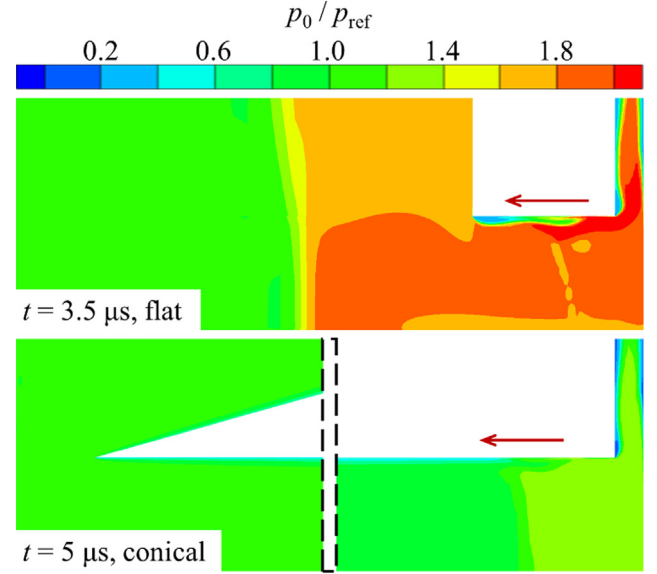


Fig. 11. Normalized total pressure contours inside the borehole for the blunt (top) and the conical (bottom) housings at $PR = 100$.

The oscillation frequency of the signal is dominated by the wave propagation inside the housing void as previously explained. For experiments under the same flow condition, the wave travelling speeds tend to remain similar, with limited variations caused by changes in the housing geometries or dimensions. Then the borehole length plays the decisive role to determine the oscillation period. The conical housing, which has a significantly longer borehole, naturally yields a much lower oscillation frequency.

The settling time, defined in a conventional way as the time taken by the signal to become stabilized within the $\pm 5\%$ interval of the steady value, depends on the decay rate of the oscillation amplitudes. The amplitude attenuation is partially caused by the energy exchange between the flow inside and outside of the housings through shock waves and expansion waves. Such communications drive the pressure in the housing void to reach a balance with the external freestream. Another reason for the amplitude dampening is the energy dissipation brought by viscous friction and heat transfer at the housing interior walls. Under the same flow condition ($Re_{\infty, D} = 4800$), strengths of the wall viscous stress and the wall heat flux are similar between blunt and conical housings. However, the frequent wave motions inside the blunt housing (owing to the short borehole length) efficiently exchange the pressure information with the outside freestream, restraining the cavity ahead of the sensor from being over-filled or over-drained. Comparatively, the communication between the cavity in the conical housing and the external flow field is retarded by the long borehole, resulting in a slow oscillation attenuation and a long settling time.

Overall speaking, the performance of the blunt housing is superior to the conical housing, in terms of the stagnation pressure measurements. The signal exhibits a shorter rise time, a weaker overshoot and a faster settling down.

3.3. Effect of the flow conditions

For each housing configuration, experiments are carried out under three flow conditions as listed in Table 1. The performance of blunt and conical housings in subsonic, transonic and supersonic flows are compared and discussed in this section.

Figs. 12 and 13 compare the pressure signals for blunt and conical housings at distinct flow conditions, respectively. The shadowed ribbons backgrounding each line represent the corresponding measurement uncertainty as 95% confidence intervals. The calculation is based

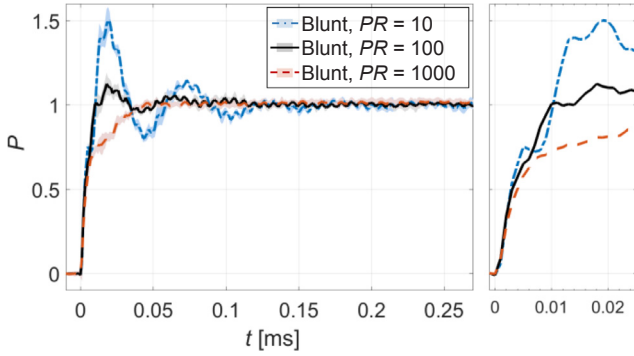


Fig. 12. Normalized pressure signals for the blunt housing ($D = 0.36$, $G = 0.045$) at different flow conditions, with the shadowed ribbons representing the measurement uncertainty. The right plot is a zoomed view of the initial pressure jump.

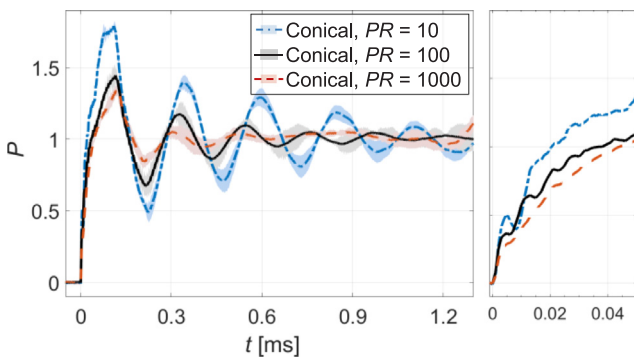


Fig. 13. Normalized pressure signals for the conical housing ($D = 0.36$, $G = 0.045$) at different flow conditions, with the shadowed ribbons representing the measurement uncertainty. The right plot is a zoomed view of the initial pressure jump.

on the t -distribution analyses of at least four repeated experiments. The uncertainty for blunt housings is relatively small and falls within $\pm 2.5\%$. Conical housings exhibit a higher uncertainty level, especially at the oscillation peaks and troughs where a broadest range of $\pm 10\%$ is reached locally. But the characteristic signal patterns remain clearly identified. The general distinctions previously observed between blunt and conical housings are maintained at different flow conditions.

Rise times, maximum overshoots and settling times for all cases are summarized in Fig. 14. One point of notice is the drastic difference in the settling time between the two housing designs. By adopting the blunt housing, the settling time is reduced by one order of magnitude, which is of essential importance for experiments with short time windows. Another interesting point is the absence of the signal overshoot for the blunt housing at $PR = 1000$. The signal climbs slowly to the reference value and settles down immediately without further oscillations. This behavior suggests that a non-overshooting rapidly-settled signal is achievable for the stagnation pressure measurement by manipulating the sensor housing geometries.

As to the effect of the flow conditions, there appears a consistent tendency of increasing the rise time, lowering the maximum overshoot, raising the oscillation frequency and reducing the settling time as the flow changes from subsonic to supersonic conditions. These points are discussed with the help of simulation results shown in Fig. 15. Mach number contours inside the conical housing are presented at the moment when the cavity is still filling. Considering the change in the flow condition exerts similar effects on the two housing designs, only cases of the conical housing are provided.

Rise Time. As shown in Fig. 15, a separation bubble at the borehole wall appears for all flow conditions, due to the interaction of the reflected shock with the boundary layer. This separation bubble blocks

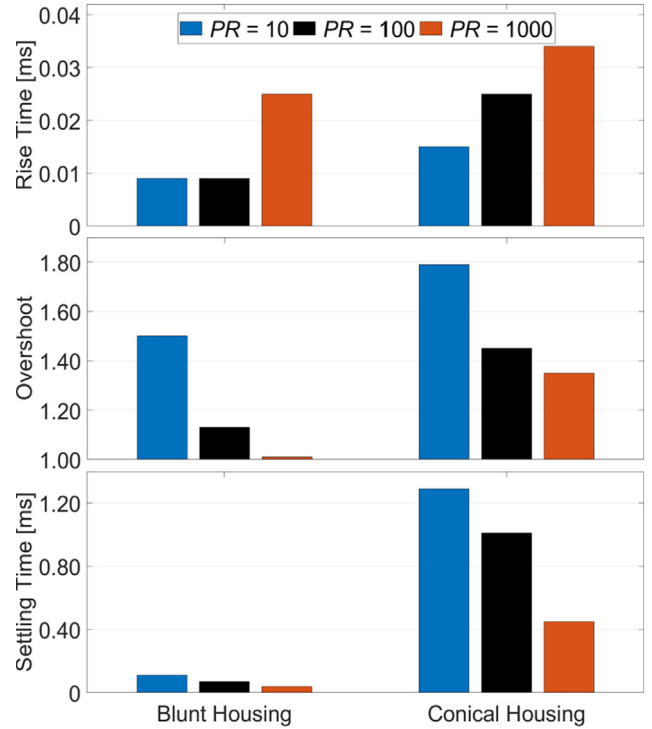


Fig. 14. Comparison of rise times (top), maximum overshoots (middle) and settling times (bottom) between blunt and conical housings at different flow conditions.

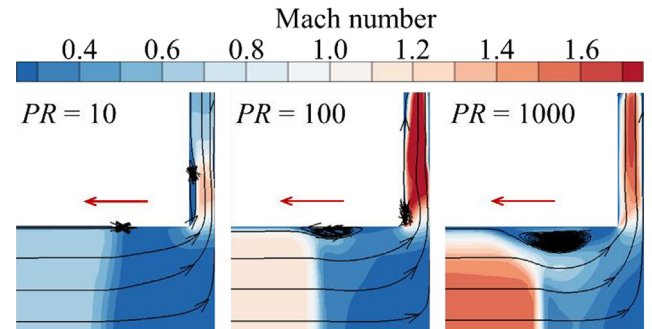


Fig. 15. Comparison of the Mach number contours in front of the sensor surface during the cavity filling process for the conical housing at different flow conditions ($t = 5 \mu s$).

the cross section of the borehole and absorbs part of the incoming flow into the recirculation region instead of filling the downstream cavity. For cases with higher M_s and correspondingly lower $Re_{\infty, D}$, the pressure gradient across the shock is stronger and the boundary layer developed is thicker, of which both contribute to a larger separation bubble. As a consequence, the blocking effect is enhanced and the resulting rise time is extended.

Maximum Overshoot. An analytical calculation of one-dimensional shock waves shows that the reflection of the incident shock could ideally cause a maximum overshoot of 2.06, 1.89 and 1.74 for subsonic, transonic and supersonic flow conditions, respectively. Due to the filling of the cavity ahead of the sensor, the overshoots of the experimental signals are consistently lower than the theoretical values. However, this tendency of weakening the overshoot with increasing the flow Mach number is preserved.

Oscillation Frequency. Figs. 16 and 17 plot the fast Fourier transform (FFT) spectrum of the pressure signals measured for blunt and conical housings, respectively. As the flow Mach number increases from subsonic to supersonic conditions, the spectrum peaks shift towards mildly

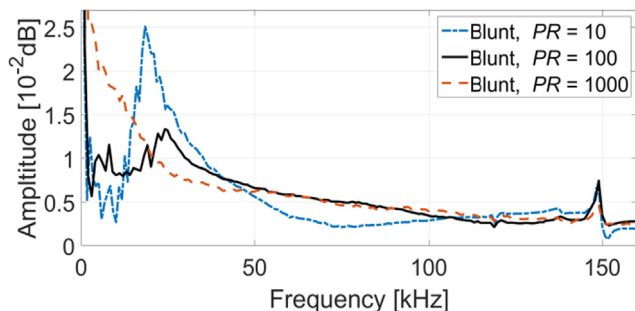


Fig. 16. FFT spectrum of the pressure signals measured for the blunt housing.

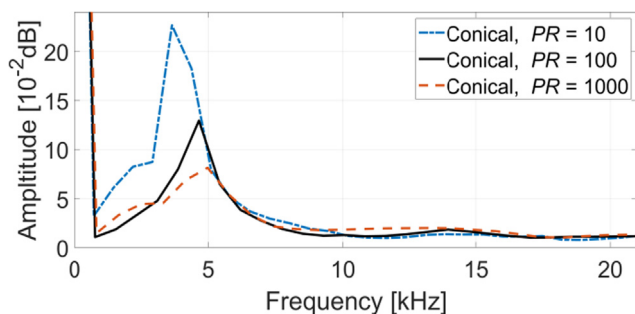


Fig. 17. FFT spectrum of the pressure signals measured for the conical housing.

higher frequencies (from 18 kHz to 24 kHz for blunt housings, and from 4 kHz to 5 kHz for conical housings). Interestingly, conical housings have boreholes 14 times longer than blunt housings, but the corresponding oscillation frequencies of the measured signals are only four to five times lower. This might be attributed to the influence of the cavity filling on the oscillation period. For the blunt housing at $PR = 1000$, no distinguishable peak exists in the spectrum, which agrees with the observation in Fig. 12 that the viscous damping slows down the filling process and restrains signal oscillations. Peaks at the frequency 149 kHz for blunt housings correspond to the small-amplitude periodic fluctuations in Fig. 12. Conical housings exhibit similar peaks at 136 kHz, which is not presented in Fig. 17 for concision. The most likely explanation is that these high-frequency fluctuations arise from the wave motions inside the tiny gap around the lateral surface of the sensor. This gap is 6 mm long and merely 0.06 mm thick, and preserved for a smooth assembly into the housing. Since these noises exert negligible effects on the transient response of the signals, they are filtered out from the pressure data presented in following figures by a low-pass 100 kHz filter.

Settling Time. In the experiments, increasing flow Mach number is accompanied with decreasing flow Reynolds number as shown in Table 1. The lower Re results in stronger viscous dissipation. Increasing the flow speed also enhances the heat convection at the housing interior walls. Consequently, a stronger dampening of the oscillation amplitudes is expected for higher flow Mach numbers, and the resulting signal settling time is correspondingly shorter.

As a short summary, for experiments with higher pressure ratios, the signal overshoot is intensified and the oscillation frequency is raised due to the increasing flow Mach number. Meanwhile, the decreasing Reynolds number elongates the rise time but shortens the settling time.

3.4. Effect of the borehole diameter

Modifications of the housing interior dimensions, including the borehole diameter and the cavity depth, are examined and the associated effects on the stagnation pressure measurement are evaluated. In this section, the influence of the borehole diameter is discussed by comparing results of the housings with $D = 0.36, 0.45$ and 0.54 .

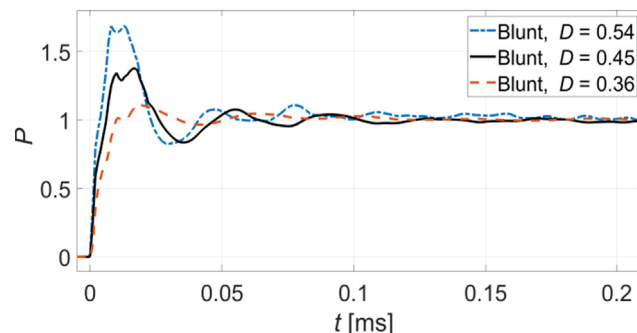


Fig. 18. Normalized pressure signals for the blunt housing ($G = 0.045$) with three different borehole diameters at $PR = 100$.

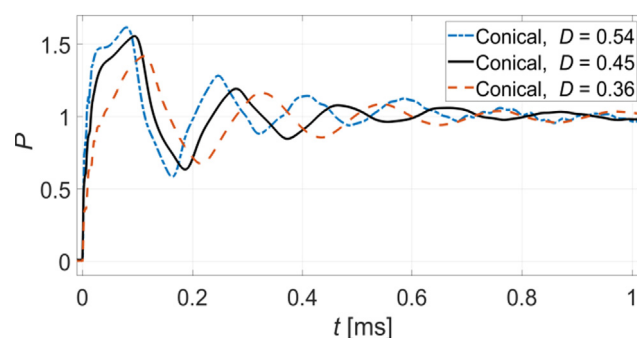


Fig. 19. Normalized pressure signals for the conical housing ($G = 0.045$) with three different borehole diameters at $PR = 100$.

The pressure signals measured by the blunt and the conical housings with different borehole diameters are presented in Figs. 18 and 19, respectively. Similar trends of the signal changes are observed for the two different housings. Larger borehole diameters bring about shorter rise times, distinctly stronger overshoots and higher-frequency oscillations. Simulation results of the Mach number and total pressure contours inside the conical housing are provided in Fig. 20 to supplement the discussion.

Rise Time. In an ideal case where no cavity exists at the end of the borehole, the reflected shock would induce a stationary field behind it. But the fact that a certain amount of flow is drawn into the cavity attenuates the strength of the reflected shock. For cases with larger borehole diameters, the amount of flow into the cavity takes up a smaller proportion of the incoming flow, thus leading to a less reduction of the reflected shock strength. This is verified in Fig. 20 where the total pressure behind the reflected shock is the highest for $D = 0.54$ and the lowest for $D = 0.36$. Consequently, the mass flow rate for the cavity filling is relatively high for housings with wide boreholes, and the respective rise times are comparatively short. The fact that the cavity volume is reduced as the borehole diameter expands, also contributes to the decreasing rise time.

Maximum Overshoot. As mentioned before, the maximum overshoot obtainable by the pressure signal is limited by the strength of the reflected shock. Although the cavity is not fully filled up to this limit, it provides reasonable indications on the overshoot strength. Since the reflected shock is enhanced by increasing the borehole diameter, a higher maximum overshoot is expected correspondingly. From Figs. 18 and 19, it is observed that the promotion of the signal overshoots as the borehole expands is more pronounced for the blunt housing. At $D = 0.54$, its maximum overshoot even overtakes that for the conical housing.

Oscillation Frequency. The enhancement of the reflected shock with increasing the borehole diameter is also reflected in higher shock speed. This can be inferred from the shock positions in Fig. 20. Consequently, the faster wave motions give rise to higher signal oscillation

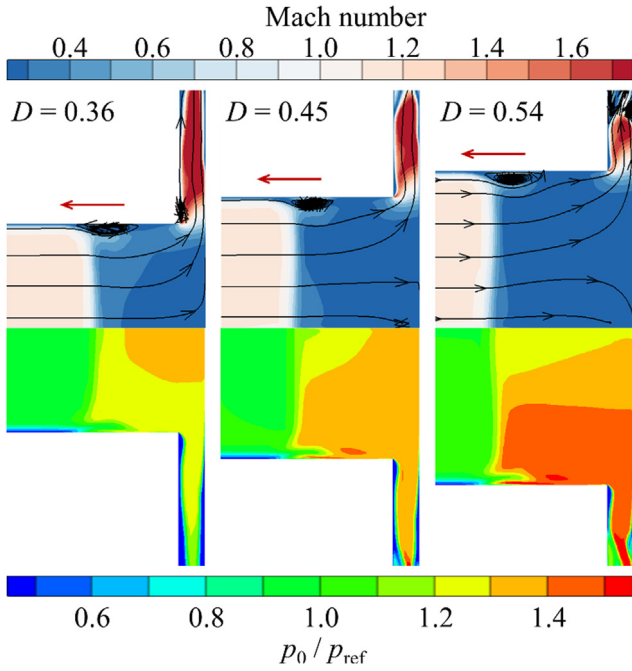


Fig. 20. Contours of the Mach number (top) and the total pressure (bottom) in front of the sensor surface during the cavity filling process for the conical housing with different borehole diameters under $PR = 100$ at $t = 5 \mu s$.

frequencies. One point of notice is that when the borehole diameter of the conical housing is expanded, the borehole is shortened accordingly to maintain the same sloped exterior. Hence, the reduction of the borehole length is another important contributor to the increase in the oscillation frequency for conical housings.

To sum up, increasing the borehole diameter mainly works to strengthen the reflected shock, which further exerts effects on the signal rise time, the overshoot and the oscillation frequency. The signal overshoot seems particularly sensitive to the borehole diameter for the blunt housing, and a proper selection might completely remove the overshoot.

3.5. Effect of the cavity depth

This section intends to analyze the influence of the cavity depth. The experimental results for blunt and conical housings with $G = 0.045$, 0.12 and 0.19 are presented in Figs. 21 and 22, respectively.

As the cavity depth increases, the signal rise time is extended consistently while the overshoot only varies within a very limited range. For the conical housing, another noticeable change is the prolongation of the oscillation period. The simulated Mach number and total pressure contours inside the conical housing are presented in Fig. 23 for further

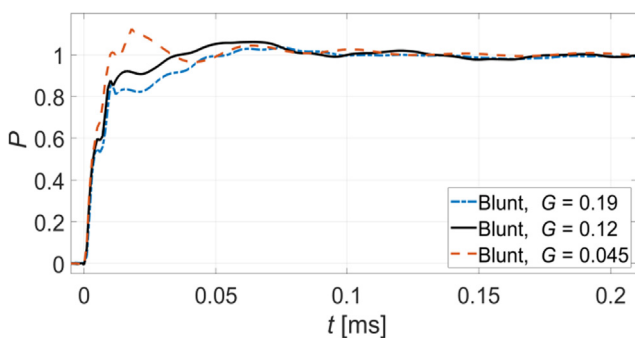


Fig. 21. Normalized pressure signals for the blunt housing ($D = 0.36$) with three different cavity depths at $PR = 100$.

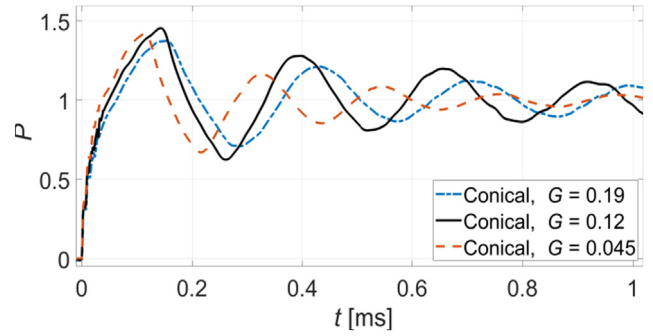


Fig. 22. Normalized pressure signals for the conical housing ($D = 0.36$) with three different cavity depths at $PR = 100$.

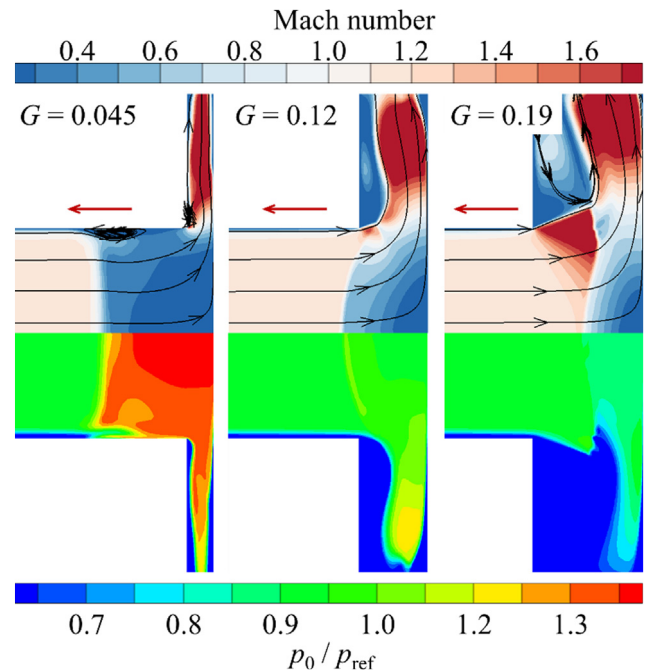


Fig. 23. Contours of the Mach number (top) and the total pressure (bottom) in front of the sensor tip during the cavity filling process for the conical housing with different cavity depths under $PR = 100$ at $t = 5 \mu s$.

analyses.

Rise Time. For larger cavity depths, a higher proportion of the post-shock fluid is absorbed into the cavity. Correspondingly the reflected shock becomes weaker, compressing the flow to a lower pressure level as shown in Fig. 23. The simulation results present another distinct change in the flow structure. A large separation bubble is induced across the cavity corner and blocks over half of the entire cross section at $G = 0.19$. Therefore, for cases with larger cavity depths, the decreasing total pressure plus the shrinking choking area results in a less-adequate mass flow rate for the cavity filling, which accounts for the longer rise time.

Maximum Overshoot & Oscillation Frequency. Since the strength of the reflected shock decreases as the cavity depth increases, a lower overshoot is expected. The accompanied decrease in the shock velocity results in a lower oscillation frequency.

In general, increasing the cavity depth exerts opposite effects to increasing the borehole diameter. This implies that the volume ratio between the cavity and the borehole could serve as a general indicator of the housing performance.

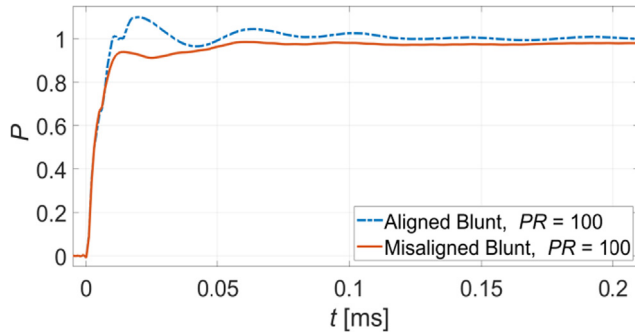


Fig. 24. Normalized pressure signals for the aligned and the 2° misaligned blunt housings ($D = 0.36$, $G = 0.045$) at $PR = 100$.

3.6. Effect of the assembly misalignment

One practical problem involved in pressure measurements is the misaligned mounting of sensors. To correctly measure the flow stagnation pressure, the sensor is supposed to be directed exactly opposite to the freestream flow direction. This requirement is not always satisfied, considering the assembly accuracy and the flow uniformity. Thus, evaluation of the sensitivity of the measurement setup on the mounting misalignment is necessary.

Figs. 24 and 25 present the pressure signals measured by the 2° misaligned sensors under $PR = 100$ for blunt and conical housings, respectively. As shown, inclining the sensor by 2° exerts negligible effects on the signal rise time and the oscillation frequency. However, a reduction is identified for the maximum overshoot, the oscillation amplitudes, and more importantly the steady value. Results of the other two flow conditions, which are not shown here for the sake of concision, have the same tendencies.

The misalignment between the housing centerline and the incoming freestream direction brings subtle changes to the housing configuration. On one hand, the effective cross section of the borehole to receive the incident shock is reduced. The resulting behavior is expected to resemble a housing with a smaller borehole. Based on the observations in Figs. 18 and 19, the reduction of the overshoot and the decrease in the oscillation amplitudes are as expected. On the other hand, the cross section of the borehole inlet is not perfectly normal to the incoming flow. Thus the presumed stagnation condition at the housing tip is not fulfilled. With only part of the flow dynamic pressure accounted for, a measurement signal lower than the stagnation pressure is expected.

Table 2 lists the steady values of the pressure signals measured in different cases. For the conical housings under $PR = 10$ and $PR = 100$, the pressure signals still exhibit a certain degree of oscillations at the end of the available experimental time. Thus the corresponding steady values are calculated as the averaged pressure over the last oscillation period. As shown in Table 2, the misaligned mounting decreases the measured pressure by a maximum of 4.08%. For both housing designs,

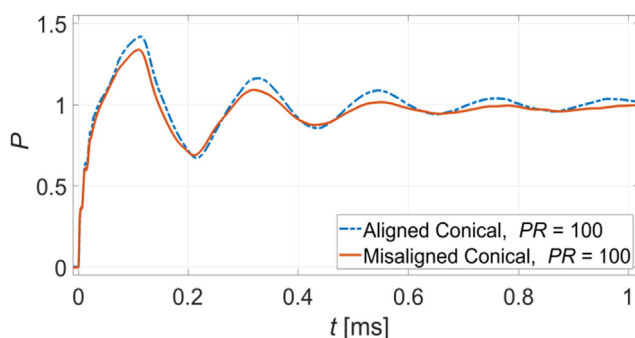


Fig. 25. Normalized pressure signals for the aligned and the 2° misaligned conical housings ($D = 0.36$, $G = 0.045$) at $PR = 100$.

Table 2

Steady values of the pressure signals measured by aligned and misaligned sensors with blunt and conical housings.

Pressure ratio PR		10	100	1000
Blunt	Aligned	1.0001	1.0018	1.0037
	Misaligned	0.9807	0.9783	0.9726
	Drop	1.92%	2.35%	3.11%
Conical	Aligned	0.9998	0.9967	0.9933
	Misaligned	0.9674	0.9614	0.9525
	Drop	3.26%	3.53%	4.08%

the decrement grows as the flow Mach number increases, meaning that the supersonic flow is more sensitive to the misalignment than the subsonic flow. Under the same flow condition, the conical housing consistently gives a higher pressure reduction than the blunt one. Hence, the former design has a higher demand for the mounting accuracy.

3.7. Effect of filling the housing with gelatin

Filling the housing interior void with oil or grease is one of the methods previously proposed to accelerate the temporal response [17,18]. The idea is that the acoustic information would be delivered faster between the inside and the outside of housings due to the comparatively high sound speed in oil/grease, and the filling process would be eliminated because of the corresponding low compressibility.

To estimate the performance of this method in stagnation pressure measurements, experiments with the housing interior filled with gelatin are conducted. The gelatin is made from a mixture of distilled water, Gelrite™ Gellan gum and magnesium sulfate with the respective mass proportion of 10,000:6:5. The speed of sound in the gel is experimentally measured to be 1480 m/s. To prevent water evaporation and to avoid expansion of the tiny bubbles possibly trapped in the gelatin, only the low pressure ratio $PR = 10$ is studied, which corresponds to the subsonic flow condition.

Figs. 26 and 27 show the pressure signals measured for the gelatin-filled blunt and conical housings at $PR = 10$. With housings filled with gelatin, the signal rise time is reduced approximately to $2\mu\text{s}$, since the low compressibility of the filler shortens the cavity filling process significantly. Meanwhile, the overshoot is intensified noticeably, which is caused by the change in the wave motion pattern. For gelatin-filled housings, the shock wave experiences the first reflection at the air-gelatin interface, that is, at the borehole inlet. Due to the dramatic difference of the acoustic impedance between air and gelatin, this reflection happens in an almost ideal manner and increases the pressure behind the reflected shock to a level close to p_{peak} . To maintain the pressure balance across the air-gelatin interface, a compression wave is induced and propagates into the borehole. A second reflection occurs as the compression wave reaches the sensor surface and boosts the

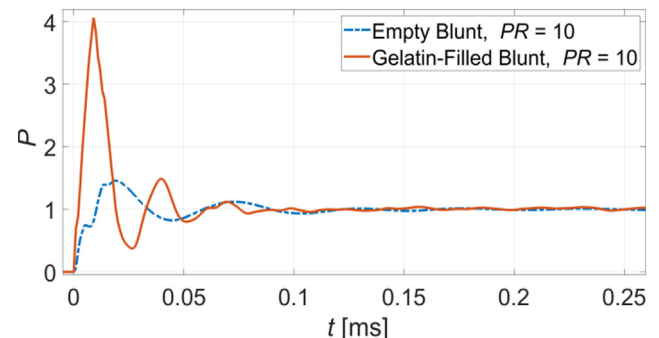


Fig. 26. Normalized pressure signals for the empty and the gelatin-filled blunt housings ($D = 0.36$, $G = 0.045$) at $PR = 10$.

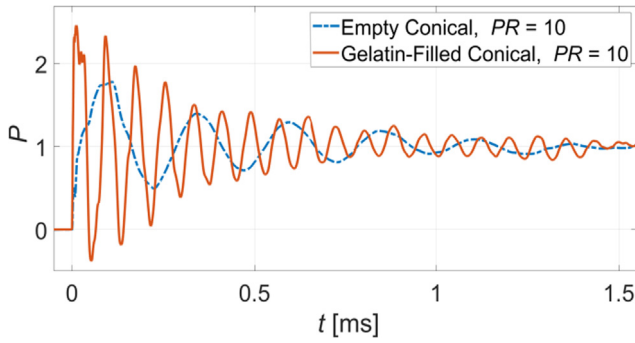


Fig. 27. Normalized pressure signals for the empty and the gelatin-filled conical housings ($D = 0.36$, $G = 0.045$) at $PR = 10$.

pressure to an even higher value, which is responsible for the stronger overshoot. In addition, the signal oscillation frequency is tripled by filling housings with gelatin, owing to the increase in the sound speed. Interestingly, the oscillation amplitudes decay almost at the same rate as cases of empty housings. Consequently, the settling time is nearly unchanged by the gelatin filling.

As noticed, the gelatin-filled blunt housing exhibits a much higher overshoot than the gelatin-filled conical one. This might be related to the strength of the reflected shock at the air-gelatin interface. For the blunt housing, the central part of the reflected shock decays comparatively slowly due to the extensive frontal surface, sending a stronger compression wave into the gelatin than the conical housing.

Overall speaking, the gelatin-filled housings exhibit no superior performance to the empty housings in the stagnation pressure measurements. Instead, the resulting strong overshoots put more burdens on the pressure sensors.

3.8. Behavior of the exposed sensors

The previous sections show that shielding the sensor involves some negative drawbacks onto the measurement itself. The cavity and the borehole connecting it to the ambience both affect the signal rise time and involve overshoots and oscillations. Therefore, two sensor holders without protective housing (as shown in Fig. 28) are finally examined.

Fig. 29 summarizes the pressure signals measured with exposed-front blunt and conical holder geometries at different flow conditions. With the absence of boreholes and cavities in front of the sensors, all signals exhibit one pronounced overshoot and settle down rapidly without preceding oscillations. It is noteworthy, however, that the overshoot of the blunt holders is much stronger, but rests to the correct value, while the conical housing gives a constant pressure, which is

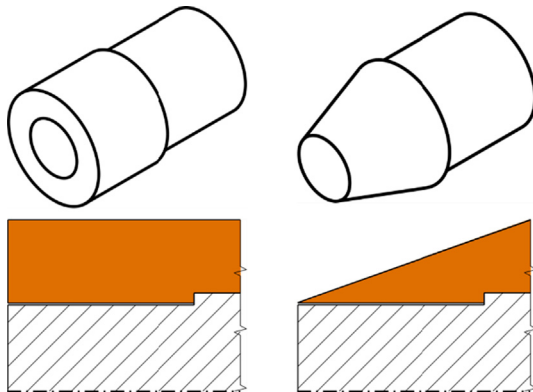


Fig. 28. Configuration of blunt and conical holders (orange colored) with sensors (shadowed) exposed to the freestream. (For interpretation of the references to colour in this figure legend, the reader is referred to the web version of this article.)

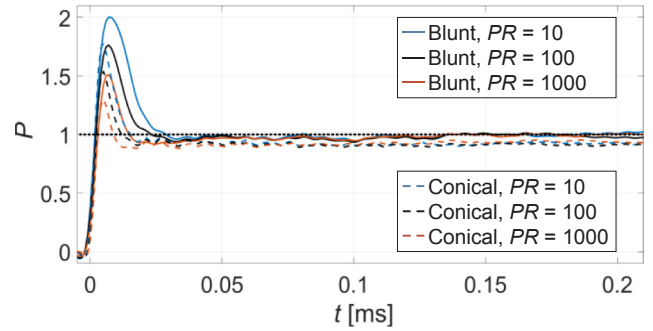


Fig. 29. Normalized pressure signals for exposed sensors in blunt and conical holders at different flow conditions. The black dotted line represents $P = 1$.

about 6% below the reference value.

Maximum Overshoot. For exposed sensors, the incident shock impacts on the entire sensor surface and is subsequently reflected. Hence, overshoots in the range of the previously mentioned theoretical values of 2.06, 1.89 and 1.74 are to be expected. The experimental outcomes for the blunt holders (2.00, 1.76 and 1.51) match the theoretical values well, but the quantitative discrepancy is widened for higher Mach numbers. The reason is simply the higher speed of sound behind the reflected shock and the correspondingly faster adaptation of the pressure field. The maximum overshoots for the conical holders are consequently even lower (1.77, 1.54 and 1.30) since the flow is immediately accelerated to the rim of the sensor surface.

Settling Time. According to the explanation for the maximum overshoot, a steady flow field establishes earlier for a higher speed of sound or smaller geometrical dimensions. It is noteworthy that the settling time can be reduced by a factor of 2 to 3 compared to the blunt sensor housings in Fig. 12.

Steady Value. As already sketched in Fig. 1, the flow in front of a conical sensor decelerates to a stagnation point and subsequently accelerates to the corner of the sensor (or housing) front, where the flow speed reaches Mach number $M = 1$ for transonic flows. Simulations are performed to confirm and illustrate this behavior for both sensor holder geometries (see Fig. 30). In the case of the blunt holder (first row), the pressure in front of the sensor surface (shadowed block) is close to stagnation conditions. Conversely, for the conical holder, the flow acceleration and the associated pressure drop occur at the outer part of the sensor surface. Consequently, the measured signal representing an area-averaged pressure over the sensor surface is lower than the stagnation pressure. This effect of the conical holders on the stagnation pressure measurement agrees very well with the experimentally observed deviation of 6%.

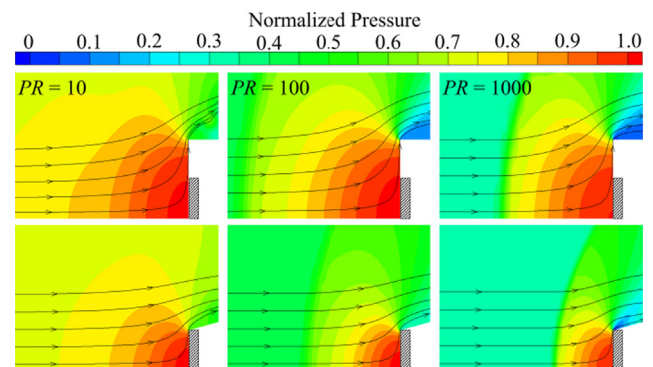


Fig. 30. Pressure contours of the steady-state flow fields around the blunt (top) and conical (bottom) holders at different flow conditions. The shadowed blocks represent the sensor tips.

4. Conclusions

In the present work, the effect of the sensor housing geometries on the stagnation pressure measurement of shock-induced flows is investigated. Housings with two different exterior shapes (blunt and conical) and variations of the internal dimensions (the borehole diameter and the cavity depth) were considered. Each configuration was evaluated at three experimental conditions representing subsonic, transonic and supersonic flows. Influences of other practical factors including the mounting misalignment, the filling with gelatin and the direct exposure of the sensor surface were also assessed. The main points are summarized here:

- (1) The blunt housing consistently gives a shorter rise time, a lower maximum overshoot, weaker oscillations and a shorter settling time than the conical housing, mainly due to the built-in advantage of a shorter borehole length.
- (2) Decreasing the volume ratio between the cavity and the borehole, either by increasing the borehole diameter or reducing the cavity depth, enhances the strength of the reflected shock at the sensor surface. As a result, the signal rise time is shortened and the overshoot is intensified.
- (3) At higher flow Mach numbers, faster wave motions lead to signals oscillating at higher frequencies. The accompanying decrease in the Reynolds number dampens the oscillation amplitudes and shortens the settling time.
- (4) The 2° mounting misalignment decreases the pressure measurement by 2–4%. The conical housing is more sensitive to the misalignment than the blunt one.
- (5) Filling the housing void with gelatin shortens the rise time, but significantly intensifies the overshoot. This design brings little benefit to the pressure measurement in the current setup.
- (6) Experiments with exposed sensors show that the conical sensor holder measures a pressure 6% lower than the stagnation value. Such a deviation is not observed for housings with boreholes and cavities.

To sum up, the blunt housing outperforms the conical one for the stagnation pressure measurement in impulse facilities, by generating less intensely overshooting and more rapidly settled pressure signals. Signal overshoots could be avoided with no sacrifice in the settling time by choosing the borehole diameter and the cavity depth properly. However, the conical housing retains the advantage of less influence on the surrounding flow, and the application of either housing geometry should be case-specific.

Declaration of Competing Interest

There is no financial or personal relationship between authors and other people or organizations that could inappropriately influence or bias the work.

Acknowledgements

The authors acknowledge funding by the European Research Council (ERC) under the European Union's Horizon 2020 research and innovation program (grant agreement No. 667483). The author Z. Wang would like to acknowledge the support from the China Scholarship Council (No. 201606230220).

References

- [1] Rex Klopfenstein Jr., Air velocity and flow measurement using a Pitot tube, *ISA transactions* 37, no. 4 (1998) 257–263.
- [2] A.J. Cable, R.N. Cox, *The Ludwieg pressure-tube supersonic wind tunnel*, *Aeronaut. Quart.* 14 (2) (1963) 143–157.
- [3] Aeronautical Research Council, *Bow-shock establishment and stagnation-point pressure measurements for a blunt-nosed body at supersonic speeds*, HM Stationery Office, 1965.
- [4] J.D. Anderson, *Modern Compressible Flow with Historical Perspective*, 2003.
- [5] Richard Gilman Folsom, *Review of the Pitot tube*, 1955.
- [6] S.H. Chue, *Pressure probes for fluid measurement*, *Progr. Aerospace Sci.* 16 (2) (1975) 147–223.
- [7] C.R. Gossweiler, *On probes and measuring techniques for fast-response flow measurement using piezo-resistive pressure transducers* (1995) 0953–0953.
- [8] R.M. Lec, *Piezoelectric sensors*, *J. Acoust. Soc. Am.* 104 (3) (1998) 1796–1796.
- [9] G. Gautschi, *Piezoelectric sensors, Piezoelectric Sensorics*, Springer, Berlin, Heidelberg, 2002, pp. 73–91.
- [10] A.J. Neely, R.J. Stalker, A. Paull, *High enthalpy, hypervelocity flows of air and argon in an expansion tube*, *Aeronaut. J.* 95 (946) (1991) 175–186.
- [11] A. Paull, R.J. Stalker, *Test flow disturbances in an expansion tube*, *J. Fluid Mech.* 245 (1992) 493–521.
- [12] Akihiro Sasoh, Yasuyuki Ohnishi, Djameel Ramjaun, Kazuyoshi Takayama, Hirotaoka Otsu, Takashi Abe, *Effective test time evaluation in high-enthalpy expansion tube*, *AIAA J.* 39 (11) (2001) 2141–2147.
- [13] Matthew McGilvray, Peter A. Jacobs, Richard G. Morgan, Rowan J. Gollan, Carolyn M. Jacobs, *Helmholtz resonance of pitot pressure measurements in impulsive hypersonic test facilities*, *AIAA J.* 47 (10) (2009) 2430–2439.
- [14] M.A. Sutcliffe, R.G. Morgan, *The measurement of Pitot pressure in high enthalpy expansion tubes*, *Measur. Sci. Technol.* 12 (3) (2001) 327.
- [15] J.W. Naughton, L.N. Cattafesta III, G.S. Settles, *Miniature, fast-response five-hole conical probe for supersonic flowfield measurements*, *AIAA J.* 31 (3) (1993) 453–458.
- [16] A.R. Porro, *Pressure probe designs for dynamic pressure measurements in a supersonic flow field*, in: *Instrumentation in Aerospace Simulation Facilities*, 2001. 19th International Congress on ICASF 2001, IEEE, 2001, pp. 417–426.
- [17] M.K. Bull, A.S.W. Thomas, *High frequency wall-pressure fluctuations in turbulent boundary layers*, *Phys. Fluids* 19 (4) (1976) 597–599.
- [18] A.D. Tomos, R.A. Leigh, *The pressure probe: a versatile tool in plant cell physiology*, *Annu. Rev. Plant Biol.* 50 (1) (1999) 447–472.

A.2 Effect of Mach Number on Droplet Aerobreakup in Shear Stripping Regime

Zhaoguang Wang, Marcus Giglmaier, Thomas Hopfes, Nikolaus A. Adams

In: *Experiments in Fluids* 61.9 (2020), pp. 1-17.

<https://doi.org/10.1007/s00348-020-03026-1>.

Contribution: My contributions to this publication included designing the experimental methodology and carrying out the experiments. I verified the experimental methods and analyzed the data by adapting post-processing tools. The original manuscript was written by me.

Effect of Mach number on droplet aerobreakup in shear stripping regime

SPRINGER NATURE**Author:** Zhaoguang Wang et al**Publication:** Experiments in Fluids**Publisher:** Springer Nature**Date:** Aug 9, 2020*Copyright © 2020, The Author(s)*

Creative Commons

This is an open access article distributed under the terms of the [Creative Commons CC BY](#) license, which permits unrestricted use, distribution, and reproduction in any medium, provided the original work is properly cited.

You are not required to obtain permission to reuse this article.

To request permission for a type of use not listed, please contact [Springer Nature](#)

Permissions

Get permission to reuse Springer Nature content

Springer Nature is partnered with the Copyright Clearance Center to meet our customers' licensing and permissions needs.

Copyright Clearance Center's RightsLink® service makes it faster and easier to secure permission for the reuse of Springer Nature content to be published, for example, in a journal/magazine, book/textbook, coursepack, thesis/dissertation, annual report, newspaper, training materials, presentation/slide kit, promotional material, etc.

Simply visit [SpringerLink](#) and locate the desired content;

Go to the article or chapter page you wish to reuse content from. (Note: permissions are granted on the article or chapter level, not on the book or journal level). Scroll to the bottom of the page, or locate via the side bar, the "Reprints and Permissions" link at the end of the chapter or article.

Select the way you would like to reuse the content;

Complete the form with details on your intended reuse. Please be as complete and specific as possible so as not to delay your permission request;

Create an account if you haven't already. A RightsLink account is different than a SpringerLink account, and is necessary to receive a licence regardless of the permission fee. You will receive your licence via the email attached to your RightsLink receipt;

Accept the terms and conditions and you're done!

For questions about using the RightsLink service, please contact Customer Support at Copyright Clearance Center via phone +1-855-239-3415 or +1-978-646-2777 or email springernaturesupport@copyright.com.

How to obtain permission to reuse Springer Nature content not available online on SpringerLink

Requests for permission to reuse content (e.g. figure or table, abstract, text excerpts) from Springer Nature publications currently not available online must be submitted in writing. Please be as detailed and specific as possible about what, where, how much, and why you wish to reuse the content.

Your contacts to obtain permission for the reuse of material from:

- books: bookpermissions@springernature.com
- journals: journalpermissions@springernature.com

Author reuse

Please check the Copyright Transfer Statement (CTS) or Licence to Publish (LTP) that you have signed with Springer Nature to find further information about the reuse of your content.

Authors have the right to reuse their article's Version of Record, in whole or in part, in their own thesis. Additionally, they may reproduce and make available their thesis, including Springer Nature content, as required by their awarding academic institution. Authors must properly cite the published article in their thesis according to current citation standards.

Material from: 'AUTHOR, TITLE, JOURNAL TITLE, published [YEAR], [publisher - as it appears on our copyright page]'

If you are any doubt about whether your intended re-use is covered, please contact journalpermissions@springernature.com for confirmation.

Self-Archiving

- Journal authors retain the right to self-archive the final accepted version of their manuscript. Please see our self-archiving policy for full details:

<https://www.springer.com/gp/open-access/authors-rights/self-archiving-policy/2124>

- Book authors please refer to the information on this link:

<https://www.springer.com/gp/open-access/publication-policies/self-archiving-policy>



Effect of Mach number on droplet aerobreakup in shear stripping regime

Zhaoguang Wang¹ · Thomas Hopfes¹ · Marcus Giglmaier¹ · Nikolaus A. Adams¹

Received: 20 April 2020 / Revised: 27 July 2020 / Accepted: 28 July 2020 / Published online: 9 August 2020
© The Author(s) 2020

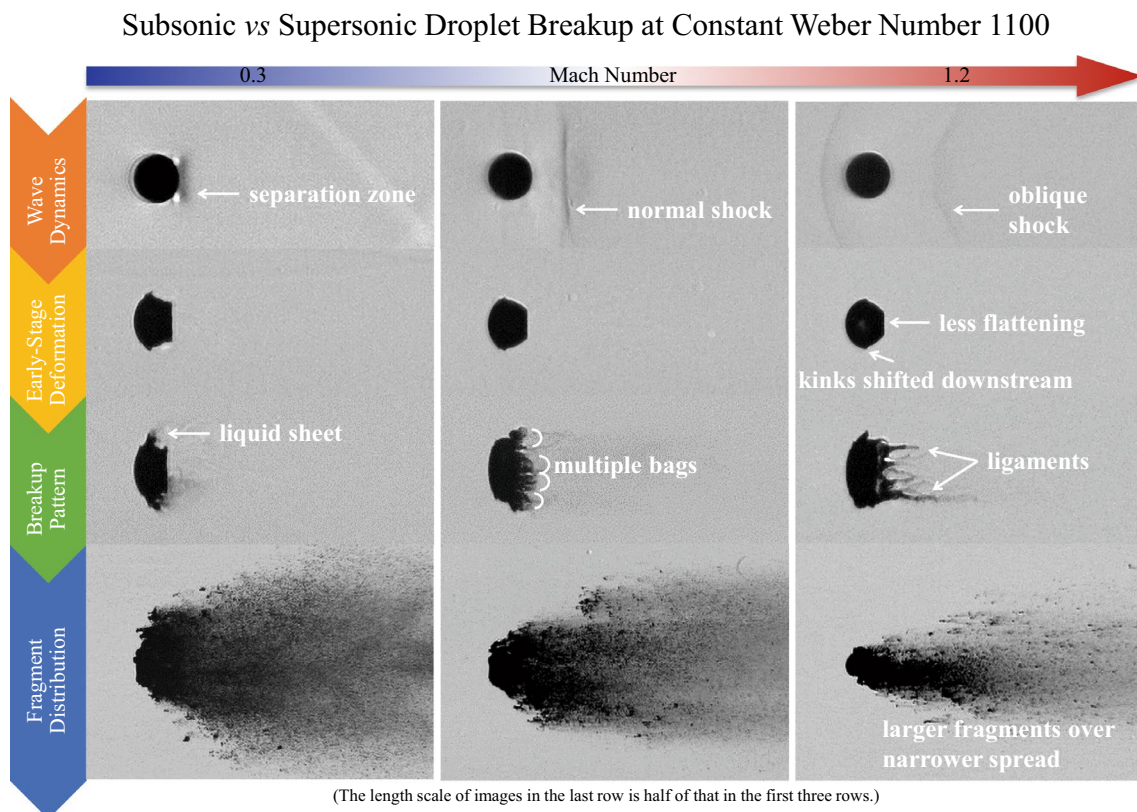
Abstract

The present experimental study investigates the shear stripping breakup of single droplets in subsonic and supersonic gaseous flows. In contrast to most research that places emphasis on the Weber number (We), we focus on the individual effects exerted by flow Mach (M_∞) and Reynolds numbers (Re). Millimeter-sized droplets made of either ethylene glycol or water are exposed to shock-induced flows. Shadowgraph and schlieren images of the breakup process are recorded by an ultra-high-speed camera. The experimental We is constrained at 1100, while M_∞ is varied from 0.3 to 1.19 and Re from 2600 to 24,000. A systematic analysis of the experiment series reveals that the breakup pattern alters with M_∞ although a constant We is maintained. The classical stripping behavior with fine mist shed from the peripheral sheet changes to rupture of multiple bags along the periphery at $M_\infty = 0.63$, and further to stretching of ligament structures from the leeward surface at $M_\infty = 1.19$. The corresponding breakup initiation is delayed and the resultant fragments are sized less uniformly and distributed over a narrower spread. In terms of the early-stage deformation, droplets experience less intense flattening and slower sheet growth at higher M_∞ . The change of Re introduces additional variations, but only to a minor extent.

✉ Zhaoguang Wang
zg.wang@tum.de

¹ Chair of Aerodynamics and Fluid Mechanics, Technical University of Munich, 85748 Garching, Germany

Graphical abstract



1 Introduction

Droplet breakup, also termed secondary atomization, refers to the fragmentation of a droplet subjected to aerodynamic forces. This phenomenon is relevant in diverse applications, such as fuel injection (Reitz and Diwakar 1986), spray coatings (Mostaghimi et al. 2002) and metal powder production (Lagutkin et al. 2004). It has been widely recognized that the breakup morphology is primarily determined by the Weber number (We) and the Ohnesorge number (Oh) (Lane 1951; Hinze 1955):

$$We = \rho_g u_g^2 d_0 / \sigma \quad (1)$$

$$Oh = \mu_d / \sqrt{\rho_d d_0 \sigma}, \quad (2)$$

where ρ_g and u_g are the density and the velocity of the gas flow, and d_0 , σ , μ_d and ρ_d are the initial diameter, the surface tension, the dynamic viscosity and the density of the liquid droplet, respectively. The Weber number represents the ratio between the disruptive aerodynamic force and the restorative surface tension, and the Ohnesorge number compares

the viscous force to the surface tension. According to Guildenbecher et al. (2009), the influence of liquid viscosity on the breakup regime diminishes when Oh drops below 0.1, leaving We as the dominant factor.

Several breakup mechanisms have been identified in the literature and are classified as bag breakup at $11 < We < 35$ and stripping breakup at $We > 80$, with so-called multi-mode breakup in the intermediate range (Hsiang and Faeth 1995; Schmehl 2003). The bag breakup is conventionally understood as a result of the Rayleigh–Taylor instability developed at the droplet front (Joseph et al. 1999). However, some studies suggest different physical mechanisms, including the pressure imbalance between the front and rear side (Opfer et al. 2014), the stress repartition around the surface (Villermaux and Bossa 2009) and the structure of flow vortices in the wake (Inamura et al. 2009). The cause of the stripping breakup is also under debate. No agreement has been achieved on whether the viscous shear or the aerodynamic drag is the driving force. Correspondingly, the name of this regime varies among shear stripping (Ranger and Nicholls 1969), sheet thinning (Liu and Reitz 1997) and shear-induced entrainment (Theofanous and Li 2008). For

the current work, we focus on the stripping breakup and adopt the concept proposed by Theofanous and Li (2008).

Although the breakup mechanism is mainly governed by the Weber number, other non-dimensional parameters influence the breakup behavior as well. Chou et al. (1997) conduct experiments with Ohnesorge numbers below 0.1, and observe larger micro-drops generated at higher Oh. Pilch and Erdman (1987) analyze the effect of Oh on the breakup time and conclude a consistent postponement of the breakup initiation as Oh increases. Lee and Reitz (2000) experimentally show that the liquid–gas density ratio ($\varepsilon = \rho_d/\rho_g$) exerts negligible effects on the breakup process at values higher than 100. In numerical simulations by Kékesi et al. (2014); however, new breakup patterns appear for density ratios below 100. In terms of the flow Reynolds number ($Re = \rho_g u_g d_0/\mu_g$), the work of Liu and Reitz (1997) indicates that the breakup behavior is independent of Re when $Re > 500$. The dependence becomes important only in the Stokes flow (Aalburg et al. 2003) and in liquid–liquid breakup systems (Hsiang and Faeth 1995).

Another non-dimensional parameter, which is of significance but not fully explored, is the flow Mach number M_∞ . Most of preceding experiments are conducted at subsonic conditions, where the effect of the flow compressibility is marginal. However, with the recent development of supersonic combustion systems including pulse detonation engines (Kailasanath 2003), scramjet engines (Curran 2001) and supersonic gas atomizers (Anderson et al. 1991), droplet breakup in high-speed flows becomes of increasing importance. Dinh et al. (2003) and Theofanous et al. (2004) investigate various breakup regimes in a highly rarified flow at $M_\infty = 3$. They find that the morphologies differ significantly from those categorized in subsonic flows and attribute the differences to changes in pressure fields. Ortiz et al. (2004) measure the drag coefficients of droplets in different airstreams and observe a rapid increase as the flow Mach number approaches supersonic conditions. Xiao et al. (2017) numerically simulate the deformation of droplets exposed to supersonic flows and conclude that the onset of breakup is

postponed compared to subsonic cases. Igra and Takayama (2003) and Meng and Colonius (2015) conduct experimental and numerical research on water column breakup in high-speed flows, respectively. Both works quantitatively show a slower temporal increase of the cross-stream diameter at higher M_∞ .

Although the abovementioned research reveals distinct breakup features in supersonic flows, the experimental database addressing the effect of M_∞ is rather limited. Moreover, a change of M_∞ in experiments is commonly accompanied with a change of Re, which renders the independent investigation of M_∞ difficult. In the present work, we constrain the Weber number at 1100 and decouple the correlation between M_∞ and Re by applying different liquid–gas combinations and carefully choosing operating conditions. This creates a test matrix which allows us to study the effects of M_∞ and Re individually.

2 Experimental setup

The layout of the shock tube used for the current experiments is depicted in Fig. 1. The tube, which has an overall length of 24 m and an inner diameter of 290 mm, consists of three segments: the driver, the driven and the test sections. A cookie cutter is installed in front of the test section to remove the boundary flows and to contract the cross section to a $190 \times 190 \text{ mm}^2$ square. In the experiments, a 0.15 mm-thick Mylar diaphragm is placed between the driver and driven sections and in contact with a pair of 0.1 mm-thick crossed NiCr heating wires. Each section of the shock tube is first filled to pressure levels corresponding to desired flow conditions. Then, a single droplet is produced in the test section by expelling liquids through a hypodermic needle with an outer diameter of 0.9 mm. The droplet falls through a pair of aligned laser emitter and receiver. This triggers the rupture of the Mylar diaphragm by supplying an electric current of 3 A to the heating wires. Subsequently, a planar shock wave

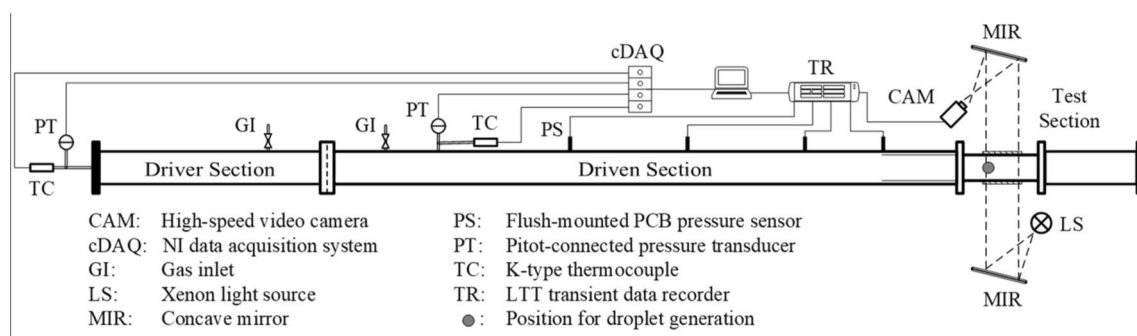


Fig. 1 Layout of the shock tube and the measurement system

forms, propagates towards the downstream test section and induces a flow with uniform flow conditions.

The pressure variation along the shock tube is measured by flush-mounted PCB Piezotronics ICP® fast-response pressure sensors. The measured signals are acquired by a LTT transient data recorder at a sampling frequency of 1 MHz. We calculate the shock velocity based on the time lag between moments when the incident shock passes two pressure sensors ahead of the test section. The combination of the shock velocity and initial pre-shock conditions yields post-shock flow properties based on moving shock relations. Another sensor in the test section measures the pressure rise across the incident shock. A representative pressure signal normalized against the theoretical post-shock pressure is provided in Fig. 2. The shock-induced freestream remains steady over 1.6 ms which well covers the investigated period of droplet breakup (maximally 1.4 ms). The slight decline in the pressure signal is attributed to the growth of the boundary layer as well as the nature of the piezoelectric sensors. This pressure signal also serves as a trigger for the image recording.

As for the flow visualization, a Shimadzu HyperVision HPV-X ultra-high-speed camera is integrated in a Z-type shadowgraph/schlieren photography system. The camera records 128 consecutive images with a resolution of 0.087 mm/pixel at a framing rate of 100 kfps.

For the present experiments, the combinations of two liquids (ethylene glycol and water) and two gases (air and CO₂) are exploited to analyze the effects of M_∞ and Re independently at a constant We. The Weber number, which is constrained at 1100 with a standard deviation of 50, lies within the stripping breakup regime and allows a wide variation of M_∞ and Re. Figure 3 shows the inversely proportional correlation between M_∞ and Re for different liquid–gas combinations. The eight labelled points represent the operating conditions selected for current experiments, and the associated error bars (magnified twice in the plot) stand for the ranges of M_∞ and Re from repeated experiments. The eight

operating conditions are numbered as i,j , where the values of i and j correspond to the relative magnitudes of M_∞ and Re, respectively. Detailed parameters averaged from repeated experiments at each operating condition are summarized in Table 1.

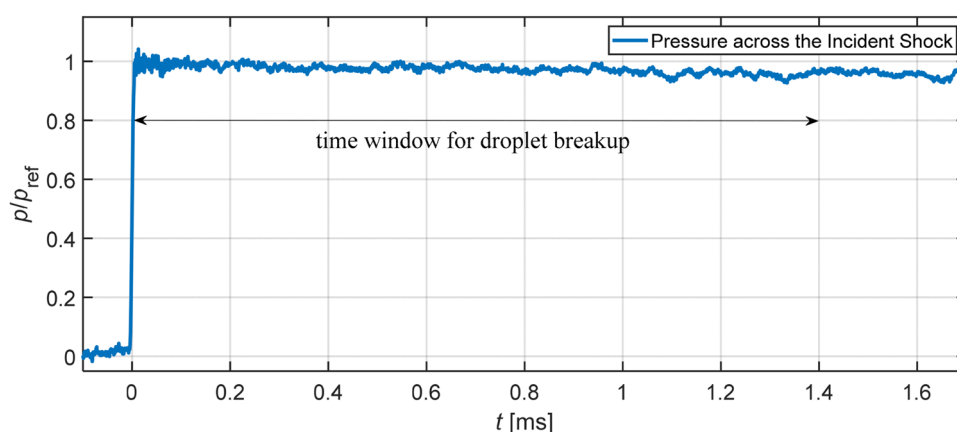
For water ($\rho_d = 998 \text{ kg/m}^3$, $\sigma = 7.28\text{e-}2 \text{ N/m}$, $\mu_d = 8.9\text{e-}4 \text{ kg/m s}$), the average droplet diameter is 3.1 mm, resulting in an Oh of 0.002. For ethylene glycol ($\rho_d = 1113 \text{ kg/m}^3$, $\sigma = 4.73\text{e-}2 \text{ N/m}$, $\mu_d = 1.61\text{e-}2 \text{ kg/m s}$), the lower surface tension leads to smaller droplets with an average diameter of 2.6 mm and the considerably higher viscosity yields an Oh of 0.043. Concerning all the experiments, the freestream Mach number M_∞ varies from subsonic (0.3) to supersonic (1.19) levels and the droplet diameter-based flow Reynolds number Re ranges over an order of magnitude (from 2.6e3 to 2.4e4). The liquid–gas density and viscosity ratios are also provided in Table 1 for completeness.

Case 1.4, 2.3, 3.2 and 5.1 are conducted with the same liquid and gas. Comparisons between them highlight the overall influences of parameters other than We and Oh. Moreover, Case 2.3, 4.3 and 5.3 have comparable Re but different M_∞ , while Case 5.1, 5.2, and 5.3 share the same M_∞ but changing Re. Comparisons of the former and of the latter group shed light on the individual role played by M_∞ and Re, respectively.

3 Results and discussion

A brief overview of the typical stripping breakup process in subsonic flows (Case 1.4, $M_\infty = 0.3$, liquid: ethylene glycol, gas: air) is provided in Fig. 4. Here, the experimental time t is regarded as zero at the moment when the incident shock impacts on the droplet. Furthermore, t is normalized against the characteristic transport time derived by Ranger and Nicholls (1969) based on droplet deformation in incompressible flows, yielding the dimensionless time T as

Fig. 2 Step-wise pressure rise across the incident shock measured in the test section



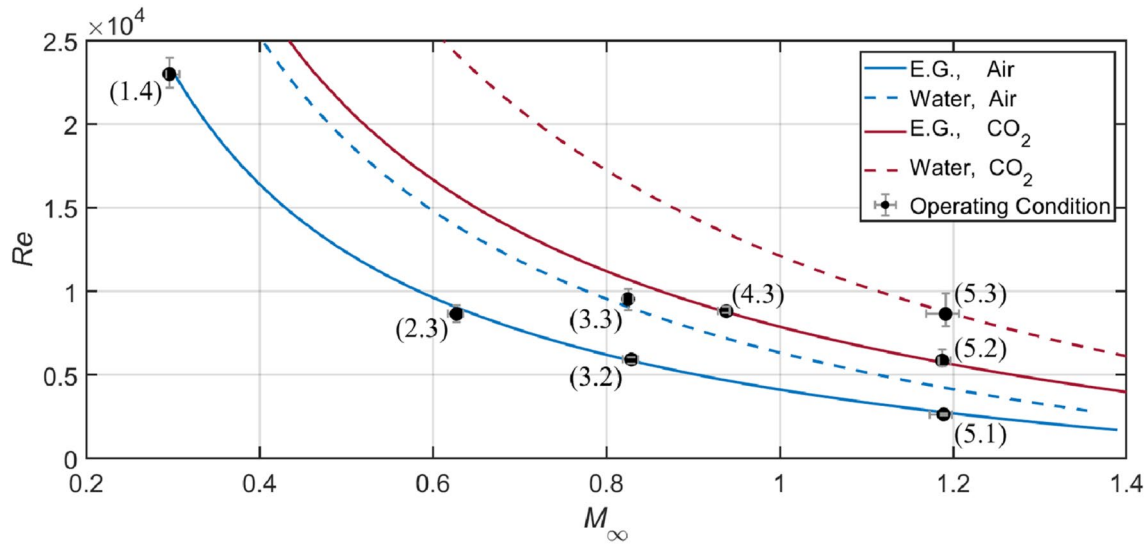


Fig. 3 Inversely proportional correlation between M_∞ and Re at $We=1100$. Each line corresponds to a certain liquid–gas combination. The eight operating conditions are labeled as $i-j$, with i and j

representing the relative magnitudes of M_∞ and Re respectively. The associated error bars stand for the ranges of conditions from repeated experiments and are magnified twice in the plot for a clearer display

Table 1 Operating conditions averaged from repeated experiments

	Liquid	Gas	We	Oh	Re	M_∞	$\rho d/\rho_g$	$\mu d/\mu_g$
Case 1.4	E.G	Air	1060	0.042	2.4e4	0.3	7.1e2	796
Case 2.3	E.G	Air	1056	0.044	8.6e3	0.63	3.6e3	697
Case 3.2	E.G	Air	1120	0.043	5.9e3	0.83	7.1e3	635
Case 5.1	E.G	Air	1050	0.044	2.6e3	1.19	2.1e4	508
Case 3.3	Water	Air	1160	0.002	9.5e3	0.83	4.5e3	35
Case 4.3	E.G	CO ₂	1100	0.044	8.8e3	0.94	4.7e3	802
Case 5.2	E.G	CO ₂	1120	0.043	5.9e3	1.19	9.0e3	713
Case 5.3	Water	CO ₂	1080	0.002	8.6e3	1.19	6.1e3	39

$$T = t \cdot u_g / (d_0 \sqrt{\rho_d / \rho_g}), \tag{3}$$

The time scaling in Eq. (3) does not account for the compressibility effects, which govern the droplet breakup in the current study. Nevertheless, this scaling is used to present the results in a consistent and comparable way with previous literature. Presented images are processed with subtraction of the background noise, contrast stretching and super resolution using MATLAB’s Very Deep Super-Resolution convolutional neural network (Kim et al. 2016).

The entire breakup process is divided into four stages. It starts with the shock-droplet interaction which establishes a flow field resembling that around a solid sphere ($T < 0.1$). Then, the droplet is flattened along the streamwise direction ($T = 0.2$) and a liquid sheet emerges at the equator ($T = 0.3$). The rupture of the sheet indicates the breakup initiation ($T = 0.4$) and the coherent body is continuously eroded at

the periphery afterwards. The last stage is achieved when the whole droplet disintegrates into fragments distributed widely in the flow field (out of the time window shown in Fig. 4).

Figure 4 also presents the quantitative change of the droplet cross-stream diameter d_c . The error bar represents the uncertainty (90% confidence level based on the Student’s t -distribution) calculated from four repeated experiments. Before the onset of breakup ($T < 0.37$), the increase of d_c indicates the flattening of the intact body and the associated uncertainty is low. Once the breakup starts, the intact body is shadowed by the fine mist. The interpretation of d_c changes to a description of the spatial distribution of liquid fragments. The corresponding uncertainty significantly increases as micro-drops are more sensitive to local flow disturbance than the coherent body. Considering the uncertainty levels are similar for all cases, the error bars are omitted in the following plots for the sake of brevity.

In following sections, we compare cases with variations in flow Mach and Reynolds numbers with respect to

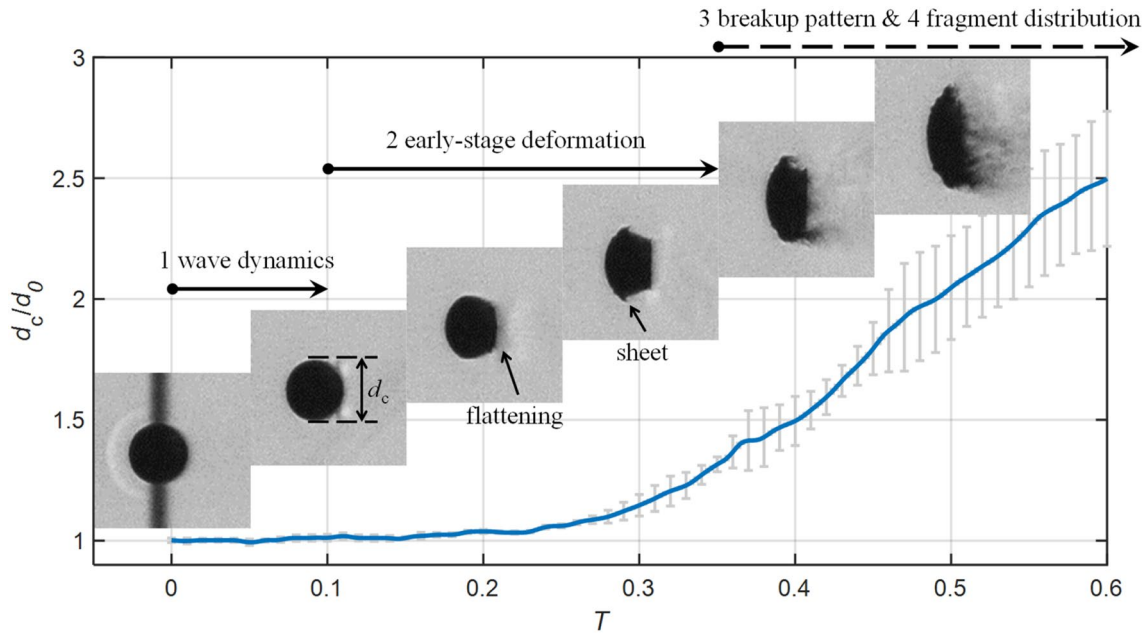


Fig. 4 Breakup patterns and cross-stream diameter variation of an ethylene glycol droplet at $M_\infty=0.3$ (Case 1.4). The error bars represent uncertainties of d_c calculated from four repeated experiments

each stage of the breakup process, namely wave dynamics, early-stage deformation, breakup patterns, and fragment sizes and spatial distributions. The main comparison is made between Case 1.4, 2.3, 3.2 and 5.1 all of which employ the same liquid and gas, to illustrate the overall tendency. This is further complemented by comparisons between constant-Re and constant- M_∞ cases to highlight the individual effects of M_∞ and Re, respectively. The discussion is concluded with a brief analysis of the influence of Oh.

3.1 Wave dynamics

Figure 5 presents a visualization of wave dynamics surrounding ethylene glycol droplets in airstreams after the impact of the incident shock for Case 1.4, 2.3, 3.2 and 5.1. At $M_\infty=0.3$, typical features including the reflected shock (RS) at the windward surface, the diffracted shock (DS) enclosing the droplet and separation zones (SZ) attached at the rear are clearly identified. These characteristics are in good agreement with the experimental and numerical results of water column breakup from Igra and Takayama (2001) and Meng and Colonius (2015).

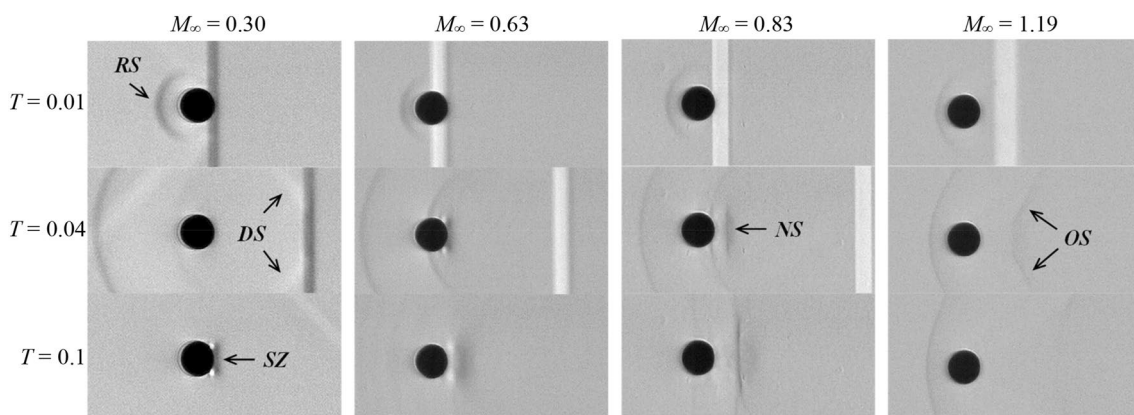


Fig. 5 Wave dynamics around ethylene glycol droplets in air. The operating conditions from left to right are Case 1.4, 2.3, 3.2 and 5.1. *RS* reflected shock, *DS* diffracted shock, *SZ* separation zone, *NS* normal shock, *OS* oblique shock)

The main change at $M_\infty = 0.63$ is that the separation zone behind the droplet extends over a wider region. As the freestream speed enters the transonic range ($M_\infty = 0.83$), a normal shock (NS) appears behind the droplet and fluctuates slightly around the displayed location. This suggests that the surrounding flow accelerates to supersonic conditions as it bypasses the droplet. For the case at $M_\infty = 1.19$, an oblique shock cone (OS) appears, stretching downstream over a broad region. Meanwhile, the reflected shock ahead of the droplet settles as a detached bow shock.

Considering the droplet does not undergo noticeable deformation during the short period of shock-droplet interaction, the surrounding pressure field is expected to resemble that around a solid sphere, which is also implied by the wave patterns presented in Fig. 5. As M_∞ changes, the pressure imposed on the spherical surface differs significantly (Charters and Thomas 1945; Bailey and Haitt 1972). These differences are held accountable for the more pronounced distinctions in succeeding deformation and breakup processes (Hanson et al. 1963).

The travelling velocity of the reflected shock is plotted in Fig. 6 with respect to the position relative to the droplet front. The distance s between the reflected shock and the droplet leading edge is normalized by the droplet diameter d_0 . The Mach number of the reflected shock relative to the freestream flow is calculated as $M_r = (ds/dt + u_g)/a$, where a is the speed of sound in the freestream. For cases with $M_\infty < 1$, the reflected shock decays to sonic waves, and the corresponding M_r falls towards 1. For the supersonic case with $M_\infty = 1.19$, however, the decreasing M_r settles at M_∞ and the normalized distance s/d_0 is stabilized around 0.65 which matches the value measured for a solid sphere at similar conditions (Liepmann and Roshko 2001).

3.2 Early-stage deformation

The early-stage droplet deformation for subsonic and supersonic cases is compared in Fig. 7. As described in Fig. 4,

the droplet at $M_\infty = 0.3$ exhibits typical deformation features such as flattening at frontal and rear surfaces and stretching of the liquid sheet around the equator. Generally, droplets at higher- M_∞ follow similar deformation patterns, but a thorough examination reveals noticeable distinctions that are summarized as follows:

- the liquid sheet emerges further downstream in the supersonic flow ($T=0.20$);
- the flattening of the leeward surface becomes weaker as M_∞ increases ($T=0.30$);
- the liquid sheet grows more rapidly at lower M_∞ ($T=0.48$).

As the windward surface of the droplets gets flattened, kinks form around the droplet equator at $T=0.2$. These kinks are the origins of the subsequent development of liquid sheets. In subsonic flows, the kink is located ahead of the equatorial plane and the angle of inclination of the line connecting the kink to the droplet center is approximately 80° with respect to the flow direction. However, the position of the kink is shifted considerably downstream in the supersonic flow and the corresponding angle of inclination is 92° . The kink locations are in good accordance with the trajectory of the separation point at the surface of a solid sphere measured by Charters and Thomas (1945). In their work, the separation point stays with an angle of inclination between 70° and 80° at subsonic conditions and drifts downstream beyond 90° at $M_\infty = 1.2$.

During the period shown in Fig. 7, the leeward surface of the droplet is continuously flattened. The extent of the flattened area at $T=0.3$ is estimated relative to the initial droplet diameter. As M_∞ increases from 0.3 to 1.19, the corresponding flattened area shrinks from $0.84d_0$ to $0.5d_0$. This could be associated to the change of the pressure imposed on the droplet rear at different flow conditions. Karyagin et al. (1991) experimentally measure the pressure distribution over the surface of a sphere, and observe that the pressure

Fig. 6 Mach number of the reflected shock relative to the freestream flow (M_r) with respect to the normalized distance from the reflected shock to the droplet front (s/d_0) for Case 1.4, 2.3, 3.2, 4.3 and 5.1

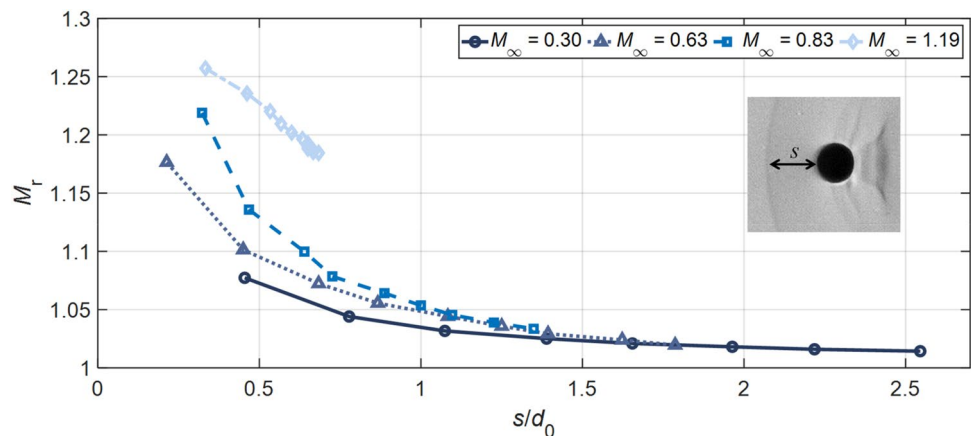
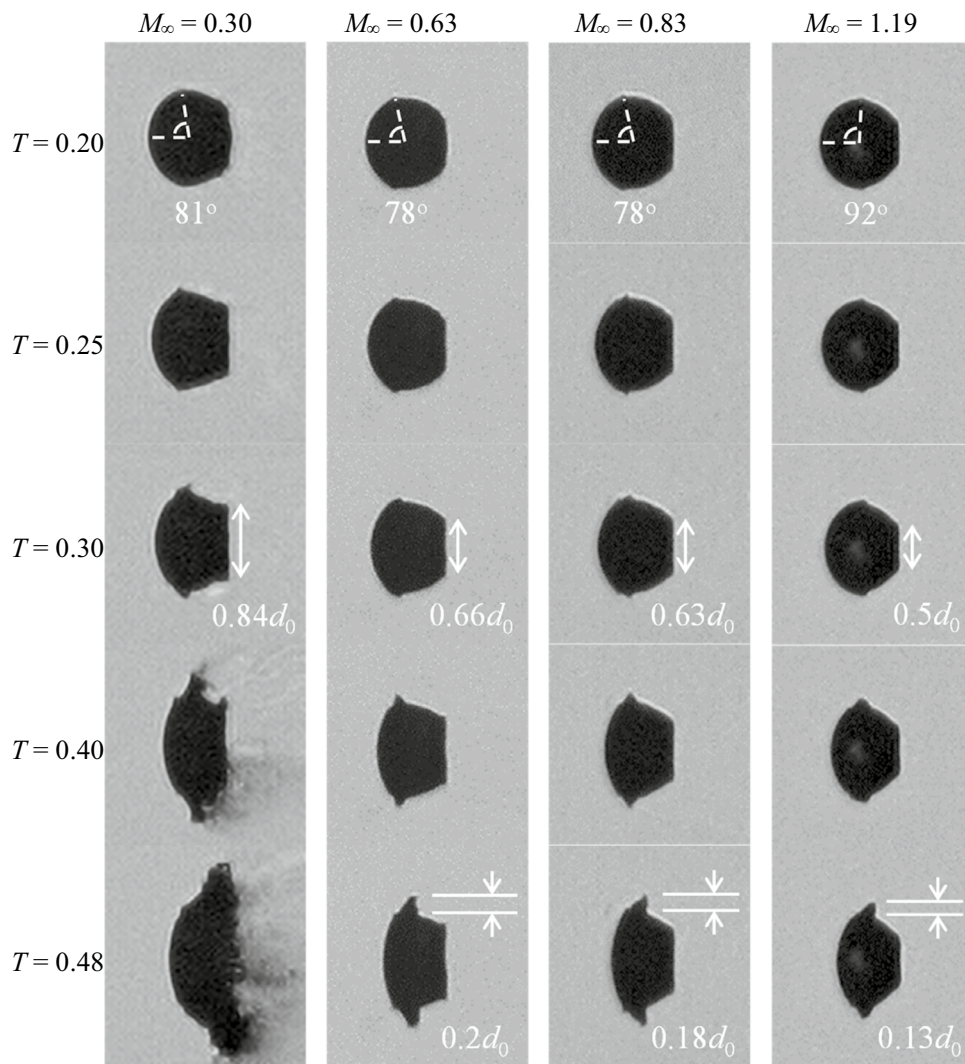


Fig. 7 Droplet flattening and development of liquid sheets (left to right: Case 1.4, 2.3, 3.2 and 5.1)

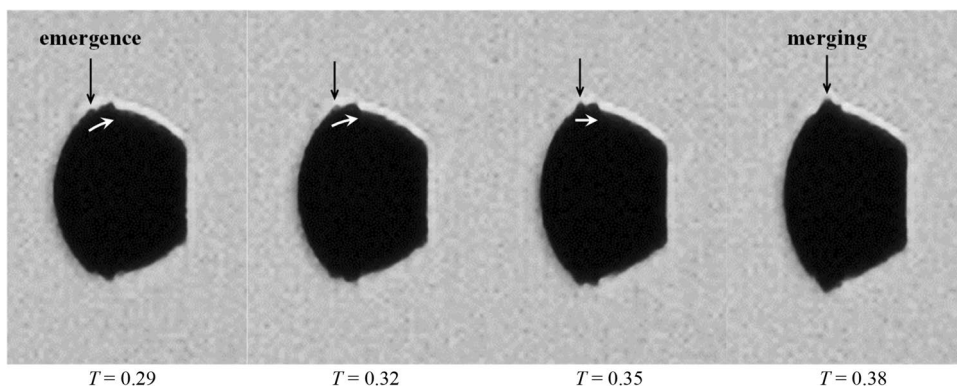


at the rear surface drops consistently as M_∞ increases. The same trend is also reported in the numerical work by Nagata et al. (2016).

By $T=0.48$, the liquid sheets for all cases have grown to considerable sizes and stretched out radially from the main body. Similarly to the experimental observation by

Theofanous et al. (2012) and the numerical analyses by Jalaal and Mehravaran (2014), the growth of the liquid sheets is enhanced by the emergence of propagative waves at the droplet surface, as shown in Fig. 8. These surface waves are induced by Kelvin–Helmholtz instabilities at the windward surface, where the liquid–gas interface suffers

Fig. 8 Emergence, propagation and merging of surface waves at the droplet periphery (Case 3.2, $M_\infty=0.83$). Dark and white arrows indicate locations and movement directions of the surface waves, respectively



strong shear. The waves are transported towards the equator under drag forces and then merge with the preceding waves.

Papamoschou and Roshko (1988) point out that increasing the flow Mach number reduces the growth rate of the shear layer between two streams rapidly, because the associated compressibility effect tends to stabilize the flow disturbance. Moreover, according to Liepmann and Roshko (2001) and Nayfeh and Saric (1971), the pressure distribution around small-scale waves is out of phase with the wave profile in supersonic flows and thus suppresses the development of instabilities. Consequently, the growth rate of the liquid sheet is lower at higher M_∞ . This explains the observation at $T=0.48$ in Fig. 7 that the liquid sheet becomes smaller as M_∞ increases.

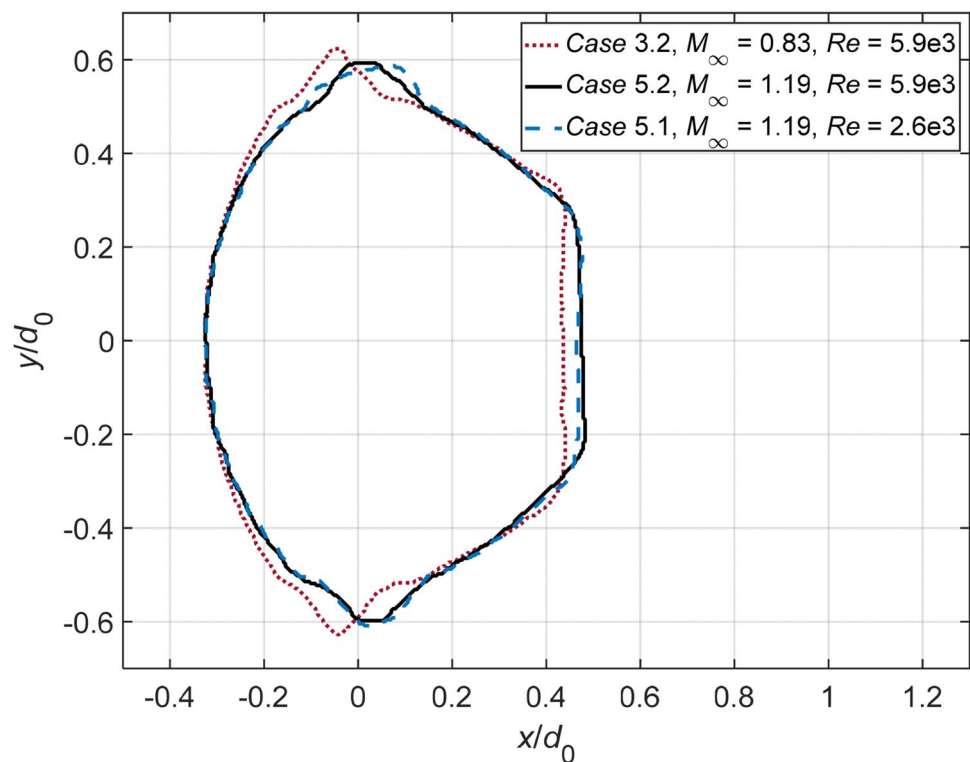
Figure 9 compares the droplet contours at $T=0.4$ between Case 3.2, 5.2 and 5.1. The dimensions are normalized against the initial droplet diameter, and the origin represents the position of the initial droplet center. Case 5.2 has the same M_∞ as Case 5.1, and shares a comparable Re with Case 3.2. The resemblance of the droplet contours between Case 5.2 and Case 5.1 indicates that Re exerts negligible effects on the early-stage deformation, while M_∞ plays a critical role in determining the flattening intensity and the sheet development.

To further quantify the droplet deformation, streamwise displacements of the leading edge, the mass center and the trailing edge are measured. These parameters are of particular interest for numerical validations.

The position of the mass center, which is calculated with the assumption that the droplet cross section normal to the flow direction is axisymmetric, is plotted in Fig. 10. For all cases, the trajectory of the droplet mass center approximates to be parabolic over the shown period. The drag coefficient CD is estimated by fitting the data into the relation $x_{mc}/d_0 = 3/8CDT^2$ derived by Ranger and Nicholls (1969). The subsonic case at $M_\infty=0.3$ experiences a drastic acceleration around $T=0.25$. This results from the rapid growth of the cross-stream diameter, as shown in Fig. 7, and yields a relatively high CD of 1.4. For the other three cases that share comparable cross-stream diameters before $T=0.4$, the streamwise drift of the droplet mass center is faster at higher M_∞ . The corresponding drag coefficients are calculated to be 0.9 for $M_\infty=0.63$, 1.0 for $M_\infty=0.83$ and 1.2 for $M_\infty=1.19$. This trend agrees with the drag coefficients for a solid sphere measured by Bailey and Haïtt (1972) and Charters and Thomas (1945), but the values are much higher due to the droplet flattening.

Figure 11 compares the streamwise displacements of the leading edge and the trailing edge at different flow conditions. It is noteworthy that the difference of the leading edge shift is negligible among all present cases. Therefore, as also stated by Theofanous (2011), the displacement of the leading edge is not a proper parameter to represent the drag. In terms of the trailing edge, the displacement shows certain degrees of variations between cases and becomes smaller at higher M_∞ . This tendency is consistent with the observation

Fig. 9 Droplet outlines of Case 3.2, 5.2 and 5.1 at $T=0.4$. The mass center of the initial droplet lies at (0, 0)



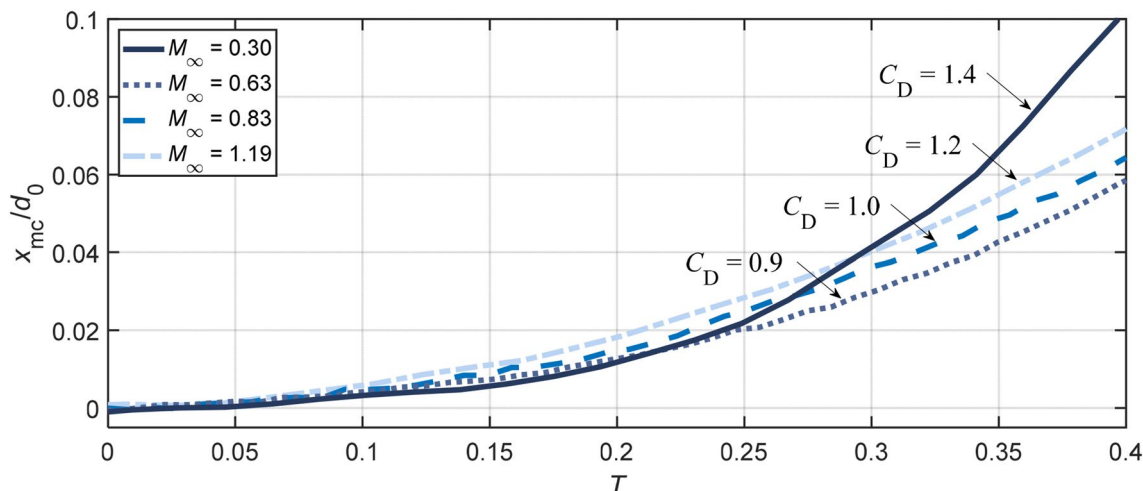
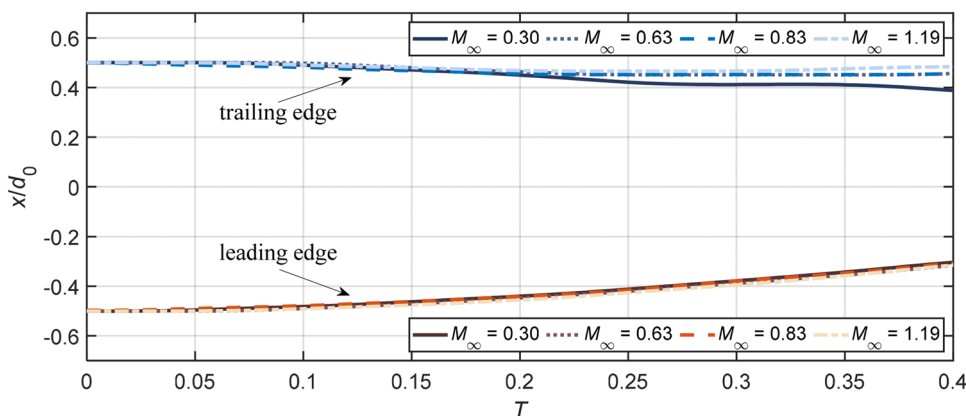


Fig. 10 Streamwise displacement of the mass center for Case 1.4, 2.3, 3.2 and 5.1. Initial droplet center lies at $x=0$. The plotted data are averaged values from four repeated experiments

Fig. 11 Streamwise displacement of the leading edge and the trailing edge for Case 1.4, 2.3, 3.2 and 5.1. Initial droplet center lies at $x=0$. The plotted data are averaged values from four repeated experiments



in Fig. 7 that the flattening at the leeward surface is weakened as M_∞ increases.

3.3 Breakup patterns

Breakup patterns of droplets at different flow conditions are displayed in Fig. 12. The first row represents the individual breakup initiation which is defined as the onset of the formation of liquid fragments. Each of the remaining rows corresponds to a specific time moment. Although the breakup process shows certain degrees of chaotic behavior (Hardalupas and Whitelaw 1994; Engelbert et al. 1995), the features discussed in the following are consistently observed in repeated experiments. Generally speaking, three types of breakup patterns are categorized:

- fragmentation of the liquid sheet ($M_\infty=0.3$);
- development of multiple bags along the periphery ($M_\infty=0.63$);

- formation of streamwise ligaments in the wake ($M_\infty=1.19$).

The droplet at $M_\infty=0.3$ experiences a typical stripping breakup initiated with the fracture of the liquid sheet. Afterwards, the windward surface is continuously flattened and expands over an increasingly broad region. At regions encircling the smooth front, small-scale waves generated by Kelvin–Helmholtz instabilities appear. These waves propagate towards the periphery peeling micro-drops off from the droplet. The micro-drops are entrained in the flow and distributed widely in the cross-stream direction.

The breakup pattern is altered as the flow Mach number increases. At $M_\infty=0.63$, the breakup onset is not indicated by entrainment of micro-drops, but by the formation of multiple bags along the periphery. Figure 13 shows the evolution from the bending of the liquid sheet to the inflation of the multiple bags. As the sheet extends downstream, the peripheral region is straightened to directly face the freestream flow ($T=0.54$). Then, multiple bags form along the rim and

Fig. 12 Droplet breakup patterns (left to right: Case 1.4, 2.3, 3.2, 5.1 and 5.2). The top row corresponds to the breakup initiation

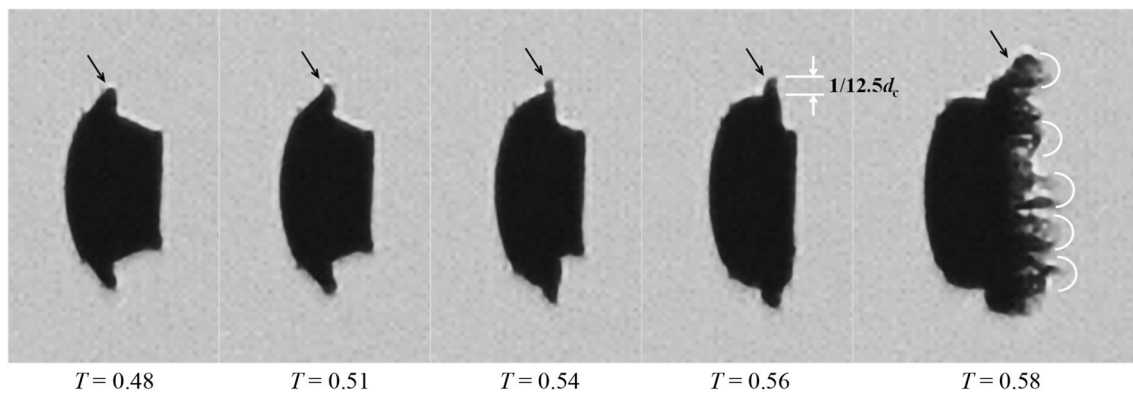
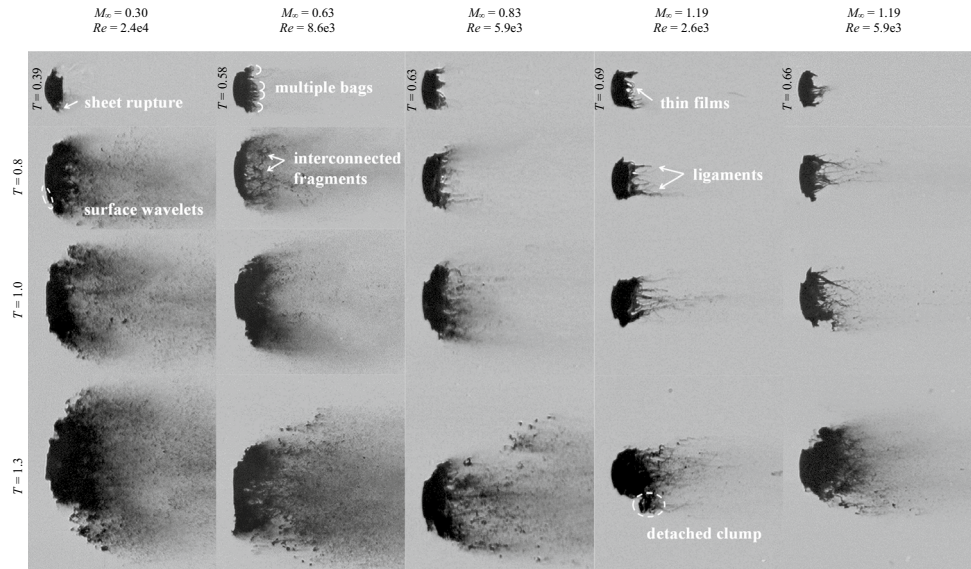


Fig. 13 Straightening of the droplet rim (indicated by the arrows) and formation of multiple bags along the periphery for Case 2.3 at $M_\infty = 0.63$

inflate rapidly ($T=0.59$). These bags rupture into fine mist and the rings that the bags are attached to disintegrate into larger interconnected fragments as indicated at $T=0.8$ in Fig. 12. The remaining coherent body of the droplet deforms into a crescent shape and the succeeding breakup process resembles the typical stripping pattern.

According to Theofanous et al. (2004) and Guildenbecher et al. (2009), the wave number n of the fastest-growing wave induced by Rayleigh–Taylor instabilities at the droplet front can be calculated with the following relation:

$$n = \frac{1}{2\pi} \left(\frac{d_c}{d_0} \right)^2 \sqrt{C_D \cdot We} \tag{4}$$

For Case 2.3 at $T=0.56$, d_c is 1.53 times of the initial diameter d_0 (see Fig. 15) and the average value of C_D is 0.9 (see Fig. 10), which yields $n=11.7$. The actual value of n should be higher considering the real-time C_D is growing over time. Nevertheless, the calculated wave number agrees

well with the observation in Fig. 13 that the straightened edge, where bags develop occupies $1/12.5$ of the entire cross-stream diameter. This implies that the Rayleigh–Taylor instability is the underlying reason for the local bag formation. Similar bag structures are also observed in the numerical simulation of diesel jet breakup at $We = 1270$ by Shinjo and Umemura (2010).

For Case 5.1 at $M_\infty = 1.19$, the droplet breakup is characterized by the generation of long and thin streamwise ligaments in the wake, similarly to the observation by Liu and Reitz (1997). Figure 14 presents the deformation of the liquid sheet which induces the succeeding generation of ligaments. After emerging from the main body, the liquid sheet bends along the flow direction and folds to wrap the droplet rear before the breakup is initiated. The sheet becomes thinner as it stretches and thus is increasingly sensitive to instabilities. According to the study of sheet breakup in co-flow by Stapper and Samuelson (1990), surface instability is mainly caused by the growth of the streamwise vortical

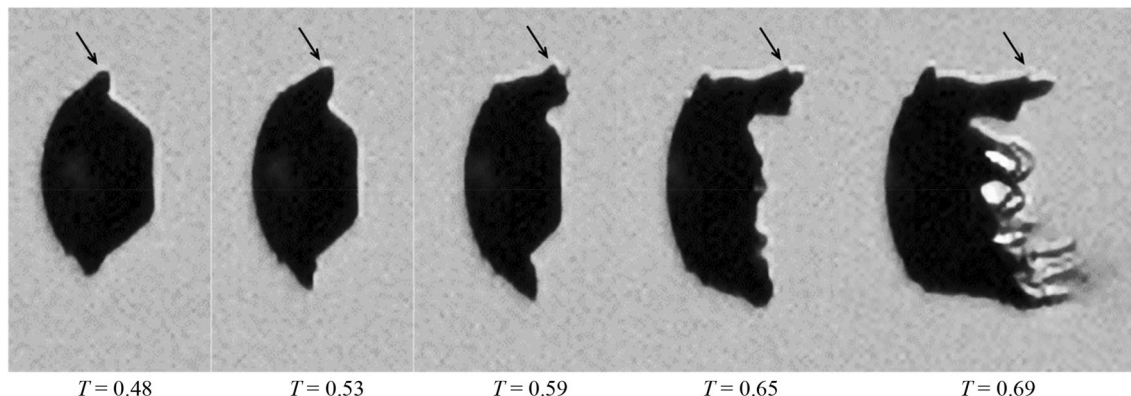
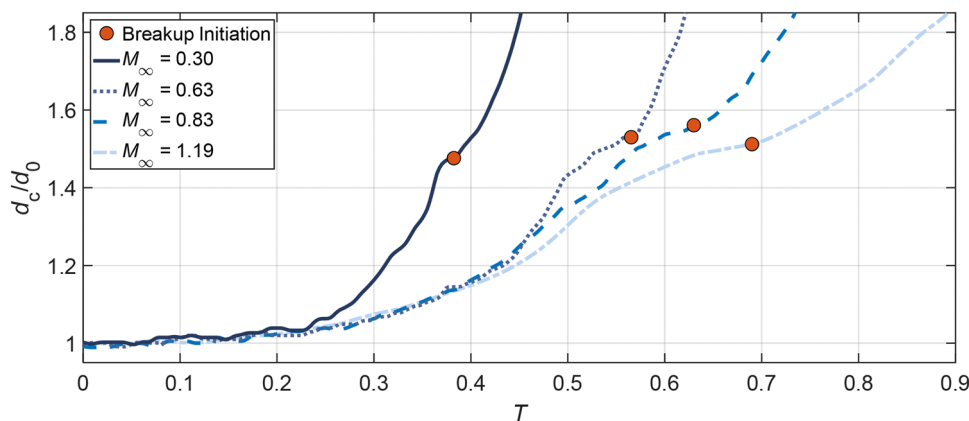


Fig. 14 Folding of the liquid sheet (indicated by the arrows) and generation of ligaments connected by thin membranes for Case 5.1 at $M_\infty = 1.19$

Fig. 15 Variation of the cross-stream diameter for Case 1.4, 2.3, 3.2 and 5.1. The red dots represent the breakup initiation. The plotted data are averaged values from four repeated experiments



waves when the flow velocity is high. As a result, streamwise ligaments connected by thin films are formed ($T=0.69$ in Fig. 12). After the films burst into micro-drops, the ligaments are stretched under the viscous shear of the flow and break into larger fragments in the presence of Rayleigh-Plateau instabilities. The subsequent breakup of the droplet continues in the pattern that new ligaments form and fragment. It is occasionally observed that large liquid clumps ($T=1.3$ in Fig. 12) detach from the intact body and disintegrate separately. It is noteworthy that recent studies (Jalaal and Mehravaran 2014; Meng and Colonius 2018; Biasiori-Poulanges and El-Rabii 2019; Dorschner et al. 2020) propose the mechanism of transverse azimuthal modulation as an alternative explanation for the generation of streamwise ligaments. It is stated that the growth of Kelvin–Helmholtz instabilities near the droplet periphery triggers Rayleigh–Taylor instabilities in the transverse plane which further lead to the formation of ligaments.

The breakup process of Case 5.2 is also presented in Fig. 12. The droplet exhibits few breakup features in common with the identical-Re Case 3.2, but resembles approximately the same characteristics as the identical- M_∞ Case

5.1. A minor difference between Case 5.2 and Case 5.1 is that the former generates slightly thinner ligaments than the latter. This suggests that M_∞ plays a dominant role in determining the breakup patterns, while Re only affects detailed structures.

Figure 15 compares the change of the droplet cross-stream diameter d_c between subsonic and supersonic conditions. Before $T=0.25$, the droplet deformation is characterized by the flattening of the main body. During this stage only marginal differences are identified among all cases. Afterwards the liquid sheet starts to develop, resulting in a rapid growth of d_c . The growth rate is significantly higher for $M_\infty = 0.3$ than the others, which is in accordance with the observation in Fig. 7. Although the differences between high- M_∞ cases (Case 2.3, 3.2 and 5.1) are comparatively small, there exists a consistent tendency that the cross-stream diameter grows more slowly as M_∞ increases. Once the breakup is initiated (marked by the red points in Fig. 15), d_c represents the cross-stream spread of the liquid fragments instead. With the breakup onset as a separating point, the overall d_c profile is divided into two power-law stages. The short-duration plateaus ahead of the breakup initiation correspond to the

periods when the liquid sheet is bent along the flow direction rather than stretched out radially.

For all cases, the breakup begins when the normalized d_c reaches approximately 1.5. The subsonic Case 1.4 at $M_\infty = 0.3$ experiences the earliest breakup, and the corresponding initiation time $T = 0.39$ matches the empirical correlation proposed by Pilch and Erdman (1987). The postponement of the breakup initiation as M_∞ increases is a consequence of the change in the breakup pattern as shown earlier. The fragmentation of multiple bags and the disintegration of streamwise ligaments at high M_∞ need significantly longer time than the direct sheet rupture at low M_∞ .

3.4 Fragment sizes and spatial distributions

In industrial applications that involve atomization processes, the fragment sizes are of particular significance. For instance, small fragments are desired in fuel injections to achieve efficient evaporation and combustion. Figure 16 compares the droplet fragmentation at $T = 2.0$ for Case 1.4, 2.3, 3.2 and 5.1. At this stage, the coherent body is difficult to identify as the windward surface is severely eroded. Droplets break into uniformly fine mist at subsonic conditions,

while the supersonic flow leads to large discrete particles that are scattered among tiny micro-drops. These large particles are mainly caused by the disintegration of ligament structures.

Apart from the size distribution, the spatial spread of the fragments is also of practical importance, since it determines the likelihood of micro-drops coalescing into larger particles. Figures 17, 18 present the outlines of dispersed fragments for various cases at $T = 2.0$. The outlines are extracted with MATLAB[®] based on the modified Moore-Neighbor tracing algorithm (Gonzalez et al. 2004). The differences among Case 2.3, 4.3 and 5.3 (Fig. 17), which share the same Re , indicate that higher M_∞ leads to a narrower cross-stream spread of the fragments. Such an effect could be related to the fact that the windward surface of the droplet is less flattened but more curved at higher M_∞ (see Figs. 7, 12). Correspondingly, the fragments gain lower cross-stream momentum from the gas flow when detaching from the droplet periphery and are hence distributed less widely in the cross-stream direction. The comparison between Case 5.1, 5.2 and 5.3 (Fig. 18), which share an identical M_∞ , shows that lowering Re also tends to constrain the spatial distribution of the fragments, but much less effectively than increasing M_∞ .

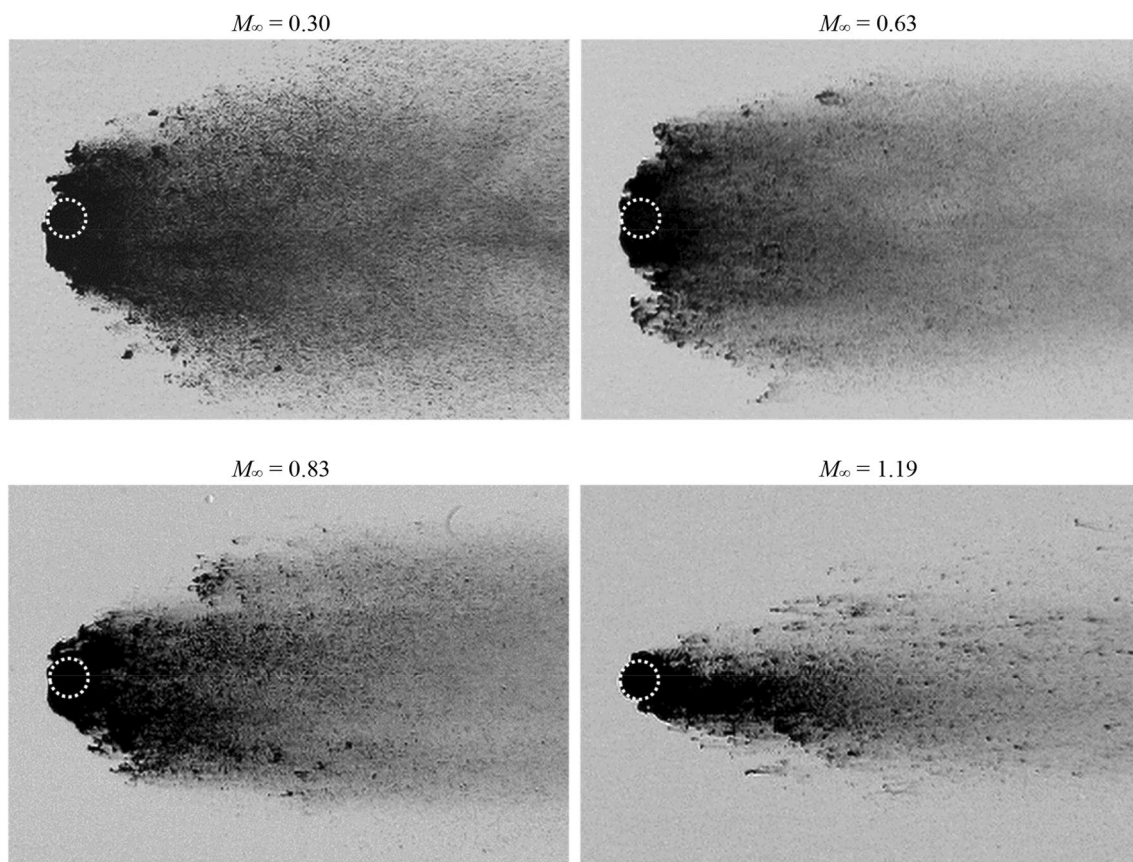


Fig. 16 Spatial distributions of liquid fragments at $T = 2.0$ for Case 1.4, 2.3, 3.2 and 5.1. The white circles represent the initial droplet sizes

Fig. 17 Comparison of fragment spreads at $T=2.0$ between Case 2.3, 4.3 and 5.3. For all cases, Re is approximately $8.6e3$

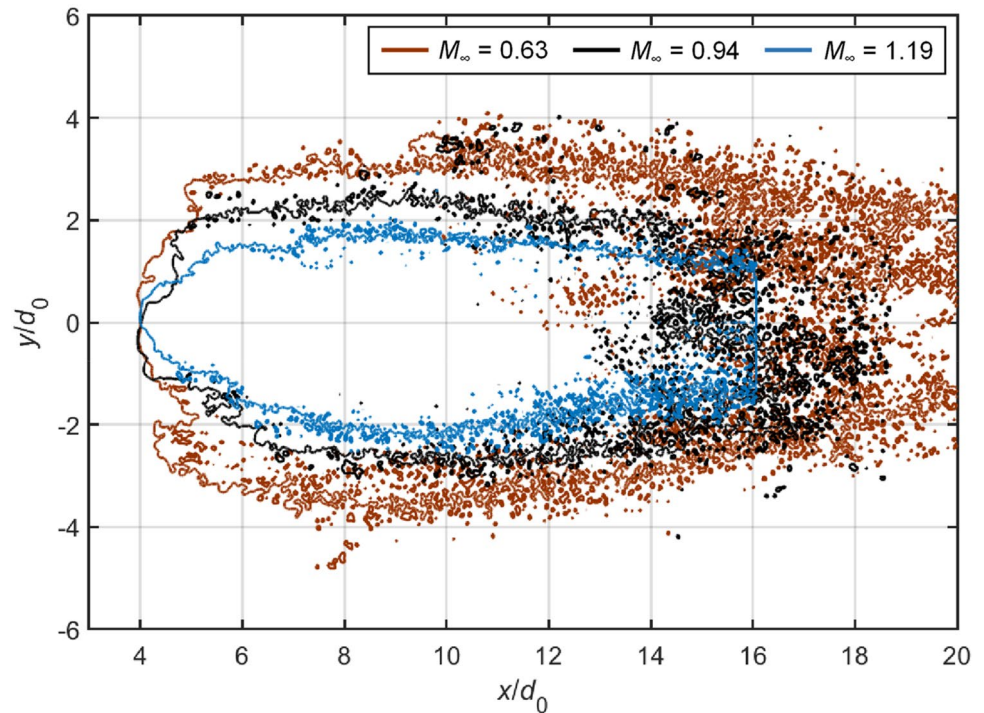
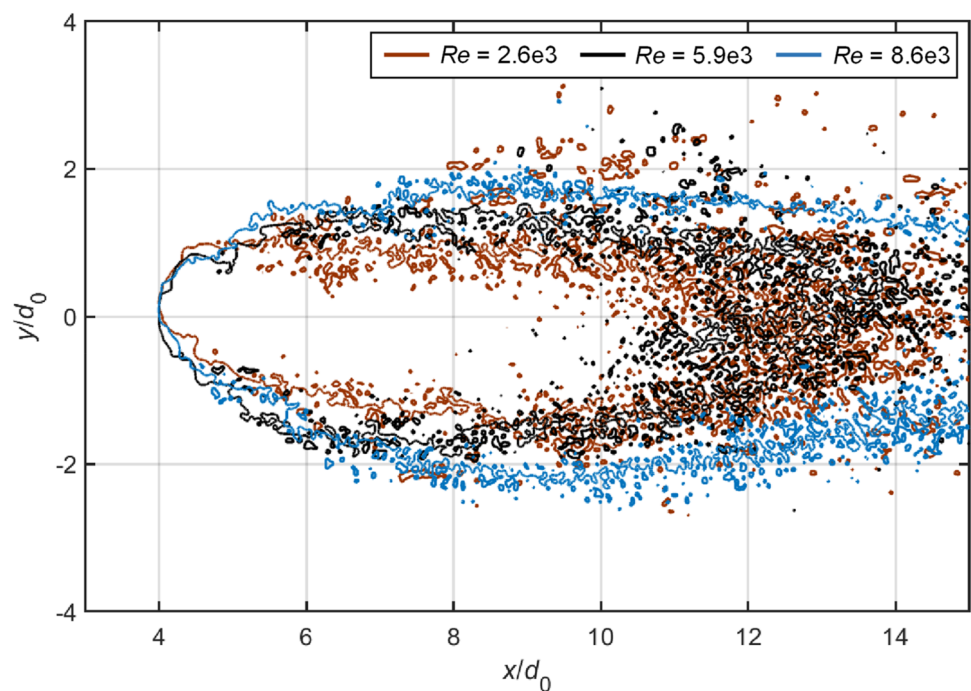


Fig. 18 Comparison of fragment spreads at $T=2.0$ between Case 5.1, 5.2 and 5.3. For all cases, M_∞ equals to 1.19

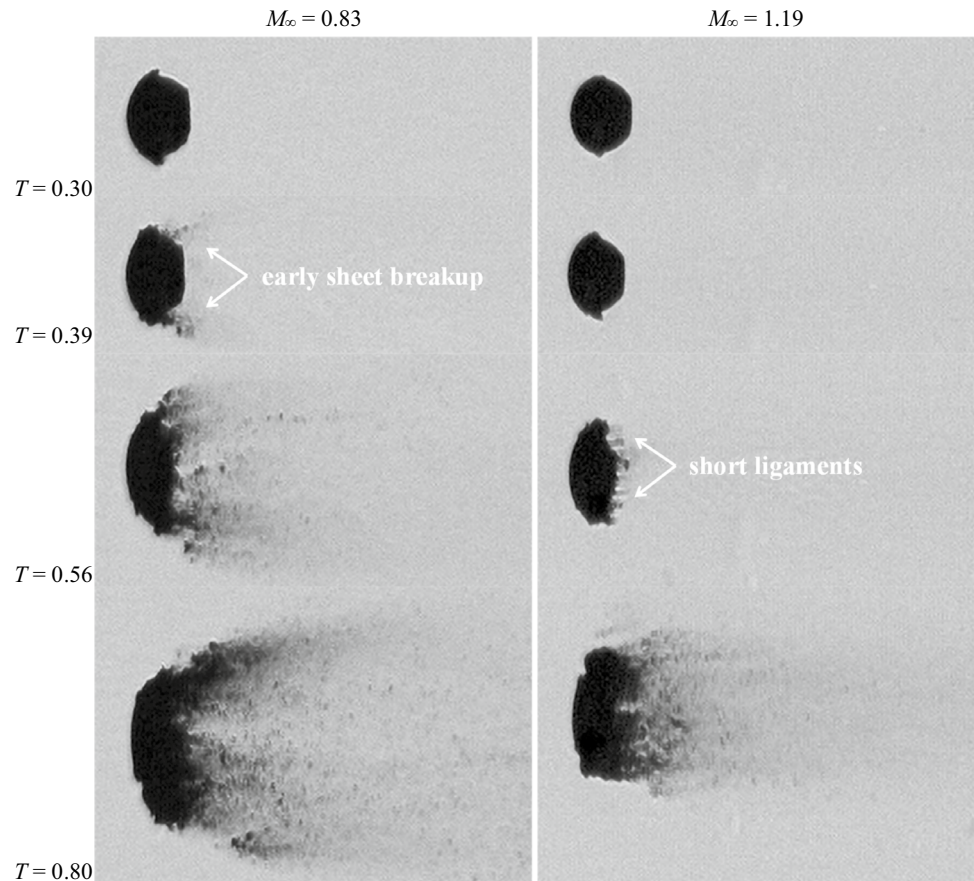


3.5 Effect of the Ohnesorge number

Figure 19 displays the breakup process of water droplets at $M_\infty=0.83$ (Case 3.3) and $M_\infty=1.19$ (Case 5.3). Compared to ethylene glycol, water is much less viscous and yields a 20 times lower Ohnesorge number. The reduction in the liquid viscosity weakens the capability of sustaining

large liquid sheets. Consequently the corresponding breakup initiations are much earlier than those of ethylene glycol droplets at the same M_∞ (0.39 vs. 0.63 at $M_\infty=0.83$, 0.56 vs. 0.69 at $M_\infty=1.19$). Furthermore, in contrast to the long outstretched ligaments observed for ethylene glycol droplets in supersonic flows, the ligaments of water droplets extend over a very limited distance before disintegration ($T=0.56$

Fig. 19 Breakup process of water droplets at $M_\infty = 0.83$ (Case 3.3) and 1.19 (Case 5.3)



at $M_\infty = 1.19$). This is consistent with the observation by Stapper et al. (1992) that less viscous liquids sustain shorter ligaments.

4 Conclusions

The present experimental work compares the stripping breakup of liquid droplets in subsonic and supersonic flows. Millimeter-sized droplets are impacted by a planar shock wave generated in a shock tube. The process of deformation and fragmentation is visualized in a shadow/schlieren system and recorded by an ultra-high-speed camera. Through controlling the shock strength and employing different liquids and gases, the Weber number is maintained around 1100, while the flow Mach number M_∞ varies from 0.3 to 1.19 and the Reynolds number Re from 2600 to 24,000. The effects of changing flow conditions on the breakup process are summarized as follows.

The droplet deformation prior to the breakup, including flattening of windward and leeward surfaces and growth of the liquid sheet at the equator, is weakened by increasing M_∞ . The sheet is initiated further downstream along the droplet surface at higher M_∞ .

In subsonic flows, the stripping breakup starts with the fragmentation of the liquid sheet. As M_∞ increases, distinct breakup features emerge at the breakup initiation, such as multiple bags formed along the periphery and ligament structures stretching in the wake. Correspondingly, the breakup initiation is significantly postponed. In subsonic flows, the breakup generates uniformly fine fragments spreading widely in the cross-stream direction. At higher M_∞ , the fragments are of less uniform sizes and constrained within a narrower region behind the main body.

Although decreasing Re tends to have a complementary role to increasing M_∞ , the effect is marginal on main breakup behaviors.

Lowering Oh reduces the size of liquid sheets and ligaments and results in earlier breakup initiation.

Although many features discussed in the present study focus on detailed breakup structures, they play crucial roles in determining the final fragmentation pattern. The dependency of fragment sizes and spatial distributions on the flow Mach number is especially important for industrial applications, where the atomization process is constantly optimized to generate widely-spread uniformly-sized fragments.

Acknowledgements Open Access funding provided by Projekt DEAL. The authors acknowledge funding by the European Research Council (ERC) under the European Union's Horizon 2020 research and innovation program (Grant agreement No. 667483).

Compliance with ethical standards

Conflict of interest There is no financial or personal relationship between authors and other people or organizations that could inappropriately influence or bias the work.

Open Access This article is licensed under a Creative Commons Attribution 4.0 International License, which permits use, sharing, adaptation, distribution and reproduction in any medium or format, as long as you give appropriate credit to the original author(s) and the source, provide a link to the Creative Commons licence, and indicate if changes were made. The images or other third party material in this article are included in the article's Creative Commons licence, unless indicated otherwise in a credit line to the material. If material is not included in the article's Creative Commons licence and your intended use is not permitted by statutory regulation or exceeds the permitted use, you will need to obtain permission directly from the copyright holder. To view a copy of this licence, visit <http://creativecommons.org/licenses/by/4.0/>.

References

- Aalburg C, Faeth GM, van Leer B (2003) Deformation and drag properties of round drops subjected to shock-wave disturbances. *AIAA J* 41(12):2371–2378. <https://doi.org/10.2514/2.6862>
- Anderson IE, Figliola RS, Morton H (1991) Flow mechanisms in high pressure gas atomization. *Mater Sci Eng A* 148(1):101–114. [https://doi.org/10.1016/0921-5093\(91\)90870-S](https://doi.org/10.1016/0921-5093(91)90870-S)
- Bailey AB, Haitt J (1972) Sphere drag coefficients for a broad range of Mach and Reynolds numbers. *AIAA J* 10(11):1436–1440. <https://doi.org/10.2514/3.50387>
- Biasiori-Poulanges L, El-Rabii H (2019) High-magnification shadowgraphy for the study of drop breakup in a high-speed gas flow. *Opt Lett* 44(23):5884–5887. <https://doi.org/10.1364/ol.44.005884>
- Charters AC, Thomas RN (1945) The aerodynamic performance of small spheres from subsonic to high supersonic velocities. *J Aeronaut Sci* 12(4):468–476. <https://doi.org/10.2514/8.11287>
- Chou WH, Hsiang LP, Faeth GM (1997) Temporal properties of drop breakup in the shear breakup regime. *Int J Multiph Flow* 23(4):651–669. [https://doi.org/10.1016/S0301-9322\(97\)00006-2](https://doi.org/10.1016/S0301-9322(97)00006-2)
- Curran ET (2001) Scramjet engines: the first forty years. *J Propul Power* 17(6):1138–1148. <https://doi.org/10.2514/2.5875>
- Dinh TN, Li GJ, Theofanous TG (2003) An investigation of droplet breakup in a high mach, low weber number regime. In: 41st aerospace sciences meeting and exhibit. American Institute of Aeronautics and Astronautics, Reston, Virginia, p 317. <https://doi.org/10.2514/6.2003-317>
- Dorschner B, Biasiori-Poulanges L, Schmidmayer K, El-Rabii H, and Colonius T. (2020) On the formation and recurrent shedding of ligaments in droplet Aerobreakup. [arXiv:2003.00048](https://arxiv.org/abs/2003.00048)
- Engelbert C, Hardalupas Y, Whitelaw JH (1995) Breakup phenomena in coaxial airblast atomizers. *Proc Royal Soc London, A* 451(1941):189–229. <https://doi.org/10.1098/rspa.1995.0123>
- Gonzalez RC, Woods RE, Eddins SL (2004) Digital image processing using MATLAB. Pearson Education India
- Guildenbecher DR, López-Rivera C, Sojka PE (2009) Secondary atomization. *Exp Fluids* 46(3):371–402. <https://doi.org/10.1007/s00348-008-0593-2>
- Hanson AR, Domich EG, Adams HS (1963) Shock tube investigation of the breakup of drops by air blasts. *Phys Fluids* 6(8):1070–1080. <https://doi.org/10.1063/1.1706864>
- Hardalupas Y, Whitelaw JH (1994) Characteristics of sprays produced by coaxial airblast atomizers. *J Propul Power* 10(4):453–460. <https://doi.org/10.2514/3.23795>
- Hinze JO (1955) Fundamentals of the hydrodynamic mechanism of splitting in dispersion processes. *AIChE J* 1(3):289–295. <https://doi.org/10.1002/aic.690010303>
- Hsiang L-P, Faeth GM (1995) Drop deformation and breakup due to shock wave and steady disturbances. *Int J Multiph Flow* 21(4):545–560. [https://doi.org/10.1016/0301-9322\(94\)00095-2](https://doi.org/10.1016/0301-9322(94)00095-2)
- Igra D, Takayama K (2001) Investigation of aerodynamic breakup of a cylindrical water droplet. *At Sprays* 11(2):20. <https://doi.org/10.1615/AtomizSpr.v11.i2.50>
- Igra D, Takayama K (2003) Experimental investigation of two cylindrical water columns subjected to planar shock wave loading. *J Fluids Eng* 125(2):325–331. <https://doi.org/10.1115/1.1538628>
- Inamura T, Yanaoka H, Kawada T (2009) Visualization of airflow around a single droplet deformed in an airstream. *At Sprays* 19(7):667–677. <https://doi.org/10.1615/AtomizSpr.v19.i7.50>
- Jalaal M, Mehravaran K (2014) Transient growth of droplet instabilities in a stream. *Phys Fluids* 26(1):012101. <https://doi.org/10.1063/1.4851056>
- Joseph DD, Belanger J, Beavers G (1999) Breakup of a liquid drop suddenly exposed to a high speed airstream. *Int J Multiph Flow* 25:1263–1303. [https://doi.org/10.1016/S0301-9322\(99\)00043-9](https://doi.org/10.1016/S0301-9322(99)00043-9)
- Kailasanath K (2003) Recent developments in the research on pulse detonation engines. *AIAA J* 41(2):145–159. <https://doi.org/10.2514/2.1933>
- Karyagin VP, Lopatkin AI, Shvets AI, Shilin NM (1991) Experimental investigation of the separation of flow around a sphere. *Fluid Dyn* 26(1):126–129. <https://doi.org/10.1007/bf01050124>
- Kékesi T, Amberg G, Prahll Wittberg L (2014) Drop deformation and breakup. *Int J Multiph Flow* 66(June):1–10. <https://doi.org/10.1016/j.ijmultiphaseflow.2014.06.006>
- Kim J, Kwon Lee J, Mu Lee K (2016) Accurate image super-resolution using very deep convolutional networks. In: 2016 IEEE conference on computer vision and pattern recognition (CVPR), pp 1646–1654. <https://doi.org/10.1109/CVPR.2016.182>
- Lane WR (1951) Shatter of drops in streams of air. *Ind Eng Chem* 43(6):1312–1317. <https://doi.org/10.1021/ie50498a022>
- Lee CH, Reitz RD (2000) An experimental study of the effect of gas density on the distortion and breakup mechanism of drops in high speed gas stream. *Int J Multiph Flow* 26(2):229–244. [https://doi.org/10.1016/S0301-9322\(99\)00020-8](https://doi.org/10.1016/S0301-9322(99)00020-8)
- Liepmann HW, Roshko A (2001) Elements of gasdynamics. Courier Corporation
- Liu Z, Reitz RD (1997) An analysis of the distortion and breakup mechanisms of high speed liquid drops. *Int J Multiph Flow* 23(4):631–650. [https://doi.org/10.1016/S0301-9322\(96\)00086-9](https://doi.org/10.1016/S0301-9322(96)00086-9)
- Meng JC, Colonius T (2015) Numerical simulations of the early stages of high-speed droplet breakup. *Shock Waves* 25(4):399–414. <https://doi.org/10.1007/s00193-014-0546-z>
- Meng JC, Colonius T (2018) Numerical simulation of the aerobreakup of a water droplet. *J Fluid Mech* 835:1108–1135. <https://doi.org/10.1017/jfm.2017.804>
- Mostaghimi J, Pasandideh-Fard M, Chandra S (2002) Dynamics of splot formation in plasma spray coating process. *Plasma Chem Plasma Process* 22(1):59–84. <https://doi.org/10.1023/A:1012940515065>

- Nagata T, Nonomura T, Takahashi S, Mizuno Y, Fukuda K (2016) Investigation on subsonic to supersonic flow around a sphere at low Reynolds number of between 50 and 300 by direct numerical simulation. *Phys Fluids* 28(5):056101. <https://doi.org/10.1063/1.4947244>
- Nayfeh AH, Saric WS (1971) Non-linear kelvin-helmholtz instability. *J Fluid Mech* 46(2):209–231. <https://doi.org/10.1017/S0022112071000491>
- Opfer L, Roisman IV, Venzmer J, Klostermann M, Tropea C (2014) Droplet-air collision dynamics: evolution of the film thickness. *Phys Rev E* 89(1):013023. <https://doi.org/10.1103/PhysRevE.89.013023>
- Ortiz C, Joseph DD, Beavers GS (2004) Acceleration of a liquid drop suddenly exposed to a high-speed airstream. *Int J Multiph Flow* 30(2):217–224. <https://doi.org/10.1016/j.ijmultiphaseflow.2003.11.004>
- Papamoschou D, Roshko A (1988) The compressible turbulent shear layer: an experimental study. *J Fluid Mech* 197(1973):453–477. <https://doi.org/10.1017/S0022112088003325>
- Pilch M, Erdman CA (1987) Use of breakup time data and velocity history data to predict the maximum size of stable fragments for acceleration-induced breakup of a liquid drop. *Int J Multiph Flow* 13(6):741–757. [https://doi.org/10.1016/0301-9322\(87\)90063-2](https://doi.org/10.1016/0301-9322(87)90063-2)
- Ranger AA, Nicholls JA (1969) Aerodynamic shattering of liquid drops. *AIAA J* 7(2):285–290. <https://doi.org/10.2514/3.5087>
- Reitz RD, Diwakar R (1986) Effect of Drop breakup on fuel sprays. *SAE transactions*, pp 218–227. <https://doi.org/10.4271/860469>
- Schmehl R (2003) Modeling droplet breakup in complex two-phase flows. In: 9th international conference on liquid atomization and spray systems, ICLASS 13-17 July 2003, Surrento, Italy
- Shinjo J, Umemura A (2010) Simulation of liquid jet primary breakup: dynamics of ligament and droplet formation. *Int J Multiph Flow* 36(7):513–532. <https://doi.org/10.1016/j.ijmultiphaseflow.2010.03.008>
- Lagutkin S, Achelis L, Sheikhaliev S, Uhlenwinkel V, Srivastava V (2004) Atomization process for metal powder. *Mater Sci Eng A* 383(1 SPEC. ISS.):1–6. <https://doi.org/10.1016/j.msea.2004.02.059>
- Stapper BE, Samuelsen GS (1990) An experimental study of the breakup of a two-dimensional liquid sheet in the presence of co-flow air shear. In: 28th aerospace sciences meeting, p 461. <https://doi.org/10.2514/6.1990-461>
- Stapper BE, Sowa WA, Samuelsen GS (1992) An Experimental study of the effects of liquid properties on the breakup of a two-dimensional liquid sheet. *J Eng Gas Turb Power* 114(1):39–45. <https://doi.org/10.1115/1.2906305>
- Theofanous TG (2011) Aerobreakup of newtonian and viscoelastic liquids. *Annu Rev Fluid Mech* 43(1):661–690. <https://doi.org/10.1146/annurev-fluid-122109-160638>
- Theofanous TG, Li GJ (2008) On the physics of aerobreakup. *Phys Fluids* 20(5):052103. <https://doi.org/10.1063/1.2907989>
- Theofanous TG, Li GJ, Dinh TN (2004) Aerobreakup in rarefied supersonic gas flows. *J Fluids Eng* 126(4):516. <https://doi.org/10.1115/1.1777234>
- Theofanous TG, Mitkin VV, Ng CL, Chang C-H, Deng X, Sushchikh S (2012) The physics of aerobreakup. II. Viscous liquids. *Phys Fluids* 24(2):022104. <https://doi.org/10.1063/1.3680867>
- Villermaux E, Bossa B (2009) Single-drop fragmentation determines size distribution of raindrops. *Nat Phys* 5(9):697–702. <https://doi.org/10.1038/nphys1340>
- Xiao F, Wang ZG, Sun MB, Liu N, Yang X (2017) Simulation of drop deformation and breakup in supersonic flow. *Proc Combust Inst* 36(2):2417–2424. <https://doi.org/10.1016/j.proci.2016.09.016>

Publisher's Note Springer Nature remains neutral with regard to jurisdictional claims in published maps and institutional affiliations.

A.3 Experimental Investigation of Shock-Induced Tandem Droplet Breakup

Zhaoguang Wang, Marcus Giglmaier, Thomas Hopfes, Nikolaus A. Adams

In: *Physics of Fluids* 33 (2021), p. 012113.
<https://doi.org/10.1063/5.0039098>.

Contribution: My contributions to this publication included conceiving the original idea, designing the experimental methodology and carrying out the experiments. I verified the experimental methods and analyzed the data by adapting post-processing tools. The original manuscript was written by me.

License to Publish Agreement

Journal: Physics of Fluids

Manuscript ID #: POF20-AR-04131R

Article Title: Experimental Investigation of Shock Induced Tandem Droplet Breakup

Name: Zhaoguang Wang

Author(s): Zhaoguang Wang, Thomas Hopfes, Marcus Giglmaier, and Nikolaus Adams

Agreement Date: 24-Dec-2020 21:44 GMT

Copyright Ownership and Grant of Rights

For the purposes of this License, the "Work" consists of all content within the article itself and made available as part of the article, including but not limited to the abstract, tables, figures, graphs, images, and multimedia files, as well as any subsequent errata. The Work refers to the content contained in both the Accepted Manuscript (AM) and the Version of Record (VOR). "Supplementary Material" consists of material that is associated with the article but linked to or accessed separately (available electronically only), including but not limited to data sets and any additional files.

This Agreement is an Exclusive License to Publish not a Transfer of Copyright. Copyright to the Work remains with the Author(s) or, in the case of a Work Made for Hire, with the Author(s)' employer(s). AIP Publishing LLC shall own and have the right to register in its name the copyright to the journal issue or any other collective work in which the Work is included. Any rights granted under this License are contingent upon acceptance of the Work for publication by AIP Publishing. If for any reason and at its own discretion AIP Publishing decides not to publish the Work, this License is considered void.

Each Copyright Owner hereby grants to AIP Publishing LLC the following irrevocable rights for the full term of United States and foreign copyrights (including any extensions):

1. The exclusive right and license to publish, reproduce, distribute, transmit, display, store, translate, edit, adapt, and create derivative works from the Work (in whole or in part) throughout the world in all formats and media whether now known or later developed, and the nonexclusive right and license to do the same with the Supplementary Material.
2. The right for AIP Publishing to freely transfer and/or sublicense any or all of the exclusive rights listed in #1 above. Sublicensing includes the right to authorize requests for reuse of the Work by third parties.
3. The right for AIP Publishing to take whatever steps it considers necessary to protect and enforce, at its own expense, the exclusive rights granted herein against third parties.

Author Rights and Permitted Uses

Subject to the rights herein granted to AIP Publishing, each Copyright Owner retains ownership of copyright and all other proprietary rights such as patent rights in the Work.

Each Copyright Owner retains the following nonexclusive rights to use the Work, without obtaining permission from AIP Publishing, in keeping with professional publication ethics, and provided clear credit is given to its first publication in an AIP Publishing journal. Any reuse must include a full credit line acknowledging AIP Publishing's publication and a link to the VOR on AIP Publishing's site.

Each Copyright Owner may:

1. Reprint portions of the Work (excerpts, figures, tables) in future works created by the Author, in keeping with professional publication ethics.
2. Post the Accepted Manuscript (AM) to their personal web page or their employer's web page immediately after acceptance by AIP Publishing.
3. Deposit the AM in an institutional or funder-designated repository immediately after acceptance by AIP Publishing.

4. Use the AM for posting within scientific collaboration networks (SCNs). For a detailed description of our policy on posting to SCNs, please see our Web Posting Guidelines (<https://publishing.aip.org/authors/web-posting-guidelines>).
5. Reprint the Version of Record (VOR) in print collections written by the Author, or in the Author's thesis or dissertation. It is understood and agreed that the thesis or dissertation may be made available electronically on the university's site or in its repository and that copies may be offered for sale on demand.
6. Reproduce copies of the VOR for courses taught by the Author or offered at the institution where the Author is employed, provided no fee is charged for access to the Work.
7. Use the VOR for internal training and noncommercial business purposes by the Author's employer.
8. Use the VOR in oral presentations made by the Author, such as at conferences, meetings, seminars, etc., provided those receiving copies are informed that they may not further copy or distribute the Work.
9. Distribute the VOR to colleagues for noncommercial scholarly use, provided those receiving copies are informed that they may not further copy or distribute the Work.
10. Post the VOR to their personal web page or their employer's web page 12 months after publication by AIP Publishing.
11. Deposit the VOR in an institutional or funder-designated repository 12 months after publication by AIP Publishing.
12. Update a prior posting with the VOR on a noncommercial server such as arXiv, 12 months after publication by AIP Publishing.

Author Warranties

Each Copyright Owner may:

1. Reprint portions of the Work (excerpts, figures, tables) in future works created by the Author, in keeping with professional publication ethics.
2. Post the Accepted Manuscript (AM) to their personal web page or their employer's web page immediately after acceptance by AIP Publishing.
3. Deposit the AM in an institutional or funder-designated repository immediately after acceptance by AIP Publishing.
4. Use the AM for posting within scientific collaboration networks (SCNs). For a detailed description of our policy on posting to SCNs, please see our Web Posting Guidelines (<https://publishing.aip.org/authors/web-posting-guidelines>).
5. Reprint the Version of Record (VOR) in print collections written by the Author, or in the Author's thesis or dissertation. It is understood and agreed that the thesis or dissertation may be made available electronically on the university's site or in its repository and that copies may be offered for sale on demand.
6. Reproduce copies of the VOR for courses taught by the Author or offered at the institution where the Author is employed, provided no fee is charged for access to the Work.
7. Use the VOR for internal training and noncommercial business purposes by the Author's employer.
8. Use the VOR in oral presentations made by the Author, such as at conferences, meetings, seminars, etc., provided those receiving copies are informed that they may not further copy or distribute the Work.
9. Distribute the VOR to colleagues for noncommercial scholarly use, provided those receiving copies are informed that they may not further copy or distribute the Work.
10. Post the VOR to their personal web page or their employer's web page 12 months after publication by AIP Publishing.
11. Deposit the VOR in an institutional or funder-designated repository 12 months after publication by AIP Publishing.
12. Update a prior posting with the VOR on a noncommercial server such as arXiv, 12 months after publication by AIP Publishing.

Author Warranties

Each Author and Copyright Owner represents and warrants to AIP Publishing the following:

Experimental investigation of shock-induced tandem droplet breakup

Cite as: Phys. Fluids **33**, 012113 (2021); <https://doi.org/10.1063/5.0039098>

Submitted: 30 November 2020 . Accepted: 31 December 2020 . Published Online: 29 January 2021

 Zhaoguang Wang (王召光),  Thomas Hopfes,  Marcus Giglmaier, and Nikolaus A. Adams



View Online

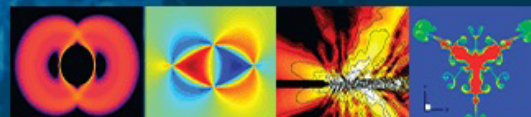


Export Citation



CrossMark

Physics of Fluids
GALLERY OF COVERS



Experimental investigation of shock-induced tandem droplet breakup

Cite as: *Phys. Fluids* **33**, 012113 (2021); doi: [10.1063/5.0039098](https://doi.org/10.1063/5.0039098)

Submitted: 30 November 2020 • Accepted: 31 December 2020 •

Published Online: 29 January 2021



Zhaoguang Wang (王召光),^{a)} Thomas Hopfes, Marcus Giglmaier, and Nikolaus A. Adams

AFFILIATIONS

Chair of Aerodynamics and Fluid Mechanics, Technical University of Munich, 85748 Garching, Germany

^{a)} Author to whom correspondence should be addressed: zg.wang@tum.de

ABSTRACT

For deeper insights into the dynamics of dense sprays, the present experimental work investigates the shock-induced breakup of two identically sized water droplets in tandem formation. The breakup process is visualized in a shadowgraph system and captured by an ultra-high-speed camera. The experimental Weber number ranges from 13 to 180, and the separation distance between the droplets is varied between 1.2 and 10.5 times of the droplet diameter. While the tandem formation exerts marginal influence on the lead droplet, the breakup intensity of the trailing droplet is consistently attenuated as the separation distance falls below critical levels. The time of initial deformation is postponed, the maximum cross-stream diameter is reduced, and the mean drag coefficient is lowered. These effects are more profound at lower Weber numbers and closer separation distances. The attenuation of the breakup intensity is also reflected by the formation of smaller bags in bag and bag-and-stamen morphologies and by the narrower cross-stream dispersion of fragments in multibag and shear stripping morphologies. When positioned in close proximity to the lead droplet, the trailing droplet fails to follow the conventional breakup morphologies. Instead, it either punctures or coalesces with the lead droplet.

Published under license by AIP Publishing. <https://doi.org/10.1063/5.0039098>

I. INTRODUCTION

Droplet breakup is a relevant phenomenon in a variety of applications, including fuel injection,¹ powder metallurgy,² and spray coatings.³ Previous research has concluded that the droplet breakup process is mainly governed by the Weber number (We) and the Ohnesorge number (Oh),^{4,5}

$$We = \rho_g u_g^2 d_0 / \sigma, \quad (1)$$

$$Oh = \mu_d / \sqrt{\rho_d d_0 \sigma}, \quad (2)$$

where ρ_g and u_g are the density and the velocity of the gas flow and d_0 , σ , μ_d , and ρ_d are the initial diameter, the surface tension, the dynamic viscosity, and the density of the liquid droplet. The Weber number and the Ohnesorge number compare the disruptive aerodynamic force and the viscous force against the restorative surface tension, respectively. When $Oh < 0.1$, the significance of the liquid viscosity becomes negligible and We turns to be the sole dominant factor.⁶

The aerodynamic breakup of single droplets has been extensively investigated and reviewed in detail by Pilch and Erdman,⁷

Faeth *et al.*,⁸ and Guildenbecher *et al.*⁶ As the aerodynamic force becomes increasingly intense, the corresponding breakup pattern transitions from bag breakup^{9–11} to stripping breakup.^{12–14} There exist several in-between multimode morphologies,^{15,16} and the two covered in the current work are bag-and-stamen breakup^{7,17} and multibag breakup.^{18,19}

However, the conventional understandings of single droplet breakup do not describe the breakup behavior in dense sprays accurately. In practical applications such as diesel injections²⁰ and agricultural sprays,²¹ droplets appear in close proximity instead of being isolated. The interaction between adjacent droplets has to be considered to properly estimate the fragment sizes. Therefore, the arrangement of droplets in tandem formation is more representative than single droplets, and the initial on-center separation distance s between the tandem droplets becomes an additional variable of importance. The associated tandem breakup behavior is investigated thoroughly in the current work.

Most of the previous research about droplets in tandem formation is dedicated to the evaluation of drag coefficients. Liu *et al.*²² study experimentally the laminar flow field around an infinite droplet chain with the normalized on-center separation distance

$S = s/d_0$ varied between 2 and 12. They conclude that the drag coefficient of monodisperse droplets is up to an order of magnitude lower than the drag coefficient of isolated droplets. Mulholland *et al.*²³ conduct similar experiments but with S ranging from 1.7 to 1700. They propose an empirical formulation to model the drag coefficient and find that the value is significantly diminished as the separation distance drops below 150. Poo and Ashgriz²⁴ investigate a stream of closely spaced droplets with $S < 5$ in a turbulent flow and state that the drag coefficient is 4–5 times smaller compared to isolated droplets. There are other studies with the focus on a finite number of droplets in tandem formation instead of an infinite stream. Temkin and Ecker²⁵ study the interaction between two droplets with S from 1.5 to 11 and Reynolds numbers below 150. Based on the quantified changes of drag coefficients, they show that the upstream droplet is not affected by the tandem formation while the downstream one experiences reduction up to 50%. The result also suggests that the region of influence behind the upstream droplet extends over 15 droplet diameters. Nguyen and Dunn-Rankin²⁶ examine vertically falling droplet packets composed of 4 droplets separated by 5.5 diameters with the Reynolds number around 80. They analyze the trajectory of the first trailing droplet and present that the drag coefficient is 25% lower than that of the lead droplet. Chiang and Sirignano²⁷ investigate numerically the transportation of three droplets aligned with the flow direction. Their results indicate that the drag of the first two droplets differs profoundly while the difference between the downstream two droplets becomes insignificant.

The amount of research focusing on the deformation and breakup of tandem droplets is very limited, among which the experimental work is even scarcer. Zhao *et al.*²⁸ conduct experiments of two neighboring droplets at $We = 12.3$ in the bag breakup regime with the normalized separation distance S below 3. For cases with the two droplets positioned in tandem, they report a coalescence mode at $S < 1.3$ and a puncture mode at higher S . Igra and Takayama²⁹ experimentally investigate the shear stripping breakup of two water columns separated 5 diameters away at the Weber number of 6900. The same breakup behavior as single columns is observed for the front column while the rear one deforms at a much lower rate. Others adopt numerical methods for the relevant research. Quan *et al.*³⁰ employ a finite-volume scheme to investigate the deformation of tandem droplets spaced within 6 diameters at Weber numbers of 40,

4, and 0.4. They present a mushroom shape formed by the droplet pair at the two largest Weber numbers with $S = 1.6$. Simulations of similar tandem arrangements are carried out by Kékesi *et al.*,³¹ with the Weber number of 20 and the separation distance from 1.5 to 5 droplet diameters. They conclude that the trailing droplet either shoots through or merges with the lead droplet and its breakup time is increased significantly. Stefanitsis *et al.*³² apply the volume of fluid method to study the breakup of four diesel droplets in tandem formation at Weber numbers varied between 15 and 64. They analyze the deformation of the third droplet and present a new breakup mode termed shuttlecock. Their results show that the interaction between tandem droplets becomes important for separation distances below 9 droplet diameters.

To shed more light on the breakup features of tandem droplets, the current experimental work intends to assess the significance of the tandem formation over a wide range of Weber numbers and separation distances. In contrast to most of the previous works that focus on the evaluation of drag reduction, we place emphasis on detailed description of deformation patterns and breakup structures. The present results can serve as bases for potential numerical validations and for more accurate modeling of fragment sizes and dispersion.

II. EXPERIMENTAL SETUP

The layout of the shock tube and the measurement system employed in the present work is provided in Fig. 1. The setup is the same as described in our previous work,³³ except for the position of the cookie-cutter. The square cookie-cutter, which conventionally locates upstream of the test section to remove boundary layers, is shifted downstream to achieve a longer period of steady-flow conditions. Figure 2 sketches the propagation of the incident shock inside the tube, and Fig. 3 plots the corresponding post-shock pressure at the test point measured by PCB Piezotronics ICP® fast-response pressure sensors. When reaching the front of the test section, the incident shock partially reflects since the cross section contracts to a $190 \times 190 \text{ mm}^2$ square ($t = -0.5 \text{ ms}$ in Fig. 2). The reflected shock leads to a short transition period ($\sim 0.2 \text{ ms}$) after the pressure at the test location experiences a stepwise increase at the arrival of the incident shock ($t = 0 \text{ ms}$ in Fig. 3). As the incident shock exits from the test section, the increase in the cross-sectional area induces

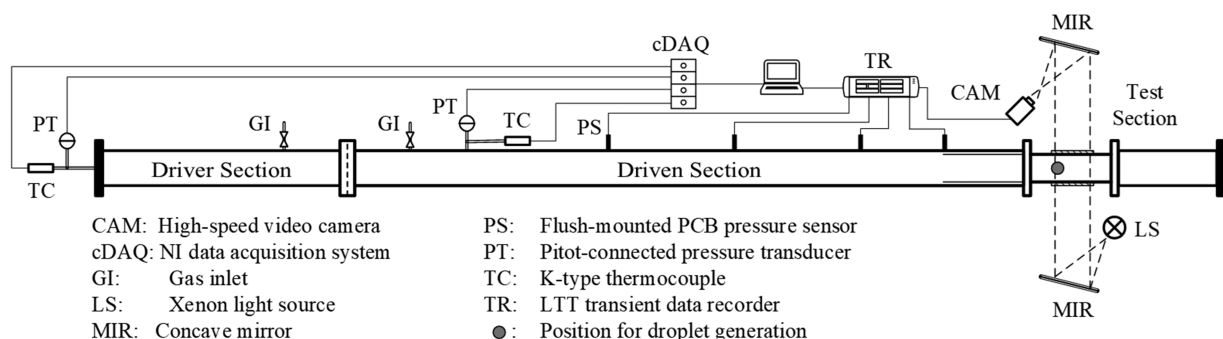


FIG. 1. Layout of the shock tube and the measurement system.

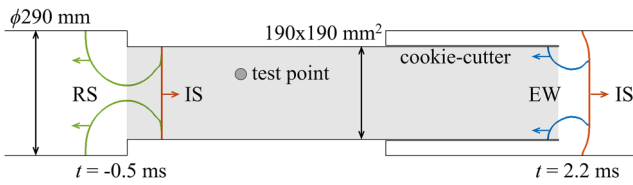


FIG. 2. Wave dynamics inside the test section. The test section is marked with gray shades. The incident shock propagates from left to right. IS: incident shock; RS: reflected shock; EW: expansion wave.

generation of additional expansion waves ($t = 2.2$ ms in Fig. 2). These expansion waves propagate upstream and give rise to pressure drop and velocity increase at the test location ($t = 4.5$ ms in Fig. 3). By shifting the cookie-cutter to the downstream of the test section, the upstream propagation of the expansion waves is postponed, and thus, the steady-flow time window is prolonged from ~ 2 ms in the previous setup³³ to ~ 4.5 ms, at the expense of causing a short transition period and slightly higher flow fluctuations.

In the current work, the steady-flow period covers the entire breakup process of cases at high Weber numbers. For cases at the two lowest Weber numbers ($We = 13$ and 24), the early-stage deformation and the initiation of bag development are within the steady-flow period, but the onset of bag rupture is beyond. Nevertheless, although the timing for the bag rupture is altered by the changing flow conditions, the main deformation patterns are preserved for these cases. Particularly, the early-stage parameters quantified in Sec. III E are not affected.

In the current experiments, the velocity of the incident shock is calculated by measuring the time difference between moments when the incident shock passes two 0.75 m-separated pressure sensors directly upstream of the test section. Based on this shock speed and the initial atmospheric conditions, we conduct 2D axisymmetric numerical simulations to estimate post-shock flow parameters. As shown in Fig. 3, the simulated pressure profile at the test point is in good agreement with that measured experimentally. This justifies the application of the flow velocity and density obtained from the numerical simulation in the calculation of Weber numbers.

In terms of flow visualization, shadowgraph images of the droplet breakup are recorded by a Shimadzu HyperVision HPV-X ultra-high-speed camera at framing rates of 10–40 kfps. The images

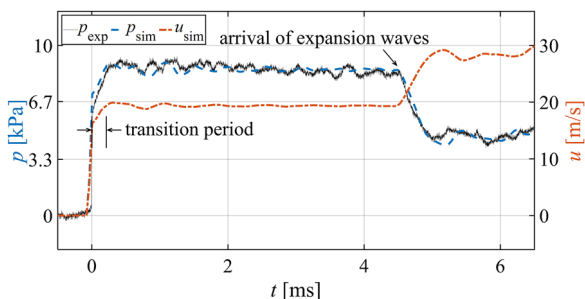


FIG. 3. Post-shock flow pressure and velocity at the test point ($We = 13$).

TABLE I. Operating flow conditions summarized from repeated experiments.

We	Oh_{avg}	$Re_{\infty avg}$	Breakup morphology
13 (± 1.3)	2.4×10^{-3}	2.5×10^3	Bag breakup
24 (± 2.2)	2.4×10^{-3}	3.4×10^3	Bag and stamen
70 (± 3.0)	2.3×10^{-3}	6.1×10^3	Multibag breakup
180 (± 10)	2.4×10^{-3}	1.0×10^4	Shear stripping

are processed with background subtraction, contrast adjustment, and super resolution using MATLAB's Very Deep Super-Resolution convolutional neural network.³⁴ The spatial resolution of the resultant images is ~ 0.05 mm/pixel. By counting the pixels that constitute the droplet in the shadowgraph image, the cross-sectional area A is obtained, and the equivalent droplet diameter d_0 is calculated as $d_0 = 2 \times (A/\pi)^{0.5}$.

To generate droplets in tandem formation, two syringe needles separated with a defined spacing are inserted into the test section. After droplets with the diameter of ~ 2 mm are produced at the needle tips, the syringes are withdrawn rapidly detaching the two droplets simultaneously. The current experimental matrix covers four flow conditions, of which the parameters are summarized in Table I based on repeated experiments. The average Weber numbers investigated are 13, 24, 70, and 180, with the corresponding breakup morphology changing from bag breakup to shear stripping. The Ohnesorge number for all cases is approximately 2.4×10^{-3} , making the viscous effect negligible.⁶ The d_0 -based freestream Reynolds number Re_{∞} ,

$$Re_{\infty} = \rho_g u_g d_0 / \mu_g, \quad (3)$$

increases from 2.5×10^3 to 1.0×10^4 . Under each flow condition, seven on-center separation distances $S = s/d_0$ between 1.2 and 10.5 are studied. In addition, single droplet experiments are conducted as well for more comprehensive comparisons.

III. RESULTS AND DISCUSSION

In the current study, the experiment time t is normalized against the characteristic transport time derived by Ranger and Nicholls¹² to yield the non-dimensional time T ,

$$T = t \cdot u_g / \left(d_0 \sqrt{\rho_a / \rho_g} \right). \quad (4)$$

The time for lead and trailing droplets is zeroed at the instant of the incident shock impacting on their respective frontal surface. Nevertheless, the time shift between the tandem droplets is less than 0.06 ms for all cases and insignificant compared to the duration of the breakup process at current conditions. For the sake of consistency and brevity, only the time for the lead droplet is provided in the following image sequences. As presented in Fig. 3, the freestream flow condition remains steady until $t = 4.5$ ms. The corresponding non-dimensional time instants are approximately $T = 1.7, 2.2, 3.6,$ and 6.0 for current experiments at Weber numbers of 13, 24, 70, and 180, respectively. The breakup process is completed under constant flow conditions for high Weber numbers but slightly exceeds the

steady-flow period for low Weber numbers. In the following texts, time instants that exceed this period are marked with T^* instead of T .

Figure 4 provides an overview of the interactive modes between the tandem droplets. Considering that the lead droplet breakup is marginally influenced by the tandem formation, Fig. 4 only categorizes the change of the breakup pattern for the trailing droplet at different separation distances S and Weber numbers We . In the figure, the x -axis S is plotted on the linear scale and the y -axis We on the logarithmic scale. The entire S - We map is divided into three regions. The independent breakup region at the top-right corner represents cases where the trailing droplet undergoes the same breakup process as the lead droplet. The suppressed breakup region at the bottom-left corner contains cases where the trailing droplet fails to follow the breakup morphology of the lead droplet but exhibits either puncture or coalescence modes instead. For cases in the transition region, the breakup morphology of the trailing droplet is the same as that of the lead droplet but the breakup intensity is reduced. The boundary between the independent breakup region and the transition region is of particular importance because it represents the critical separation distance below which the interaction of the tandem droplets has to be taken into account. This critical distance is We -dependent and halved from $S = 10.8$ at $We = 13$ to $S = 5.4$ at $We = 180$.

The following presentation of results starts with illustrating the breakup pattern of the tandem droplets with shadowgraph images for each breakup morphology individually (Secs. III A–III D). In each section, representative cases at a certain Weber number in the transition and the suppressed breakup regions are described in detail while those in the independent breakup region are omitted for conciseness. The discussion is concluded by quantifying the time of initial deformation, the maximum cross-stream diameter, and the mean drag coefficient of the tandem droplets in Sec. III E.

A. Bag breakup

1. Transition region: Smaller bag for the trailing droplet

For the bag breakup of tandem droplets, the present cases with separation distances between 4.7 and 10.5 are identified in the

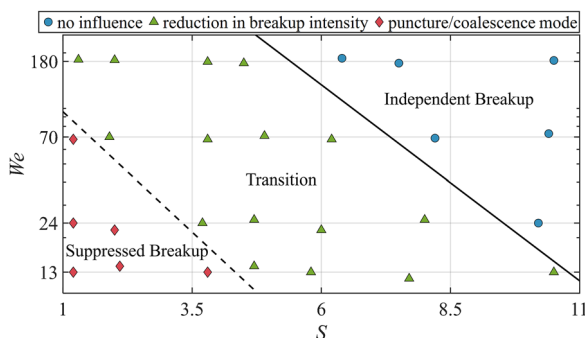


FIG. 4. Change of the breakup pattern of the trailing droplet at different separation distances and Weber numbers, in comparison to the lead droplet. The map is divided into three regions (independent breakup region, transition region, and suppressed breakup region).

transition region. An exemplary case is shown in Fig. 5 with $S = 5.8$ and $We = 13$. Here, the lead droplet replicates the breakup process of single droplets and experiences initial flattening ($T = 1.0$), bag inflation ($T = 1.5$), bag rupture ($T^* = 2.35$), and ring disintegration ($T^* = 2.8$) sequentially. The trailing droplet exhibits the same breakup morphology as the lead droplet but is flattened to a lower cross-stream diameter (d_c) in the early stage and develops a smaller bag at a later time. In all following figures that present breakup structures, the explanatory notes on the right describe the breakup progress of the trailing droplet.

As demonstrated by the top row in Fig. 6, the main variation within the transition region is that the bag formed by the trailing droplet becomes consistently smaller as the separation distance decreases. The reduction of the bag size is associated with the less pronounced flattening in the early stage and results from the fact that the wake flow of the lead droplet shields the trailing droplet and lowers the pressure imposed on its windward surface. This shielding effect is stronger at closer separation distances. The bottom row in Fig. 6 compares the ring structure of the trailing droplet after fragmentation of the bag. On the one hand, smaller bags mean that less mass is shed off through the bag rupture and more remains in the toroidal ring. On the other hand, the bag size also determines the diameter of the ring in a proportional way. Consequently, under the combined influence of these two factors, the ring is thickened when the trailing droplet is in closer proximity to the lead

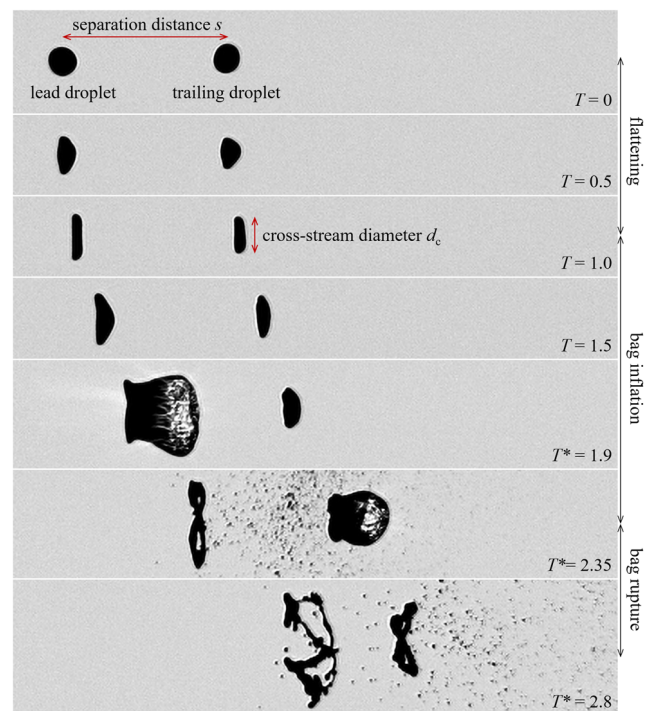


FIG. 5. Weaker flattening and smaller bag size for the trailing droplet under the shielding effect of the lead droplet ($S = 5.8$, $We = 13$). The freestream direction is from left to right for all presented images. As labeled, s and d_c are the initial on-center separation distance and the cross-stream diameter, respectively.

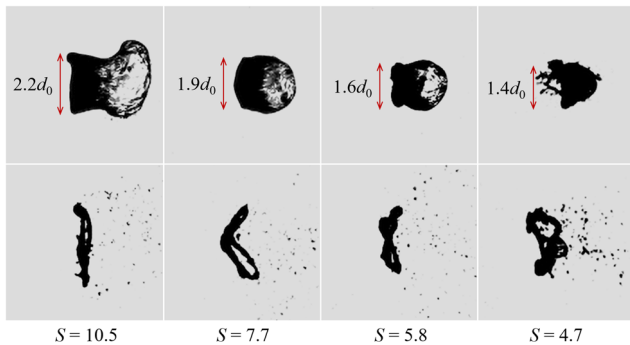


FIG. 6. Variation of the bag size and the ring thickness at different separation distances for the trailing droplet in the bag breakup regime. The top and bottom rows correspond to time instants prior and subsequent to the bag rupture, respectively ($We = 13, 12, 13,$ and 15 from left to right).

droplet. Although the time instants shown in Fig. 6 are beyond the steady-flow period, all cases still share approximately the same flow conditions, and thus, the tendency presented here remains valid qualitatively.

2. Suppressed breakup region: Puncture of the lead droplet by the trailing droplet

The interaction of the tandem droplets at separation distances $S = 2.1$ and 3.8 is identified as the puncture mode in the suppressed breakup region. The corresponding breakup features are exemplified by the case at $S = 2.1$ in Fig. 7. The deformation of the lead droplet progresses in a conventional manner until $T = 1.7$ when the collision

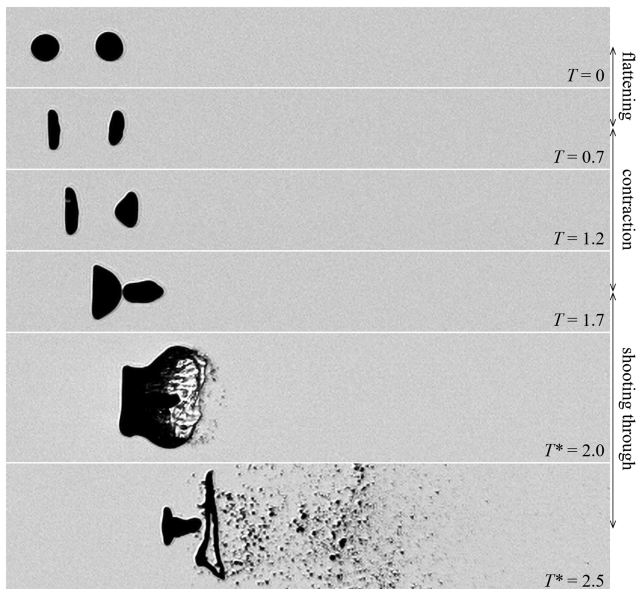


FIG. 7. Puncture of the bag structure of the lead droplet by the trailing droplet ($S = 2.1, We = 14$).

with the trailing droplet triggers an early rupture of the inflating bag. In terms of the trailing droplet, the deformation starts with weakened flattening ($T = 0.7$). As the lead droplet deforms into a thin disk, the trailing droplet suffers from stronger shielding effects and consequently enters a contraction period. The trailing droplet contracts into a triangular shape pointing upstream at $T = 1.2$ and further into an ellipsoid with the major axis aligned with the streamwise direction at $T = 1.7$. The ellipsoidal trailing droplet punctures the bag structure of the lead droplet at $T^* = 2.0$ and escapes from its shelter. Being exposed to the freestream flow, the trailing droplet gets flattened at the windward surface and distorted into a “T” shape at $T^* = 2.5$. In the following period, the droplet fails to reproduce the typical bag breakup but tends to disintegrate into several fragments of comparable sizes to the original.

3. Suppressed breakup region: Coalescence of the tandem droplets

The case at $S = 1.2$ in the suppressed breakup region exhibits new features as presented in Fig. 8 and is categorized as the coalescence mode. The most noticeable feature is the absence of bag structures. The early-stage flattening of the lead droplet is maintained, while the deformation of the trailing droplet starts with streamwise stretching. The disk-shape lead droplet and the teardrop-shape trailing droplet ($T = 1.0$) coalesce into a funnel shape at $T = 1.35$. The coalescence is completed around $T = 1.7$ when the tail of the trailing droplet is swallowed entirely. In the later stage, the deformation of the merged body becomes highly disordered. Apart from the formation and fragmentation of ligament structures ($T^* = 2.8$), the main body tends to split into large children droplets. This coalescence mode and the afore-mentioned puncture mode have also been observed by Zhao *et al.*²⁸ for separation distances below and above 1.3, respectively, with which our present results are in good consistency.

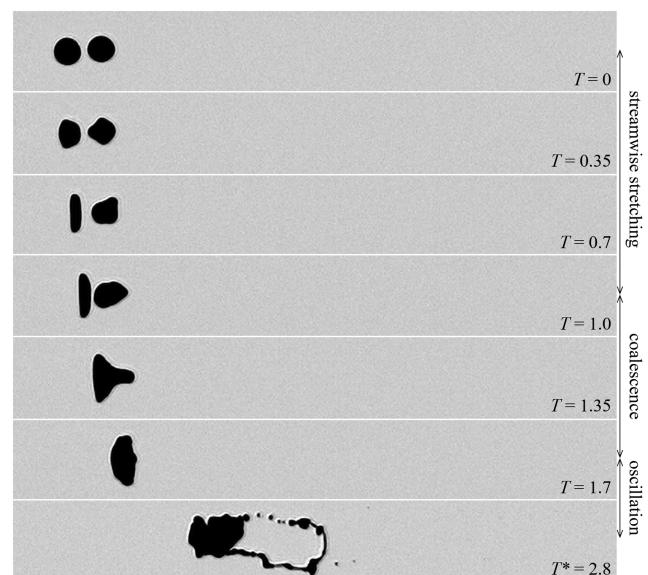


FIG. 8. Coalescence of lead and trailing droplets ($S = 1.2, We = 13$).

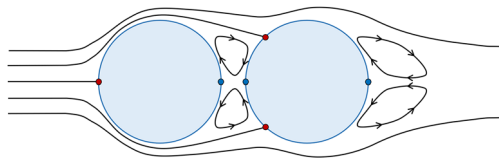


FIG. 9. Simplified 2D sketch of streamlines around tandem droplets at $S = 1.2$. Stagnation points of the highest static pressure are labeled in red and those of low pressure in blue.

To better explain how the shielding effect changes the early-stage deformation of the trailing droplet from cross-stream flattening to streamwise stretching, Fig. 9 presents a simplified 2D sketch of streamlines around two closely packed droplets. The red circles represent stagnation points with the highest static pressure along the droplet surface, and the blue circles correspond to those with relatively lower pressure. With the presence of the lead droplet, the highest pressure at the trailing droplet surface appears at locations near the equator. The resulting pressure imbalance extrudes a sharp nose at the droplet front ($T = 0.35$ in Fig. 8) and results in the following streamwise stretching ($T = 0.7$ in Fig. 8).

In summary, the presence of the lead droplet tends to weaken the bag inflation of the trailing droplet. This reduces the production of fine mist through bag rupture and favors the generation of large fragments. For a more accurate modeling of the fragment size distribution, special attention needs to be paid to cases where the trailing droplet fails to follow bag breakup and produces fragments with sizes comparable to the initial diameter.

B. Bag-and-stamen breakup

1. Transition region: Smaller bag for the trailing droplet

For the bag-and-stamen breakup, the transition region covers experiments with separation distances from $S = 3.7$ to 8.0 in the current study. An exemplary case is shown in Fig. 10 with $S = 8.0$ and $We = 25$. During the initial flattening, a bulge forms at the frontal surface of the lead droplet, marking the development of a stamen ($T = 1.0$). After the bag inflates around the stamen to the maximum size, the bag rupture, the ring fragmentation, and the stamen disintegration take place in succession. The trailing droplet shares similar breakup features except that it deforms at a slower rate and develops a smaller bag.

Figure 11 compares the variation of the bag size (top row) and the ring/stamen thickness (bottom row) of the trailing droplet among cases in the transition region. Although detailed breakup structures are considerably distorted by the shielding effect of the lead droplet, main bag-and-stamen breakup features are still maintained. Nevertheless, the bag of the trailing droplet shrinks and the ring/stamen structures are thickened as the separation distance decreases, which is similar to the observations for bag breakup in Fig. 6.

2. Suppressed breakup region: Puncture of the lead droplet by the trailing droplet

The two cases with the closest separation distances $S = 1.2$ and 2.0 lie in the suppressed breakup region, where the lead droplet

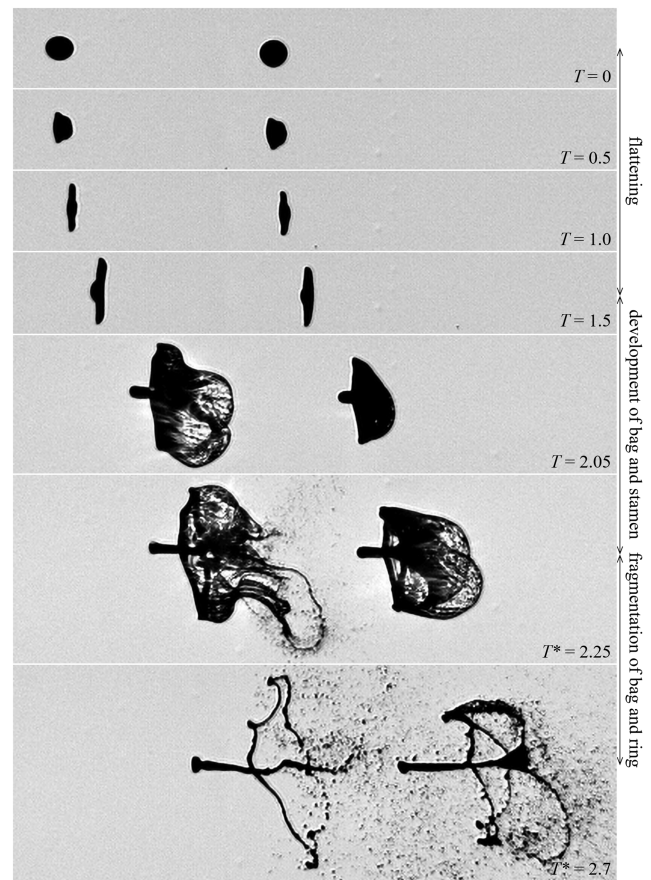


FIG. 10. Weaker flattening and smaller bag size for the trailing droplet under the shielding effect of the lead droplet ($S = 8.0$, $We = 25$).

collides with the trailing droplet during the early development of bag structures as shown in Fig. 12. The shielding effect on the trailing droplet is clearly observed at the very beginning of the deformation. In contrast to the conventional cross-stream flattening, the

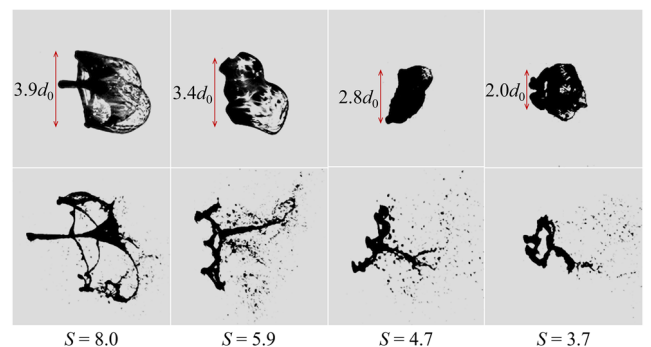


FIG. 11. Variation of the bag size and the ring/stamen thickness at different separation distances for the trailing droplet in the bag-and-stamen breakup regime. The top and bottom rows correspond to time instants prior and subsequent to the bag rupture, respectively ($We = 25, 22, 25$, and 24 from left to right).

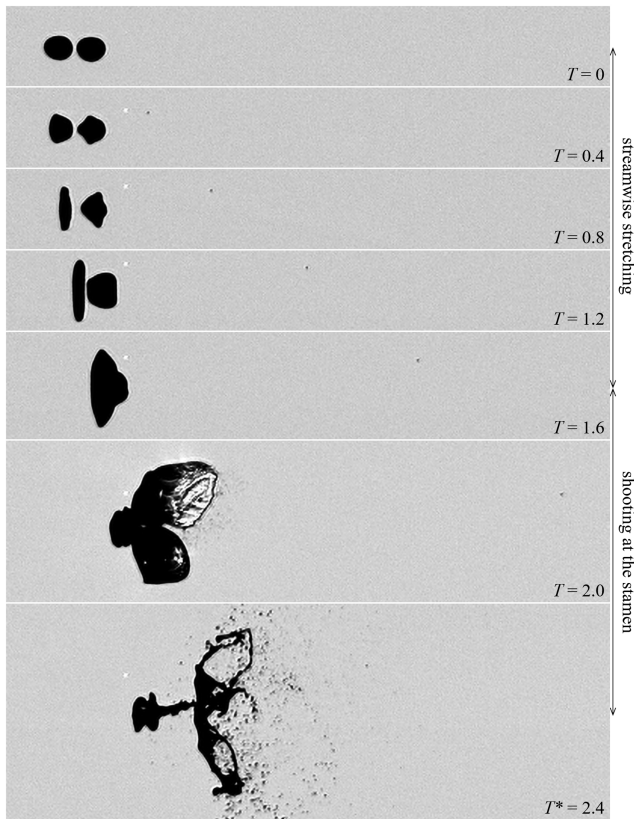


FIG. 12. Puncture of the bag structure of the lead droplet and coalescence of the trailing droplet with the stamen ($S = 1.2$, $We = 24$).

trailing droplet deforms into an arrowhead shape at $T = 0.8$ and later together with the flattened lead droplet constitutes a mushroom shape ($T = 1.2$). This mushroom layout has also been reported in the numerical work by Quan *et al.*³⁰ at We between 4 and 40 and $S = 1.6$, which falls between the separation distances of the two present cases in the suppressed breakup region. At $T = 2.0$, the trailing droplet punctures the bag structure of the lead droplet and coalesces with its stamen. The ligament that stretches at the rear of the intact trailing droplet at $T^* = 2.4$ resembles the conventional stamen. In the subsequent period, apart from formation of small bags, the main body of the trailing droplet tends to disintegrate into large pieces.

Overall speaking, the influence of the lead droplet on the breakup behavior of the trailing droplet in the bag-and-stamen morphology is similar to that in the bag breakup morphology. The bag development of the trailing droplet is weakened, and more mass is preserved in the ring/stamen structure or in an intact body. Consequently, a larger portion of the trailing droplet is atomized into large fragments instead of fine mist.

C. Multibag breakup

1. Transition region: Dampened bag formation

For the multibag breakup, the transition region covers the current cases with separation distances from $S = 1.9$ to 6.2. The

breakup behavior of the tandem droplets is characterized in Fig. 13 with the case at $S = 6.2$ and $We = 68$. The deformation of the lead droplet starts with the typical flattening ($T = 1.0$), followed by a short period of bending of the thin peripheral sheet ($T = 1.45$). Then, consecutive formation and rupture of bags take place around the periphery, shedding small mist into the flow ($T = 1.85$). The remaining stamen-like structure at $T = 2.6$ further fragments through rupture of tiny bags and fracture of thin ligaments. The trailing droplet follows the breakup morphology of the lead droplet, but the formation and rupture of bags are noticeably dampened by the shielding effect. Compared to the bag-and-stamen breakup, the multibag mode leaves a thicker stamen-like structure and generates no toroidal ring.

2. Suppressed breakup region: Coalescence of the trailing droplet with the stamen-like structure of the lead droplet

When the separation distance drops to 1.2, the lead droplet still maintains main features of the multibag morphology, but the breakup of the trailing droplet is significantly altered as shown in Fig. 14. The strong shielding effect shapes the front of the trailing droplet into a sharp cone ($T = 0.4$). A liquid sheet is subsequently developed along the periphery ($T = 0.7$) and stretched in the streamwise direction ($T = 1.0$). The elongated trailing droplet collides with the flattened lead droplet at $T = 1.4$ and coalesces into the stamen-like structure that emerges at $T = 2.6$.

In the multibag morphology, the burst of bags of the lead droplet tends to eject fine fragments widely in the cross-stream direction. However, since the bag inflation of the trailing droplet is significantly dampened by the shielding effect as shown in Fig. 13,

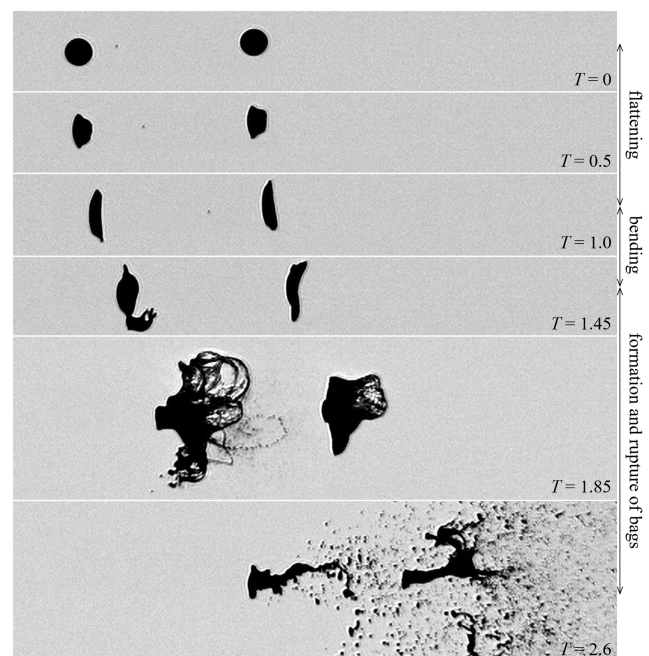


FIG. 13. Less intense formation of bags for the trailing droplet under the shielding effect of the lead droplet ($S = 6.2$, $We = 68$).

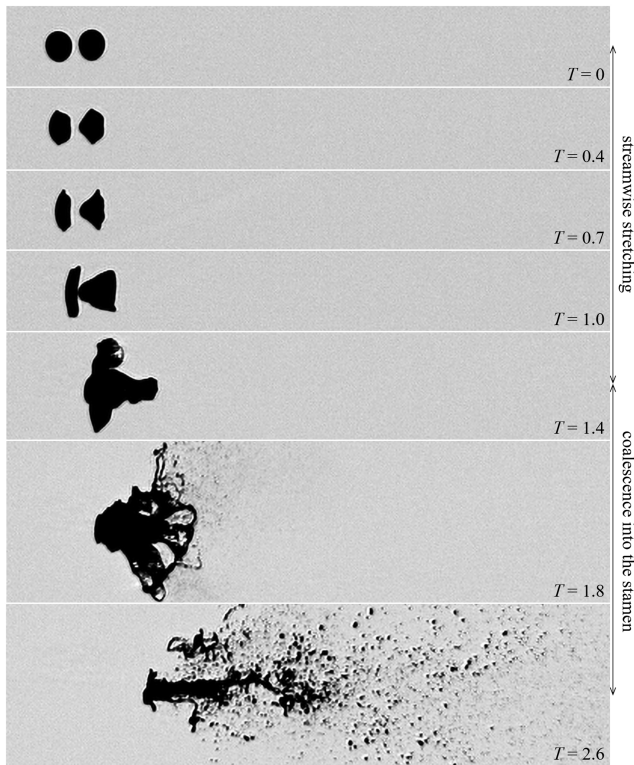


FIG. 14. Coalescence of the trailing droplet into the stamen-like structure of the lead droplet ($S = 1.2$, $We = 68$).

the resultant fragments gain less cross-stream momentum from the outward splash of the bag rupture, and thus, the spatial distribution is substantially confined. After the tandem droplets collide and merge, their fragments are blended together and dispersed in a conical pattern. Figure 15 compares the dispersion angle of the mixed fragments at $T = 3.0$ and shows that the dispersion angle is narrowed from 81° to 59° as the separation distance decreases from 3.8 to 1.2.

D. Shear stripping

1. Transition region: Narrower fragment dispersion for the trailing droplet

The last morphology covered in the current work is the shear stripping breakup, which is also conventionally understood as the

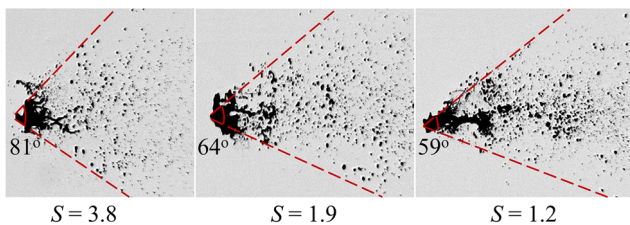


FIG. 15. Dispersion angle of the fragments detaching from the merged body of the tandem droplets in the multibag regime at $T = 3.0$ ($We = 68, 70,$ and 68 from left to right).

ultimate breakup regime.¹⁴ The transition region for this breakup morphology covers all present cases with $S \leq 4.5$, and no suppressed breakup region is identified in the current work. Figure 16 shows the exemplary case with $S = 3.8$ and $We = 179$. The lead and trailing droplets share the same breakup morphology, consisting of initial flattening ($T = 0.3$), bending of the peripheral sheet ($T = 0.6$), and stripping of fine mist along the sheet ($T = 1.2$). The breakup is characterized by the fragmentation of the peripheral sheet into thin ligaments and further into micro-droplets. Consecutive inflation and burst of tiny bags along the peripheral sheet is observed at the very beginning of the fragmentation ($T = 0.85$) but ceases in a short time. The main difference between the tandem droplets is that in the late stage the trailing droplet is less flattened and the resultant fragments are dispersed less widely in the cross-stream direction. Igra and Takayama²⁹ have reported similar observations for tandem water columns separated at $S = 5$ for a much higher Weber number of 6900.

It is worth mentioning that at the smallest separation distance $S = 1.3$ in the present study, the trailing droplet is shaped with a sharply tapered front similarly to that shown in Fig. 14 in the early stage but follows main stripping breakup features afterward. The corresponding image sequence is omitted for brevity.

Figure 17 compares the dispersion angle of fragments shed off the merged body of the tandem droplets at $T = 3.0$ for cases at $S = 3.8, 2.0,$ and 1.3 . The cross-stream span occupied by the fragments becomes consistently narrower as the separation distance decreases.

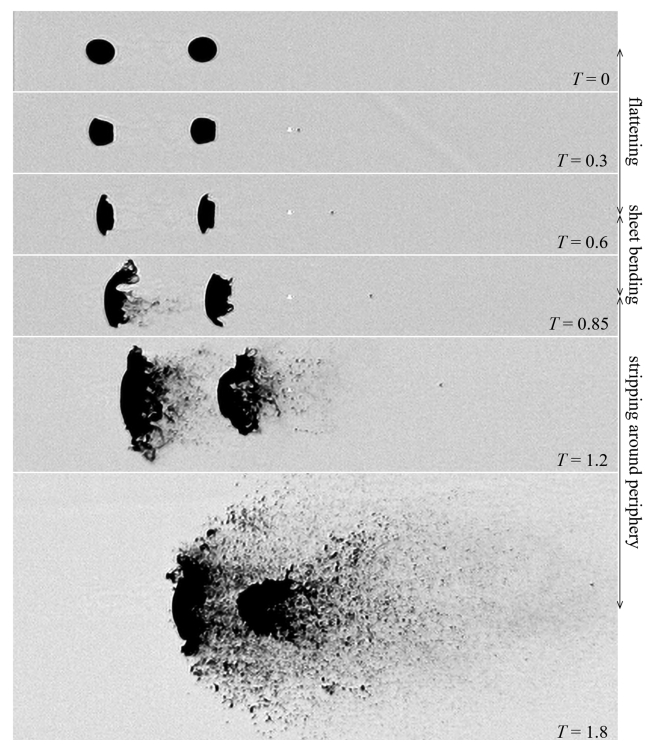


FIG. 16. Narrower cross-stream dispersion of the trailing droplet fragments under the shielding effect of the lead droplet ($S = 3.8$, $We = 179$).

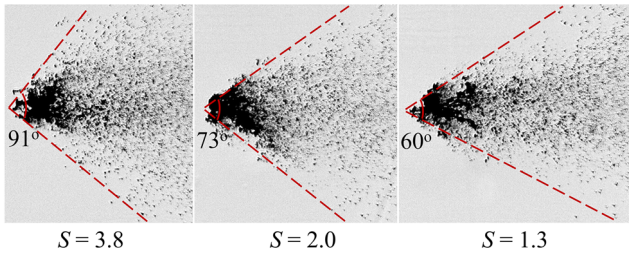


FIG. 17. Dispersion angle of the fragments detaching from the merged body of the tandem droplets in the shear stripping regime at $T = 3.0$ ($We = 179, 183,$ and 184 from left to right).

This trend is consistent with that observed in Fig. 15 for the multibag regime.

E. Quantitative analyses of the early-stage deformation of the tandem droplets

The early-stage deformation of droplets plays a crucial role in determining the subsequent breakup morphology, and the associated parameters are also of practical importance for numerical validations. This section quantifies the early-stage behavior of the tandem droplets and highlights the variation at different Weber numbers and separation distances. The quantified parameters in the current work are the time of initial deformation T_{ini} , the maximum cross-stream diameter D_{cmax} , and the mean drag coefficient C_{dmean} .

The initial deformation of droplets ends at the time instant of the minimum streamwise diameter. This time instant T_{ini} marks the start of the bag inflation for bag and bag-and-stamen morphologies and the bending of the peripheral sheet over the rear surface for multibag and shear stripping morphologies. The definition was proposed by Pilch and Erdman⁷ to indicate the breakup initiation and also adopted in other literature.^{6,17} The maximum cross-stream diameter D_{cmax} is the cross-stream diameter at T_{ini} normalized against the initial diameter. The mean drag coefficient C_{dmean} is calculated by fitting the streamwise displacement of the droplet mass center x_{mc} between $T = 0$ and T_{ini} into the relation

$$x_{mc}/d_0 = 3/8 \cdot C_{dmean} T^2 \quad (5)$$

derived by Ranger and Nicholls.¹² For all cases, T_{ini} lies within the steady-flow time window.

1. Influence of the tandem formation on the early-stage deformation of the lead droplet

Table II summarizes T_{ini} , D_{cmax} , and C_{dmean} of the lead droplet in different breakup morphologies. The values are averaged from experiments of which the breakup regime is the same but the separation distances are varied. The time of initial deformation $T_{ini,lead}$ decreases consistently from 1.19 at $We = 13$ to 0.71 at $We = 180$. This tendency is in agreement with the empirical correlation

$$T_{ini} = 1.9(We - 12)^{-0.25} (1 + 2.2Oh^{1.6}) \quad (6)$$

TABLE II. The time of initial deformation T_{ini} , the maximum cross-stream diameter D_{cmax} , and the mean drag coefficient C_{dmean} of the lead droplet, averaged from experiments in the same breakup morphology.

We	$T_{ini,lead}$	$D_{cmax,lead}$	$C_{dmean,lead}$
13 (± 1.3)	1.19 ($\pm 1.2\%$)	1.67 ($\pm 3.6\%$)	1.40 ($\pm 1.4\%$)
24 (± 2.2)	1.08 ($\pm 1.7\%$)	1.88 ($\pm 3.9\%$)	1.58 ($\pm 2.1\%$)
70 (± 3.0)	0.83 ($\pm 2.3\%$)	1.73 ($\pm 4.2\%$)	1.25 ($\pm 3.0\%$)
180 (± 10)	0.71 ($\pm 2.4\%$)	1.67 ($\pm 4.4\%$)	1.20 ($\pm 2.3\%$)

proposed by Pilch and Erdman,⁷ except that this correlation predicts a higher value of 1.9 at $We = 13$. Meanwhile, the maximum cross-stream diameter $D_{cmax,lead}$ peaks with the value of 1.88 for bag-and-stamen breakup and then declines as We keeps increasing. The data points reported by Zhao *et al.*³⁵ show the same trend but slightly different magnitudes. In terms of the mean drag coefficient $C_{dmean,lead}$, the effect of the droplet flattening is not excluded in the current calculation. Consequently, in addition to flow Reynolds numbers, $C_{dmean,lead}$ is also significantly influenced by the growth rate of the droplet cross-stream diameter. This explains the observation that $C_{dmean,lead}$ follows a similar trend to $D_{cmax,lead}$ and that the magnitudes exceed 1.2, which is the drag coefficient of a circular disk.³⁶ Overall speaking, the early-stage behavior of the lead droplet is barely influenced by the tandem formation, and the quantified parameters are consistent with those of isolated droplets.

Table II also provides the range of variation for T_{ini} , D_{cmax} , and C_{dmean} . All three parameters vary within the interval of $\pm 4.5\%$. The variation is mainly caused by the difference in the flow conditions (which is also implied by the variation of Weber numbers) and the irregularity of the initial droplet shapes. Compared to the overall variation, the measurement uncertainty is relatively low. With current framing rates and spatial resolutions of the recorded images, the uncertainty for temporal and spatial calculations is $\pm 1.3\%$ and $\pm 1.5\%$, respectively.

2. Influence of the tandem formation on the early-stage deformation of the trailing droplet

This section is focused on the influence of the tandem formation on the breakup behavior of the trailing droplet. The S - We maps of the time of initial deformation, the maximum cross-stream diameter, and the mean drag coefficient are presented sequentially. Considering that the lead and trailing droplets from one experiment experience identical flow conditions and tend to share similar initial shapes, the data points presented for the trailing droplet are normalized against values of the lead droplet, in order to minimize the uncertainties brought by flow variation and shape irregularity.

The time of initial deformation of the trailing droplet relative to the lead droplet $T_{ini,trail}/T_{ini,lead}$ is plotted in Fig. 18 over the S - We map. Isolines of 1.01, 1.03, 1.06, and 1.09 provided in the figure are calculated through interpolation of the discrete data points. Cases in the suppressed breakup region are labeled dark circles and excluded in the present calculation since the trailing droplet fails to initiate the breakup independently. Generally speaking, $T_{ini,trail}$ is postponed by the tandem formation, and the postponement is longer at smaller

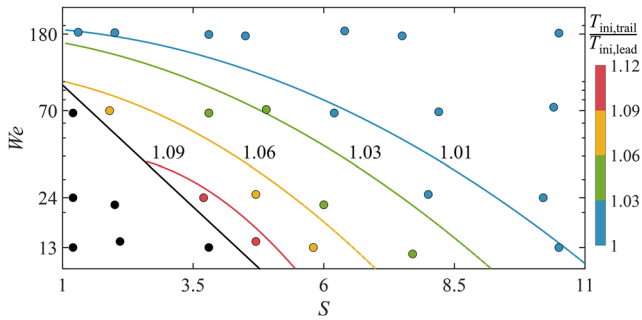


FIG. 18. Time of initial deformation of the trailing droplet at different separation distances and Weber numbers, normalized by values of the lead droplet.

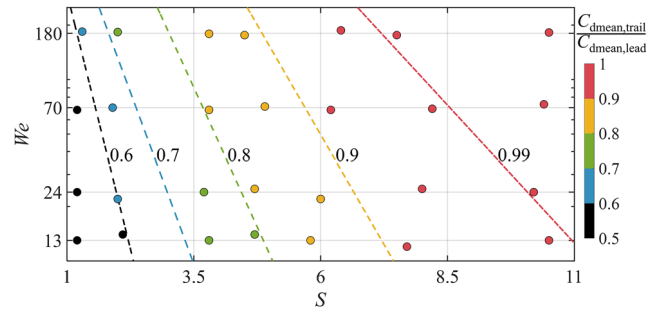


FIG. 20. Mean drag coefficient of the trailing droplet at different separation distances and Weber numbers, normalized by values of the lead droplet.

S and lower We . For low- We bag and bag-and-stamen morphologies, T_{ini} is marked by the end of droplet flattening. The flattening is caused by the pressure imbalance around the droplet and highly sensitive to the shielding effect, which significantly reduces the pressure imposed on the front of the trailing droplet as illustrated in Fig. 9. For high- We multibag and shear stripping morphologies, however, T_{ini} is indicated by the bending of the peripheral sheet over the droplet rear. As demonstrated by the experimental work of Theofanous *et al.*³⁷ and Wang *et al.*,³³ development of the peripheral sheet is dominated by the local shear flow around the equator, which is much less influenced by the shielding effect than the pressure imbalance around the droplet. Consequently, the postponement of $T_{ini, trail}$ is strongly reduced as the Weber number increases. Particularly, the influence is negligible in the shear stripping regime.

Figure 19 presents the maximum cross-stream diameter of the trailing droplet normalized against values of the lead droplet $D_{cmax, trail} / D_{cmax, lead}$. Interpolated isolines of 0.99, 0.97, 0.94, and 0.91 are also displayed. The general tendency is that $D_{cmax, trail}$ is reduced by the presence of the lead droplet, and the reduction is higher at closer S and lower We . For all breakup morphologies, the growth of the cross-stream diameter is dominated by the flattening of the main body. As discussed before, the shielding effect of the lead droplet reduces the pressure at the front of the trailing droplet and, thus,

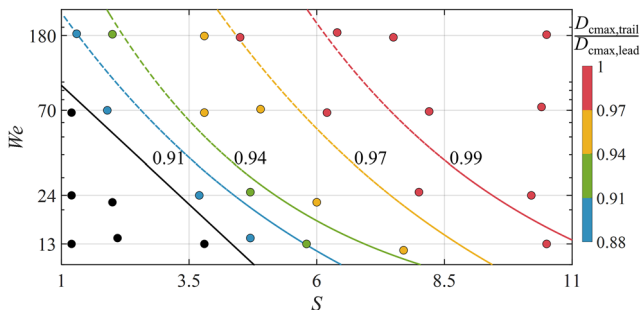


FIG. 19. Maximum cross-stream diameter of the trailing droplet at different separation distances and Weber numbers, normalized by values of the lead droplet.

results in lower $D_{cmax, trail}$. The strength of the shielding effect differs from case to case. The lead droplet deforms into a flat disk at low We ($T = 1.0$ in Fig. 5) and into an ellipsoid at high We ($T = 0.6$ in Fig. 16). Ellipsoidal shapes induce weaker flow separation in the wake than flat disks, and the corresponding shielding is less effective. In addition, the cross-stream diameter of the deformed lead droplet tends to be smaller at higher We , which further alleviates the shielding effect on the trailing droplet. Consequently, the reduction of $D_{cmax, trail}$ is lowered as the Weber number increases.

The variation of the mean drag coefficient of the trailing droplet over the S - We map is shown in Fig. 20. For cases where the trailing droplet fails to initiate the breakup independently, $C_{dmean, trail}$ is calculated by fitting into Eq. (5), the data prior to the collision with the lead droplet. The change of $C_{dmean, trail}$ with S and We follows similar patterns to $D_{cmax, trail}$. Again, the shielding effect is stronger at smaller S and lower We and accounts for the reduction of $C_{dmean, trail}$.

IV. SUMMARY AND CONCLUSION

The present work experimentally investigates the breakup of two identically sized droplets in tandem formation. The breakup is triggered by a planar shock wave and recorded by an ultra-high-speed camera integrated into a shadowgraph system. The experimental matrix consists of seven separation distances S ranging from 1.2 to 10.5 times of the droplet diameter and four Weber numbers We between 13 and 180 covering bag, bag-and-stamen, multi-bag, and shear stripping breakup morphologies. The influences of the tandem formation on the breakup behavior are summarized as follows:

- (a) The presence of the trailing droplet exerts marginal effects on the lead droplet. The lead droplet replicates the breakup morphology of isolated droplets in all cases, except for the bag breakup at $S = 1.2$ where the tandem droplets coalesce with no further bag formation.
- (b) When the separation distance falls below critical levels, the breakup intensity of the trailing droplet is consistently weakened although the conventional breakup morphology is preserved. In the early stage, the tandem formation postpones the time of initial deformation for the trailing droplet, lowers the maximum cross-stream diameter, and reduces the mean drag coefficient. These effects are stronger at lower

Weber numbers and are intensified as the separation distance decreases. In the late stage, the bag structure is inflated to a smaller size for bag and bag-and-stamen morphologies, and the fragments are less widely dispersed in the cross-stream direction for multibag and shear stripping morphologies. Notably, the critical separation distance is We -dependent and halved from $S = 10.8$ at $We = 13$ to $S = 5.4$ at $We = 180$.

- (c) For cases where the tandem droplets are in very close proximity, the trailing droplet exhibits streamwise stretching instead of flattening during the initial deformation and either punctures or coalesces with the lead droplet in the later period.

To the best of our knowledge, the current study is the first work that experimentally investigates tandem droplet breakup over a wide range of Weber numbers and separation distances. The present results can be particularly helpful for accurate modeling of fragment sizes and breakup timings in applications related with dense sprays.

ACKNOWLEDGMENTS

The authors acknowledge funding from the European Research Council (ERC) under the European Union's Horizon 2020 research and innovation program (Grant Agreement No. 667483).

DATA AVAILABILITY

The data that support the findings of this study are openly available in mediaTUM.

REFERENCES

- ¹R. D. Reitz and R. Diwakar, "Effect of drop breakup on fuel sprays," SAE Tech. Pap. Ser. 1 **95**(3), 218–227 (1986), available at <https://www.jstor.org/stable/44725372>.
- ²S. Lagutkin, L. Achelis, S. Sheikhaliev, V. Uhlenwinkel, and V. Srivastava, "Atomization process for metal powder," *Mater. Sci. Eng. A* **383**(1), 1–6 (2004).
- ³J. Mostaghimi, M. Pasandideh-Fard, and S. Chandra, "Dynamics of splat formation in plasma spray coating process," *Plasma Chem. Plasma Process.* **22**(1), 59–84 (2002).
- ⁴W. R. Lane, "Shatter of drops in streams of air," *Ind. Eng. Chem.* **43**(6), 1312–1317 (1951).
- ⁵J. O. Hinze, "Fundamentals of the hydrodynamic mechanism of splitting in dispersion processes," *AIChE J.* **1**(3), 289–295 (1955).
- ⁶D. R. Gueldenbecher, C. López-Rivera, and P. E. Sojka, "Secondary atomization," *Exp. Fluids* **46**(3), 371–402 (2009).
- ⁷M. Pilch and C. A. Erdman, "Use of breakup time data and velocity history data to predict the maximum size of stable fragments for acceleration-induced breakup of a liquid drop," *Int. J. Multiphase Flow* **13**(6), 741–757 (1987).
- ⁸G. M. Faeth, L.-P. Hsiang, and P.-K. Wu, "Structure and breakup properties of sprays," *Int. J. Multiphase Flow* **21**, 99–127 (1995).
- ⁹W.-H. Chou and G. M. Faeth, "Temporal properties of secondary drop breakup in the bag breakup regime," *Int. J. Multiphase Flow* **24**(6), 889–912 (1998).
- ¹⁰D. D. Joseph, J. Belanger, and G. S. Beavers, "Breakup of a liquid drop suddenly exposed to a high-speed airstream," *Int. J. Multiphase Flow* **25**, 1263–1303 (1999).
- ¹¹J. Han and G. Tryggvason, "Secondary breakup of axisymmetric liquid drops. I. Acceleration by a constant body force," *Phys. Fluids* **11**(12), 3650–3667 (1999).
- ¹²A. A. Ranger and J. A. Nicholls, "Aerodynamic shattering of liquid drops," *AIAA J.* **7**(2), 285–290 (1969).
- ¹³Z. Liu and R. D. Reitz, "An analysis of the distortion and breakup mechanisms of high speed liquid drops," *Int. J. Multiphase Flow* **23**(4), 631–650 (1997).
- ¹⁴T. G. Theofanous and G. J. Li, "On the physics of aerobreakup," *Phys. Fluids* **20**(5), 052103 (2008).
- ¹⁵Z. Dai and G. M. Faeth, "Temporal properties of secondary drop breakup in the multimode breakup regime," *Int. J. Multiphase Flow* **27**(2), 217–236 (2001).
- ¹⁶Y. Chen, E. P. DeMauro, J. L. Wagner, M. Arienti, D. R. Gueldenbecher, P. Farias, T. W. Grasser, P. Sanderson, S. Albert, A. Turpin, W. Sealy, and R. S. Ketchum, "Aerodynamic breakup and secondary drop formation for a liquid metal column in a shock-induced cross-flow," in *55th AIAA Aerospace Sciences Meeting* (AIAA, 2017), p. 1892.
- ¹⁷L.-P. Hsiang and G. M. Faeth, "Near-limit drop deformation and secondary breakup," *Int. J. Multiphase Flow* **18**(5), 635–652 (1992).
- ¹⁸T. G. Theofanous, G. J. Li, and T. N. Dinh, "Aerobreakup in rarefied supersonic gas flows," *J. Fluids Eng.* **126**(4), 516 (2004).
- ¹⁹M. Jain, R. S. Prakash, G. Tomar, and R. V. Ravikrishna, "Secondary breakup of a drop at moderate Weber numbers," *Proc. R. Soc. A* **471**(2177), 20140930 (2015).
- ²⁰N. Ashgriz, *Handbook of Atomization and Sprays: Theory and Applications* (Springer Science & Business Media, 2011).
- ²¹G. J. Dorr, A. J. Hewitt, S. W. Adkins, J. Hanan, H. Zhang, and B. Noller, "A comparison of initial spray characteristics produced by agricultural nozzles," *Crop Prot.* **53**, 109–117 (2013).
- ²²D. Y. Liu, K. Anders, and A. Frohn, "Drag coefficients of single droplets moving in an infinite droplet chain on the axis of a tube," *Int. J. Multiphase Flow* **14**(2), 217–232 (1988).
- ²³J. A. Mulholland, R. K. Srivastava, and J. O. L. Wendt, "Influence of droplet spacing on drag coefficient in nonevaporating, monodisperse streams," *AIAA J.* **26**(10), 1231–1237 (1988).
- ²⁴J. Y. Poo and N. Ashgriz, "Variation of drag coefficients in an interacting drop stream," *Exp. Fluids* **11**(1), 1–8 (1991).
- ²⁵S. Temkin and G. Z. Ecker, "Droplet pair interactions in a shock-wave flow field," *J. Fluid Mech.* **202**, 467–497 (1989).
- ²⁶Q. V. Nguyen and D. Dunn-Rankin, "Experiments examining drag in linear droplet packets," *Exp. Fluids* **12**, 157–165 (1992).
- ²⁷C. H. Chiang and W. A. Sirignano, "Axisymmetric calculations of three-droplet interactions," *Atomization Sprays* **3**(1), 91–107 (1993).
- ²⁸H. Zhao, Z. Wu, W. Li, J. Xu, and H. Liu, "Interaction of two drops in the bag breakup regime by a continuous air jet," *Fuel* **236**, 843–850 (2019).
- ²⁹D. Igra and K. Takayama, "Experimental investigation of two cylindrical water columns subjected to planar shock wave loading," *J. Fluids Eng.* **125**(2), 325 (2003).
- ³⁰S. Quan, J. Lou, and H. A. Stone, "Interactions between two deformable droplets in tandem subjected to impulsive acceleration by surrounding flows," *J. Fluid Mech.* **684**, 384–406 (2011).
- ³¹T. Kékési, M. Altimira, G. Amberg, and L. Prah Wittberg, "Interaction between two deforming liquid drops in tandem and various off-axis arrangements subject to uniform flow," *Int. J. Multiphase Flow* **112**, 193–218 (2019).
- ³²D. Stefanitsis, I. Malgarinos, G. Strotos, N. Nikolopoulos, E. Kakaras, and M. Gavaies, "Numerical investigation of the aerodynamic breakup of droplets in tandem," *Int. J. Multiphase Flow* **113**, 289–303 (2019).
- ³³Z. Wang, T. Hopfes, M. Giglmaier, and N. A. Adams, "Effect of Mach number on droplet aerobreakup in shear stripping regime," *Exp. Fluids* **61**(9), 1–17 (2020).
- ³⁴J. Kim, J. K. Lee, and K. M. Lee, "Accurate image super-resolution using very deep convolutional networks," in *2016 IEEE Conference on Computer Vision and Pattern Recognition (CVPR)* (IEEE, 2016), pp. 1646–1654.
- ³⁵H. Zhao, H.-F. Liu, W.-F. Li, and J.-L. Xu, "Morphological classification of low viscosity drop bag breakup in a continuous air jet stream," *Phys. Fluids* **22**(11), 114103 (2010).
- ³⁶F. W. Roos and W. W. Willmarth, "Some experimental results on sphere and disk drag," *AIAA J.* **9**(2), 285–291 (1971).
- ³⁷T. G. Theofanous, V. V. Mitkin, C. L. Ng, C.-H. Chang, X. Deng, and S. Sushchikh, "The physics of aerobreakup. II. Viscous liquids," *Phys. Fluids* **24**(2), 022104 (2012).

B Copyright Permissions for Reproduced Material

The copyright permissions for reproduced material in this thesis are attached here.

ELSEVIER LICENSE TERMS AND CONDITIONS

Jan 26, 2021

This Agreement between Mr. Zhaoguang Wang ("You") and Elsevier ("Elsevier") consists of your license details and the terms and conditions provided by Elsevier and Copyright Clearance Center.

License Number	4996361196364
License date	Jan 26, 2021
Licensed Content Publisher	Elsevier
Licensed Content Publication	International Journal of Multiphase Flow
Licensed Content Title	Drop deformation and breakup due to shock wave and steady disturbances
Licensed Content Author	L.-P. Hsiang,G.M. Faeth
Licensed Content Date	Aug 1, 1995
Licensed Content Volume	21
Licensed Content Issue	4
Licensed Content Pages	16
Start Page	545
End Page	560
Type of Use	reuse in a thesis/dissertation
Portion	figures/tables/illustrations
Number of figures/tables/illustrations	1
Format	both print and electronic
Are you the author of this Elsevier article?	No
Will you be translating?	No
Title	Experimental Investigation of Shock-Induced Droplet Breakup
Institution name	Technical University of Munich
Expected presentation date	Jun 2021
Portions	Fig. 3
Requestor Location	Mr. Zhaoguang Wang Hauptstr. 22 Eching, 85386 Germany Attn: Zhaoguang Wang
Publisher Tax ID	GB 494 6272 12
Total	0.00 USD
Terms and Conditions	

INTRODUCTION

1. The publisher for this copyrighted material is Elsevier. By clicking "accept" in connection with completing this licensing transaction, you agree that the following terms and conditions apply to this transaction (along with the Billing and Payment terms and conditions established by Copyright Clearance Center, Inc. ("CCC"), at the time that you opened your Rightslink account and that are available at any time at <http://myaccount.copyright.com>).

GENERAL TERMS

- Elsevier hereby grants you permission to reproduce the aforementioned material subject to the terms and conditions indicated.
- Acknowledgement: If any part of the material to be used (for example, figures) has appeared in our publication with credit or acknowledgement to another source, permission must also be sought from that source. If such permission is not obtained then that material may not be included in your publication/copies. Suitable acknowledgement to the source must be made, either as a footnote or in a reference list at the end of your publication, as follows:
"Reprinted from Publication title, Vol /edition number, Author(s), Title of article / title of chapter, Pages No., Copyright (Year), with permission from Elsevier [OR APPLICABLE SOCIETY COPYRIGHT OWNER]." Also Lancet special credit - "Reprinted from The Lancet, Vol. number, Author(s), Title of article, Pages No., Copyright (Year), with permission from Elsevier."
- Reproduction of this material is confined to the purpose and/or media for which permission is hereby given.
- Altering/Modifying Material: Not Permitted. However figures and illustrations may be altered/adapted minimally to serve your work. Any other abbreviations, additions, deletions and/or any other alterations shall be made only with prior written authorization of Elsevier Ltd. (Please contact Elsevier's permissions helpdesk [here](#)). No modifications can be made to any Lancet figures/tables and they must be reproduced in full.
- If the permission fee for the requested use of our material is waived in this instance, please be advised that your future requests for Elsevier materials may attract a fee.

7. **Reservation of Rights:** Publisher reserves all rights not specifically granted in the combination of (i) the license details provided by you and accepted in the course of this licensing transaction, (ii) these terms and conditions and (iii) CCC's Billing and Payment terms and conditions.
8. **License Contingent Upon Payment:** While you may exercise the rights licensed immediately upon issuance of the license at the end of the licensing process for the transaction, provided that you have disclosed complete and accurate details of your proposed use, no license is finally effective unless and until full payment is received from you (either by publisher or by CCC) as provided in CCC's Billing and Payment terms and conditions. If full payment is not received on a timely basis, then any license preliminarily granted shall be deemed automatically revoked and shall be void as if never granted. Further, in the event that you breach any of these terms and conditions or any of CCC's Billing and Payment terms and conditions, the license is automatically revoked and shall be void as if never granted. Use of materials as described in a revoked license, as well as any use of the materials beyond the scope of an unrevoked license, may constitute copyright infringement and publisher reserves the right to take any and all action to protect its copyright in the materials.
9. **Warranties:** Publisher makes no representations or warranties with respect to the licensed material.
10. **Indemnity:** You hereby indemnify and agree to hold harmless publisher and CCC, and their respective officers, directors, employees and agents, from and against any and all claims arising out of your use of the licensed material other than as specifically authorized pursuant to this license.
11. **No Transfer of License:** This license is personal to you and may not be sublicensed, assigned, or transferred by you to any other person without publisher's written permission.
12. **No Amendment Except in Writing:** This license may not be amended except in a writing signed by both parties (or, in the case of publisher, by CCC on publisher's behalf).
13. **Objection to Contrary Terms:** Publisher hereby objects to any terms contained in any purchase order, acknowledgment, check endorsement or other writing prepared by you, which terms are inconsistent with these terms and conditions or CCC's Billing and Payment terms and conditions. These terms and conditions, together with CCC's Billing and Payment terms and conditions (which are incorporated herein), comprise the entire agreement between you and publisher (and CCC) concerning this licensing transaction. In the event of any conflict between your obligations established by these terms and conditions and those established by CCC's Billing and Payment terms and conditions, these terms and conditions shall control.
14. **Revocation:** Elsevier or Copyright Clearance Center may deny the permissions described in this License at their sole discretion, for any reason or no reason, with a full refund payable to you. Notice of such denial will be made using the contact information provided by you. Failure to receive such notice will not alter or invalidate the denial. In no event will Elsevier or Copyright Clearance Center be responsible or liable for any costs, expenses or damage incurred by you as a result of a denial of your permission request, other than a refund of the amount(s) paid by you to Elsevier and/or Copyright Clearance Center for denied permissions.

LIMITED LICENSE

The following terms and conditions apply only to specific license types:

15. **Translation:** This permission is granted for non-exclusive world **English** rights only unless your license was granted for translation rights. If you licensed translation rights you may only translate this content into the languages you requested. A professional translator must perform all translations and reproduce the content word for word preserving the integrity of the article.
16. **Posting licensed content on any Website:** The following terms and conditions apply as follows: Licensing material from an Elsevier journal: All content posted to the web site must maintain the copyright information line on the bottom of each image; A hyper-text must be included to the Homepage of the journal from which you are licensing at <http://www.sciencedirect.com/science/journal/xxxxx> or the Elsevier homepage for books at <http://www.elsevier.com>; Central Storage: This license does not include permission for a scanned version of the material to be stored in a central repository such as that provided by Heron/XanEdu. Licensing material from an Elsevier book: A hyper-text link must be included to the Elsevier homepage at <http://www.elsevier.com>. All content posted to the web site must maintain the copyright information line on the bottom of each image.

Posting licensed content on Electronic reserve: In addition to the above the following clauses are applicable: The web site must be password-protected and made available only to bona fide students registered on a relevant course. This permission is granted for 1 year only. You may obtain a new license for future website posting.

17. **For journal authors:** the following clauses are applicable in addition to the above:

Preprints:

A preprint is an author's own write-up of research results and analysis, it has not been peer-reviewed, nor has it had any other value added to it by a publisher (such as formatting, copyright, technical enhancement etc.).

Authors can share their preprints anywhere at any time. Preprints should not be added to or enhanced in any way in order to appear more like, or to substitute for, the final versions of articles however authors can update their preprints on arXiv or RePEc with their Accepted Author Manuscript (see below).

If accepted for publication, we encourage authors to link from the preprint to their formal publication via its DOI. Millions of researchers have access to the formal publications on ScienceDirect, and so links will help users to find, access, cite and use the best available version. Please note that Cell Press, The Lancet and some society-owned have different preprint policies. Information on these policies is available on the journal homepage.

Accepted Author Manuscripts: An accepted author manuscript is the manuscript of an article that has been accepted for publication and which typically includes author-incorporated changes suggested during submission, peer review and editor-author communications.

Authors can share their accepted author manuscript:

- immediately
 - via their non-commercial person homepage or blog
 - by updating a preprint in arXiv or RePEc with the accepted manuscript
 - via their research institute or institutional repository for internal institutional uses or as part of an invitation-only research collaboration work-group
 - directly by providing copies to their students or to research collaborators for their personal use
 - for private scholarly sharing as part of an invitation-only work group on commercial sites with which Elsevier has an agreement
- After the embargo period
 - via non-commercial hosting platforms such as their institutional repository
 - via commercial sites with which Elsevier has an agreement

In all cases accepted manuscripts should:

- link to the formal publication via its DOI
- bear a CC-BY-NC-ND license - this is easy to do
- if aggregated with other manuscripts, for example in a repository or other site, be shared in alignment with our hosting policy not be added to or enhanced in any way to appear more like, or to substitute for, the published journal article.

Published journal article (JPA): A published journal article (PJA) is the definitive final record of published research that appears or will appear in the journal and embodies all value-adding publishing activities including peer review co-ordination, copy-editing, formatting, (if relevant) pagination and online enrichment.

Policies for sharing publishing journal articles differ for subscription and gold open access articles:

Subscription Articles: If you are an author, please share a link to your article rather than the full-text. Millions of researchers have access to the formal publications on ScienceDirect, and so links will help your users to find, access, cite, and use the best available version.

Theses and dissertations which contain embedded PJAs as part of the formal submission can be posted publicly by the awarding institution with DOI links back to the formal publications on ScienceDirect.

If you are affiliated with a library that subscribes to ScienceDirect you have additional private sharing rights for others' research accessed under that agreement. This includes use for classroom teaching and internal training at the institution (including use in course packs and courseware programs), and inclusion of the article for grant funding purposes.

Gold Open Access Articles: May be shared according to the author-selected end-user license and should contain a [CrossMark logo](#), the end user license, and a DOI link to the formal publication on ScienceDirect.

Please refer to Elsevier's [posting policy](#) for further information.

18. **For book authors** the following clauses are applicable in addition to the above: Authors are permitted to place a brief summary of their work online only. You are not allowed to download and post the published electronic version of your chapter, nor may you scan the printed edition to create an electronic version. **Posting to a repository:** Authors are permitted to post a summary of their chapter only in their institution's repository.

19. **Thesis/Dissertation:** If your license is for use in a thesis/dissertation your thesis may be submitted to your institution in either print or electronic form. Should your thesis be published commercially, please reapply for permission. These requirements include permission for the Library and Archives of Canada to supply single copies, on demand, of the complete thesis and include permission for Proquest/UMI to supply single copies, on demand, of the complete thesis. Should your thesis be published commercially, please reapply for permission. Theses and dissertations which contain embedded PJAs as part of the formal submission can be posted publicly by the awarding institution with DOI links back to the formal publications on ScienceDirect.

Elsevier Open Access Terms and Conditions

You can publish open access with Elsevier in hundreds of open access journals or in nearly 2000 established subscription journals that support open access publishing. Permitted third party re-use of these open access articles is defined by the author's choice of Creative Commons user license. See our [open access license policy](#) for more information.

Terms & Conditions applicable to all Open Access articles published with Elsevier:

Any reuse of the article must not represent the author as endorsing the adaptation of the article nor should the article be modified in such a way as to damage the author's honour or reputation. If any changes have been made, such changes must be clearly indicated.

The author(s) must be appropriately credited and we ask that you include the end user license and a DOI link to the formal publication on ScienceDirect.

If any part of the material to be used (for example, figures) has appeared in our publication with credit or acknowledgement to another source it is the responsibility of the user to ensure their reuse complies with the terms and conditions determined by the rights holder.

Additional Terms & Conditions applicable to each Creative Commons user license:

CC BY: The CC-BY license allows users to copy, to create extracts, abstracts and new works from the Article, to alter and revise the Article and to make commercial use of the Article (including reuse and/or resale of the Article by commercial entities), provided the user gives appropriate credit (with a link to the formal publication through the relevant DOI), provides a link to the license, indicates if changes were made and the licensor is not represented as endorsing the use made of the work. The full details of the license are available at <http://creativecommons.org/licenses/by/4.0>.

CC BY NC SA: The CC BY-NC-SA license allows users to copy, to create extracts, abstracts and new works from the Article, to alter and revise the Article, provided this is not done for commercial purposes, and that the user gives appropriate credit (with a link to the formal publication through the relevant DOI), provides a link to the license, indicates if changes were made and the licensor is not represented as endorsing the use made of the work. Further, any new works must be made available on the same conditions. The full details of the license are available at <http://creativecommons.org/licenses/by-nc-sa/4.0>.

CC BY NC ND: The CC BY-NC-ND license allows users to copy and distribute the Article, provided this is not done for commercial purposes and further does not permit distribution of the Article if it is changed or edited in any way, and provided the user gives appropriate credit (with a link to the formal publication through the relevant DOI), provides a link to the license, and that the licensor is not represented as endorsing the use made of the work. The full details of the license are available at <http://creativecommons.org/licenses/by-nc-nd/4.0>. Any commercial reuse of Open Access articles published with a CC BY NC SA or CC BY NC ND license requires permission from Elsevier and will be subject to a fee. Commercial reuse includes:

- Associating advertising with the full text of the Article
- Charging fees for document delivery or access
- Article aggregation
- Systematic distribution via e-mail lists or share buttons

Posting or linking by commercial companies for use by customers of those companies.

20. **Other Conditions:**

v1.10

Questions? customercare@copyright.com or +1-855-239-3415 (toll free in the US) or +1-978-646-2777.

SPRINGER NATURE LICENSE TERMS AND CONDITIONS

Jan 26, 2021

This Agreement between Mr. Zhaoguang Wang ("You") and Springer Nature ("Springer Nature") consists of your license details and the terms and conditions provided by Springer Nature and Copyright Clearance Center.

License Number	4996370069416
License date	Jan 26, 2021
Licensed Content Publisher	Springer Nature
Licensed Content Publication	Experiments in Fluids
Licensed Content Title	Secondary atomization
Licensed Content Author	D. R. Guildenbecher et al
Licensed Content Date	Jan 22, 2009
Type of Use	Thesis/Dissertation
Requestor type	academic/university or research institute
Format	print and electronic
Portion	figures/tables/illustrations
Number of figures/tables/illustrations	1
Will you be translating?	no
Circulation/distribution	1 - 29
Author of this Springer Nature content	no
Title	Experimental Investigation of Shock-Induced Droplet Breakup
Institution name	Technical University of Munich
Expected presentation date	Jun 2021
Portions	Fig. 3
Requestor Location	Mr. Zhaoguang Wang Hauptstr. 22 Eching, 85386 Germany Attn: Zhaoguang Wang
Total	0.00 USD

[Terms and Conditions](#)

Springer Nature Customer Service Centre GmbH Terms and Conditions

This agreement sets out the terms and conditions of the licence (the **Licence**) between you and **Springer Nature Customer Service Centre GmbH** (the **Licensor**). By clicking 'accept' and completing the transaction for the material (**Licensed Material**), you also confirm your acceptance of these terms and conditions.

1. Grant of License

- 1.1.** The Licensor grants you a personal, non-exclusive, non-transferable, world-wide licence to reproduce the Licensed Material for the purpose specified in your order only. Licences are granted for the specific use requested in the order and for no other use, subject to the conditions below.
- 1.2.** The Licensor warrants that it has, to the best of its knowledge, the rights to license reuse of the Licensed Material. However, you should ensure that the material you are requesting is original to the Licensor and does not carry the copyright of another entity (as credited in the published version).
- 1.3.** If the credit line on any part of the material you have requested indicates that it was reprinted or adapted with permission from another source, then you should also seek permission from that source to reuse the material.

2. Scope of Licence

- 2.1.** You may only use the Licensed Content in the manner and to the extent permitted by these Ts&Cs and any applicable laws.
- 2.2.** A separate licence may be required for any additional use of the Licensed Material, e.g. where a licence has been purchased for print only use, separate permission must be obtained for electronic re-use. Similarly, a licence is only valid in the language selected and

does not apply for editions in other languages unless additional translation rights have been granted separately in the licence. Any content owned by third parties are expressly excluded from the licence.

2. 3. Similarly, rights for additional components such as custom editions and derivatives require additional permission and may be subject to an additional fee. Please apply to Journalpermissions@springernature.com/bookpermissions@springernature.com for these rights.

2. 4. Where permission has been granted **free of charge** for material in print, permission may also be granted for any electronic version of that work, provided that the material is incidental to your work as a whole and that the electronic version is essentially equivalent to, or substitutes for, the print version.

2. 5. An alternative scope of licence may apply to signatories of the [STM Permissions Guidelines](#), as amended from time to time.

3. Duration of Licence

3. 1. A licence for is valid from the date of purchase ('Licence Date') at the end of the relevant period in the below table:

Scope of Licence	Duration of Licence
Post on a website	12 months
Presentations	12 months
Books and journals	Lifetime of the edition in the language purchased

4. Acknowledgement

4. 1. The Licensor's permission must be acknowledged next to the Licenced Material in print. In electronic form, this acknowledgement must be visible at the same time as the figures/tables/illustrations or abstract, and must be hyperlinked to the journal/book's homepage. Our required acknowledgement format is in the Appendix below.

5. Restrictions on use

5. 1. Use of the Licensed Material may be permitted for incidental promotional use and minor editing privileges e.g. minor adaptations of single figures, changes of format, colour and/or style where the adaptation is credited as set out in Appendix 1 below. Any other changes including but not limited to, cropping, adapting, omitting material that affect the meaning, intention or moral rights of the author are strictly prohibited.

5. 2. You must not use any Licensed Material as part of any design or trademark.

5. 3. Licensed Material may be used in Open Access Publications (OAP) before publication by Springer Nature, but any Licensed Material must be removed from OAP sites prior to final publication.

6. Ownership of Rights

6. 1. Licensed Material remains the property of either Licensor or the relevant third party and any rights not explicitly granted herein are expressly reserved.

7. Warranty

IN NO EVENT SHALL LICENSOR BE LIABLE TO YOU OR ANY OTHER PARTY OR ANY OTHER PERSON OR FOR ANY SPECIAL, CONSEQUENTIAL, INCIDENTAL OR INDIRECT DAMAGES, HOWEVER CAUSED, ARISING OUT OF OR IN CONNECTION WITH THE DOWNLOADING, VIEWING OR USE OF THE MATERIALS REGARDLESS OF THE FORM OF ACTION, WHETHER FOR BREACH OF CONTRACT, BREACH OF WARRANTY, TORT, NEGLIGENCE, INFRINGEMENT OR OTHERWISE (INCLUDING, WITHOUT LIMITATION, DAMAGES BASED ON LOSS OF PROFITS, DATA, FILES, USE, BUSINESS OPPORTUNITY OR CLAIMS OF THIRD PARTIES), AND WHETHER OR NOT THE PARTY HAS BEEN ADVISED OF THE POSSIBILITY OF SUCH DAMAGES. THIS LIMITATION SHALL APPLY NOTWITHSTANDING ANY FAILURE OF ESSENTIAL PURPOSE OF ANY LIMITED REMEDY PROVIDED HEREIN.

8. Limitations

8. 1. **BOOKS ONLY:**Where 'reuse in a dissertation/thesis' has been selected the following terms apply: Print rights of the final author's accepted manuscript (for clarity, NOT the published version) for up to 100 copies, electronic rights for use only on a personal website or institutional repository as defined by the Sherpa guideline (www.sherpa.ac.uk/romeo/).

8. 2. For content reuse requests that qualify for permission under the [STM Permissions Guidelines](#), which may be updated from time to time, the STM Permissions Guidelines supersede the terms and conditions contained in this licence.

9. Termination and Cancellation

9. 1. Licences will expire after the period shown in Clause 3 (above).

9. 2. Licensee reserves the right to terminate the Licence in the event that payment is not received in full or if there has been a breach of this agreement by you.

Appendix 1 — Acknowledgements:

For Journal Content:

Reprinted by permission from [the Licensor]: [Journal Publisher (e.g. Nature/Springer/Palgrave)] [JOURNAL NAME] [REFERENCE CITATION (Article name, Author(s) Name), [COPYRIGHT] (year of publication)

For Advance Online Publication papers:

Reprinted by permission from [the Licensor]: [Journal Publisher (e.g. Nature/Springer/Palgrave)] [JOURNAL NAME] [REFERENCE CITATION (Article name, Author(s) Name), [COPYRIGHT] (year of publication), advance online publication, day month year (doi: 10.1038/sj.[JOURNAL ACRONYM].)

For Adaptations/Translations:

Adapted/Translated by permission from [the Licensor]: [Journal Publisher (e.g. Nature/Springer/Palgrave)] [JOURNAL NAME] [REFERENCE CITATION (Article name, Author(s) Name), [COPYRIGHT] (year of publication)

Note: For any republication from the British Journal of Cancer, the following credit line style applies:

Reprinted/adapted/translated by permission from [the Licensor]: on behalf of Cancer Research UK: : [Journal Publisher (e.g. Nature/Springer/Palgrave)] [JOURNAL NAME] [REFERENCE CITATION (Article name, Author(s) Name), [COPYRIGHT] (year of publication)

For Advance Online Publication papers:

Reprinted by permission from The [the Licensor]: on behalf of Cancer Research UK: [Journal Publisher (e.g. Nature/Springer/Palgrave)] [JOURNAL NAME] [REFERENCE CITATION (Article name, Author(s) Name), [COPYRIGHT] (year of publication), advance online publication, day month year (doi: 10.1038/sj.[JOURNAL ACRONYM])

For Book content:

Reprinted/adapted by permission from [the Licensor]: [Book Publisher (e.g. Palgrave Macmillan, Springer etc)] [Book Title] by [Book author(s)] [COPYRIGHT] (year of publication)

Other Conditions:

Version 1.3

Questions? customercare@copyright.com or +1-855-239-3415 (toll free in the US) or +1-978-646-2777.

AIP PUBLISHING LICENSE TERMS AND CONDITIONS

Feb 04, 2021

This Agreement between Mr. Zhaoguang Wang ("You") and AIP Publishing ("AIP Publishing") consists of your license details and the terms and conditions provided by AIP Publishing and Copyright Clearance Center.

License Number	5001840271125
License date	Feb 04, 2021
Licensed Content Publisher	AIP Publishing
Licensed Content Publication	Physics of Fluids
Licensed Content Title	Investigation on subsonic to supersonic flow around a sphere at low Reynolds number of between 50 and 300 by direct numerical simulation
Licensed Content Author	T. Nagata, T. Nonomura, S. Takahashi, et al
Licensed Content Date	May 1, 2016
Licensed Content Volume	28
Licensed Content Issue	5
Type of Use	Thesis/Dissertation
Requestor type	Student
Format	Print and electronic
Portion	Figure/Table
Number of figures/tables	1
Title	Experimental Investigation of Shock-Induced Droplet Breakup
Institution name	Technical University of Munich
Expected presentation date	Jun 2021
Portions	Fig. 3
Requestor Location	Mr. Zhaoguang Wang Hauptstr. 22 Eching, 85386 Germany Attn: Zhaoguang Wang
Total	0.00 EUR

Terms and Conditions

AIP Publishing -- Terms and Conditions: Permissions Uses

AIP Publishing hereby grants to you the non-exclusive right and license to use and/or distribute the Material according to the use specified in your order, on a one-time basis, for the specified term, with a maximum distribution equal to the number that you have ordered. Any links or other content accompanying the Material are not the subject of this license.

1. You agree to include the following copyright and permission notice with the reproduction of the Material: "Reprinted from [FULL CITATION], with the permission of AIP Publishing." For an article, the credit line and permission notice must be printed on the first page of the article or book chapter. For photographs, covers, or tables, the notice may appear with the Material, in a footnote, or in the reference list.
2. If you have licensed reuse of a figure, photograph, cover, or table, it is your responsibility to ensure that the material is original to AIP Publishing and does not contain the copyright of another entity, and that the copyright notice of the figure, photograph, cover, or table does not indicate that it was reprinted by AIP Publishing, with permission, from another source. Under no circumstances does AIP Publishing purport or intend to grant permission to reuse material to which it does not hold appropriate rights. You may not alter or modify the Material in any manner. You may translate the Material into another language only if you have licensed translation rights. You may not use the Material for promotional purposes.
3. The foregoing license shall not take effect unless and until AIP Publishing or its agent, Copyright Clearance Center, receives the Payment in accordance with Copyright Clearance Center Billing and Payment Terms and Conditions, which are incorporated herein by reference.
4. AIP Publishing or Copyright Clearance Center may, within two business days of granting this license, revoke the license for any reason whatsoever, with a full refund payable to you. Should you violate the terms of this license at any time, AIP Publishing, or Copyright Clearance Center may revoke the license with no refund to you. Notice of such revocation will be made using the contact information provided by you. Failure to receive such notice will not nullify the revocation.
5. AIP Publishing makes no representations or warranties with respect to the Material. You agree to indemnify and hold harmless AIP Publishing, and their officers, directors, employees or agents from and against any and all claims arising out of your use of the Material other than as specifically authorized herein.
6. The permission granted herein is personal to you and is not transferable or assignable without the prior written permission of AIP Publishing. This license may not be amended except in a writing signed by the party to be charged.
7. If purchase orders, acknowledgments or check endorsements are issued on any forms containing terms and conditions which are inconsistent with these provisions, such inconsistent terms and conditions shall be of no force and effect. This document, including the CCC Billing and Payment Terms and Conditions, shall be the entire agreement between the parties relating to the subject matter hereof.

This Agreement shall be governed by and construed in accordance with the laws of the State of New York. Both parties hereby submit to the jurisdiction of the courts of New York County for purposes of resolving any disputes that may arise hereunder.

V1.2

Questions? customercare@copyright.com or +1-855-239-3415 (toll free in the US) or +1-978-646-2777.